Author:
Biele, Jake

Title:
Resources for Integrated Quantum Sensing in the Mid-infrared

Resources for Integrated Quantum Sensing in the Mid-infrared

By

Jake Biele

Department of Physics
University of Bristol

A dissertation submitted to the University of Bristol in accordance with the requirements of the degree of Doctor of Philosophy in the Faculty of Science.

March 2022

Word count: 31,900

Abstract

Quantum states of light, with sub-classical noise statistics, are heralded as a potential route towards enhanced absorption spectroscopy. In this thesis we develop key infrastructure in the pursuit of quantum-enhanced absorption spectroscopy in the 2 µm-band via the adoption of integrated silicon photonics as a deployable and scalable solution.

Characterising quantum states of light in the 2 µm-band requires shot-noise limited homodyne detectors and so we start by presenting the design and characterisation of a homodyne detector that we use to make the first observation of megahertz speed vacuum shot-noise in this band. The device, designed primarily for pulsed illumination, has a 3-dB bandwidth of 13.2 MHz, total conversion efficiency of 57% at 2.07 µm, and a common-mode rejection ratio of 48 dB at 39.5 MHz.

We then utilise a silicon chip to implement an all-optical noise suppression scheme aimed at reducing the intensity noise of state-of-the-art pulsed lasers in this band via nonlinear interferometry. We find initial designs capable of noise suppression but with the addition of unwanted noise amplification from modulation instability.

In the final results chapter we look to expand the applicability of quantum states in absorption spectroscopy by analysing the effect of sample saturation on estimate precision in absorption measurements. We compare both classical and quantum probes. A limit is derived on the maximum precision gained from using a nonclassical probe and a measurement strategy for saturating this bound is presented. Finally, we evaluate amplitude-squeezed light as a viable route to gaining a quantum advantage under saturation.

This thesis is dedicated to Robin Austin whose inspirational teachings led me to maths & physics.

Acknowledgements

"If I have seen further, it is by standing on the shoulders of giants."

Sir Isaac Newton

The work presented in this thesis would not have been possible if it were not for the support and teachings of my supervisors, colleagues, and family & friends.

Specifically, I would like to thank my supervisors, **Dr. Jonathan Matthews** and **Dr. Joshua Silverstone**, for believing in me, for giving me the opportunity to undertake the challenge that is a PhD, and for inspiring me to work in such an exciting field. Beyond the direct support provided by Jonathan & Josh, I have also been lucky enough to benefit from the near-unlimited kindness of the many individuals that make up the groups they both lead.

In the quantum metrology group, I would like to thank **Euan Allen**, **Sabine Wollmann** & **Joel Tasker** for their wisdom and mentoring across all things, both scientific and personal. Without you, I am not sure I would have made it through the toughest stages of this journey. In the SWIR group, I would like to thank **Lawrence Rosenfeld** for easing my transition from the comfort of theoretical physics into the bewilderment of a quantum optics lab. The four of you are the pillars on which this thesis has been built.

A special thanks go to **David Payne**, **Dominic Sulway**, **Jonathan Frazer** and **Ben Sayers**. Though no two PhDs are the same, we embarked on this journey together and our friendship (cemented by countless debates & discussions) has been invaluable over the last 5 years. I look to the future of our friendship with great excitement.

I would like to thank all the other members of Jonathan's & Josh's groups who have made the journey a delight. Specificallly, **Giacomo Ferranti, George Atkinson, Alex Belsley, Cyril Torre, Matt Stafford, Giulia Rubino, Andriy Boubriak, Seb Currie, Quinn Palmer, Dario Dominguez** and **Marija Radulovic**. In addi-

tion, I would like to thank **all the other members of the CDT & QetLabs family** of whom their are far to many to mention.

My final thanks go to my **mum & dad** and **brother & sister** for their support. To my partner **Jad**, this achievement is as much yours as it is mine.

Author's declaration

I declare that the work in this dissertation was carried out in accordance with the requirements of the University's Regulations and Code of Practice for Research Degree Programmes and that it has not been submitted for any other academic award. Except where indicated by specific reference in the text, the work is the candidate's own work. Work done in collaboration with, or with the assistance of, others, is indicated as such. Any views expressed in the dissertation are those of the author.

SIGNED: ..... [redacted] ..... DATE: 01/10/22 .....

Journal Articles

1. **J. Biele**, S. Wollmann, J. W. Silverstone, J. C. F. Matthews, & E. J. Allen, "*Maximizing precision in saturation-limited absorption measurements*," Physical Review A, vol. 104, p. 053717, Nov. 2021.

2. **J. Biele**, J. F. Tasker, J. W. Silverstone, & J. C. F. Matthews, "*Shot-noise limited homodyne detection for MHz quantum light characterisation in the 2 μm–band*," Optics Express, vol. 30, p. 7716-7724, Feb. 2022.

Article 1. is reported in chapter 3 and article 2 is reported in chapter 4.

Conference Proceedings

J. W. Silverstone, L. M. Rosenfeld, D. A. Sulway, B. D. J. Sayers, **J. Biele**, G. F. Sinclair, D. Sahin, L. Kling, J. C. F. Matthews, M. G. Thompson, & J. G. Rarity, "*Silicon quantum photonics in the short-wave infrared: A new platform for big quantum optics*", Conference on Lasers & Electro-optics Europe-EQEC 2019 (poster).

J. Biele, J. W. Silverstone, & J. C. F. Matthews, "*Integrated silicon photonic squeezing centered on* 2.1 μm *for applications in sensing & metrology*", Quantum Devices Summer School, Sicily 2019 (poster).

J. Biele, J. W. Silverstone, J. C. F. Matthews, & E. J. Allen, "*The effects of saturation on quantum enhanced absorption spectroscopy*", Bristol Quantum Information Technology Conference, Bristol 2019 (poster).

J. Biele, J. W. Silverstone, J. C. F. Matthews, & E. J. Allen, "*Quantum absorption estimation for saturable samples*", Sensing with Quantum Light Conference, Berlin

2020 (contributed talk).

J. Biele, J. W. Silverstone, J. C. F. Matthews, & E. J. Allen, "*Quantum absorption estimation for saturable samples*", Conference on Lasers and Electro-Optics, San Jose 2021 (poster).

Table of Contents

Page

List of Tables xv

List of Figures xvii

1 Introduction 1
- 1.1 Thesis Outline . . . 6

2 Integrated Quantum Optics 9
- 2.0 Introduction . . . 9
- 2.1 Quantum optics . . . 9
  - 2.1.1 Single-mode quantum optics . . . 11
  - 2.1.2 Displacement operator . . . 18
  - 2.1.3 Modes in free space . . . 18
  - 2.1.4 Linearisation & the sideband picture . . . 19
  - 2.1.5 Beamsplitters . . . 21
- 2.2 Integrated optics . . . 21
  - 2.2.1 Light in a dielectric . . . 22
  - 2.2.2 Waveguides . . . 23
  - 2.2.3 Fiber to chip coupling . . . 25
  - 2.2.4 Directional couplers . . . 25
  - 2.2.5 Thermo-optic phase shifters . . . 26
  - 2.2.6 Integrated beamsplitters . . . 27

3 Shot-noise Limited Homodyne Detection in the 2 μm–band 29
- 3.0 Introduction . . . 29
- 3.1 Homodyne theory . . . 32
  - 3.1.1 Electronic readout . . . 35
- 3.2 Key components and considerations . . . 38
  - 3.2.1 The photodiode . . . 38

3.2.2 Transimpedance amplification . . . 42
3.2.3 Noise considerations . . . 46
3.2.4 Common-mode rejection . . . 48
3.2.5 Power considerations . . . 49
3.3 Component choice and projected performance . . . 49
3.4 Detector design and layout . . . 52
3.5 Device characterisation and vacuum noise detection . . . 54
3.6 Discussion . . . 56
3.7 Characterisation of pulsed laser noise . . . 59
3.8 Conclusion . . . 60

4 An All-optical Noise Reduction Scheme for Integrated Absorption Spectroscopy in the 2 μm-band 63
4.0 Introduction . . . 63
4.1 Noise suppression using Kerr interferometers . . . 66
4.1.1 Kerr nonlinearity . . . 66
4.1.2 Self-phase modulation . . . 66
4.1.3 Pulsed self-phase modulation . . . 67
4.1.4 Self-phase modulation in a Kerr interferometer . . . 70
4.1.5 Quantum analysis of self-phase modulation . . . 72
4.1.6 Quantum evolution of a pulse through a Kerr interferometer 73
4.1.7 Accounting for excess classical noise . . . 78
4.2 Optimal design of an integrated Kerr interferometer . . . 79
4.3 Device characterisation . . . 83
4.4 Measuring noise suppression . . . 86
4.5 Discussion . . . 91
4.5.1 Barriers to pulsed noise suppression in silicon . . . 92
4.6 Conclusion . . . 94

5 Maximising Precision in Saturation-Limited Absorption Spectroscopy 95
5.0 Introduction . . . 95
5.1 Saturation modelling and parameter estimation . . . 97
5.1.1 A Semi-classical model of saturation . . . 97
5.1.2 Fisher information analysis . . . 101
5.2 Semi-classical estimation of absorption under saturation . . . 103
5.2.1 Classical probe performance . . . 104
5.2.2 A bound on single-mode precision . . . 107

5.2.3 Finding an optimal probe . . . 107
5.2.4 The effect of saturation on precision . . . 108
5.2.5 Inefficient detection and probe brightness . . . 109
5.2.6 Amplitude-squeezing: a viable route to enhanced performance . . . 110
5.3 A fully-quantum model of saturation . . . 111
5.3.1 Open-systems modelling . . . 114
5.3.2 A comparison to the semi-classical model . . . 116
5.4 Conclusion . . . 118

6 Conclusion **119**
6.1 In pursuit of integrated 2 µm squeezing for absorption sensing . . . 120
6.2 An outlook on integrated absorption sensing in the MIR . . . 121
6.3 Closing remarks . . . 122

A List of symbols **125**

B Key specifications & parameters **131**
B.1 Pulsed laser specifications . . . 131
B.2 Cornerstone device parameters . . . 132

References **133**

List of Tables

Table		Page
3.1	A list of homodyne detector components by model number.	49
3.2	Homodyne detector component specifications.	51
3.3	A theoretical breakdown of photocurrent noise contributions.	51
4.1	A summary of silicon nitride integrated squeezing results.	65
B.1	A list of 2 µm pulsed laser specifications.	131
B.2	A list of Cornerstone device specifications.	132

List of Figures

Figure **Page**

1.1 Absorption spectra of several prominent absorbing gasses in the 2 µm-5 µm region of the electromagnetic spectrum. 2
1.2 The electromagnetic spectrum with particular reference to the transparency windown of silicon and silicon dioxide. 3
1.3 Nonlinear refraction, nonlinear absorption, and Rayleigh scattering in silicon. These values have been normalised to their value at 1.55 nm . 4

2.1 Wigner representation of the vacuum state and a number state. 15
2.2 A map of non-physical, quadrature squeezed and classical states as defined by their quadrature variance. 16
2.3 Wigner representation of the squeeze vacuum state. 17
2.4 The effect of loss on quadrature squeeing for varying input amounts of squeezing. 22
2.5 TE and TM mode electric field intensity in a strip waveguide. 24
2.6 (a) and (b) schematic of a grating coupler used to couple light into a chip. (c) normalised electric field intensity of a full 3D FDTD simmulation of a balanced directional coupler. 26
2.7 (a) schematic of an MZI beamsplitter, mapping input modes a, b to output modes c, d. (b) the normalised output mode power with applied phase given input into mode a. 27

3.1 A schematic of homodyne detection. 32
3.2 A schematic of an electonic spectrum analyser operating on the hetrodyne principle. 37
3.3 Vertically-illuminated PIN photodiode schematic. 39
3.4 Equivelant electrical model for a photodiode. 41
3.5 DC electrical circuit for transimpedance amplification. 42
3.6 AC electrical circuit for transimpedance amplification. 44
3.7 Photodiode IV curve and resistance under reverse bias. 50

3.8 Simulated homodyne detector (a) gain spetcrum and phase (b) shot-noise clearance for several local oscillator powers. 52
3.9 A 3D render of the homodyne printed circuit board. 52
3.10 Full electrical circuit of the homodyne detector. 53
3.11 Experimental diagram of the homodyne detector charaterisation setup. 54
3.12 (a) the DC response from each photodiode showing total efficiency. (b) is the detector response with the electronic noise subtracted. From this signal we can fit to the gain spectrum. Data acquired with a resolution bandwidth of 100 kHz and video bandwidth of 100 Hz (blue). . 56
3.13 (a) the power spectral density for varying input local oscillator power. The measurement resolution bandwidth is 300 kHz, with a video bandwidth of 10 kHz. A moving point average with a Gaussian kernel has been applied with a FWHM of 1.5 MHz. (b) the average noise variance over the frequency range 1 MHz–13 MHz as a function of incident power (blue). Linear regression has been performed via least-squares giving a fit with $R^2 = 1.00$ (red). 57
3.14 Common-mode rejection ratio at the repetition rate of the laser. 57
3.15 A beakdown of pulsed laser noise into classical noise, shot-noise and detector background noise. 60
3.16 A photograph of the homodyne detector presented in this chapter. . . 61

4.1 Classical pulse propagation under self-phase modulation. 68
4.2 Kerr interferometer schematic and power relations. 71
4.3 Wigner representaion of a coherent state before and after Kerr evolution. 73
4.4 Pulse discretisation and linearisation as performed in the quantum pulsed Kerr propagation model, alongside the equivelent sideband picture. 75
4.5 Expected squeezing from a Cornerstone 1 device assuming a shot-noise limited laser. 78
4.6 Expected classical noise reduction from a Cornerstone 1 device assuming a noisy laser. 80
4.7 Raw pulsed laser spectrum displaying spectral bandwidth. 81
4.8 (a) estimated propagation loss and modal area in Cornerstone as a function of waveguide widtha and (b) expected SPM and output power assuming a waveguide width of 500 nm, propagation loss of −3 dB and input average power of 10 mW. 82
4.9 Cornerstone linear loss and integrated MZI characterisation. 84

4.10 Grating transmission as a function of wavelength. 85
4.11 Nonlinear loss characterisation and SPM from a sprial of length 8.8 cm, for several input pulse powers. 86
4.12 Experimental diagram of the integrated silicon noise suppression scheme 87
4.13 A photo of Cornerstone Sagnac squeezing devices. 88
4.14 Relative intenisty noise with power comparison through (a) an in-out grating structure and (b) a sprial of length 0.64 cm. (c) the RIN spectrum with 40 mW input power. 90
4.15 (a) measured power relations for three Sagnac asymmetric Kerr interferometers with a spiral lenght of 0.58 cm and splitting ratios 94:6 (blue), 80:20 (red) and 63:37 (green). (b) RIN at 3 MHz as a function of input power for each splitting ratio. Data is plotting against the modulation instability corrected RIN from a strip waveguide of equal length (purple) and the laser baseline RIN (black). 91

5.1 A schematic of the direct absorption measurement of the linear absorption coefficient, affected by sample saturation. 98
5.2 Nonlinear sample transmission as derived by population analysis. . . 100
5.3 Precision and efficiency obtained using an optimal quantum probe or a classical probe, calculated across the linear ($\kappa < 1$) and saturated ($\kappa \geq 1$) pump regimes. The quantum advantage $\Gamma(a)$ is also plotted. . . 105
5.4 Probe power reduction achievable by switching from a coherent probe of input intensity κ_c to a Fock state probe, without loss of precision. . 109
5.5 Squeezed state precision $F_s(a)$ normalised by the quantum limit, $\mathcal{Q}(a)$, for several amplitude-squeezing factors. 111
5.6 Coherent and Fock state evolution along a fully-quantum saturable sample. We plot the evolution of the probe state's Fano factor **F** and transmission η, comparing the fully-quantum model to the semi-classical approximation. 117

"It's what we go through that helps us get through."

Oprah Winfrey

Chapter 1

Introduction

Optical sensing exploits light to map information from any given domain to the electrical domain. The history of optical sensing, reliant upon absorbance, emissive and florescence effects, dates back to the 16th century. However, it was not until the advent of the laser in 1960 that the field reached maturity[1]. Absorption-based optical sensing, a broad subset of optical sensing techniques, takes advantage of the discrete, unique, electronic energy spectra of atoms and molecules; a consequence of the laws of quantum physics[2].

Encoded in the position, strength, and shape of each feature within an atomic or molecular absorption spectrum is information about the atomic structure, mass, and bond strengths, along with macroscopic properties of an ensemble such as composition, concentration, temperature, mass flux, velocity and pressure. Due to the vast amount of information obtainable, absorption spectroscopy techniques have enabled many advancements across atomic physics[3], astrophysics[4], molecular[5] & pharmaceutical chemistry[6], and environmental[7] & atmospheric sensing[8], with 12 noble prizes awarded to the development of such techniques across physics and chemistry[9].

Between 2 µm–5 µm, many gasses and biological molecules exhibit fundamental rotational and vibrational features, Fig. 1.1. Crucial to the application of absorption sensors in this region of the spectrum is the deployability of such technologies outside the lab to provide in situ and realtime data streams. Examples of such applications can be found in numerous industries including chemical process monitoring[10–14], climate research[15–18], agricultural monitoring[19–21], and in the medical field, e.g. for breath analysis[22,23]. Each application demands

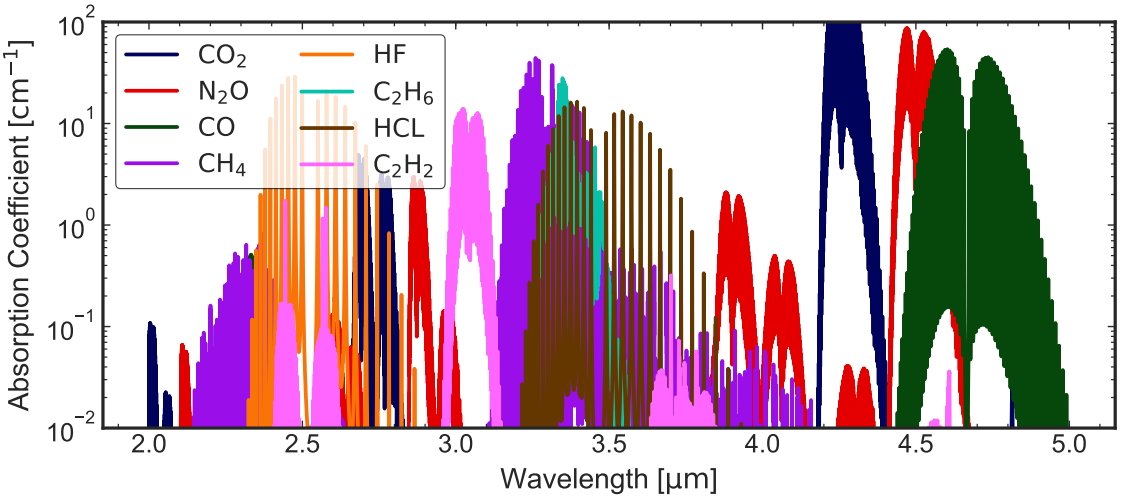

FIGURE 1.1. Absorption spectra of several prominent absorbing gasses in the 2 µm-5 µm region of the electromagnetic spectrum. Data was taken from HITRAN, an open-access online database for molecular absorption coefficients[26]

its own specification and threshold sensitivity with common desirable features seen across the board that include: high stability, low power consumption, mass-manufacturability, low cost, longevity, and high precision[24]. Liu *et al* presents a comprehensive review of all major gas sensing technologies in 2012 and found that although optical methods provide great promise in regards to the desired features listed above, they still represent only a small portion of gas sensors in use, with cost proving to be the main hurdle[25]. Integrated optics, that make use of small photonic integrated circuits, are widely believed to be a promising solution capable of overcoming this hurdle via the economies of scale afforded by billion dollar fabrication houses.

Integrated photonic absorption gas sensors face a number of technical challenges in this region of the spectrum; a platform must be chosen that is not only transparent at the central wavelength, but which also provides low loss propagation, laser & detector integration, and sufficient analyte overlap. Furthermore, enhanced absorption methods, reliant on fast modulation[27–29] or cavity effects[30,31], are often required to provide sufficient sensitivity and place additional demands on a given platforms capabilities. With a transparency window that reaches up to 8 µm (Fig. 1.2)[32], silicon photonic platforms are an obvious first choice as they boast the most advanced fabrication tooling and are already supported by a trillion dollar CMOS industry[33] that has already been utilised to engineer numer-

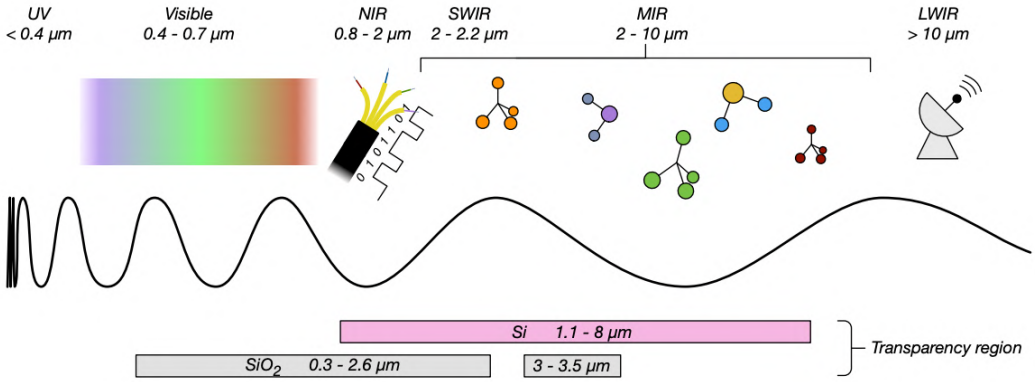

FIGURE 1.2. The electromagnetic spectrum with particular reference to the transparency windown of silicon and silicon dioxide. Figure taken with permission from Ref.[36].

ous breakthrough integrated photonic devices in the pursuit of quantum technologies in the telecoms band[34]. Miller *et al.* reviews progress made in adapting silicon photonics for applications in the mid-infrared[35].

Notable progress towards silicon based integrated, deployable, absorption gas sensors in this region of the spectrum include: the development of a range of MIR monolithic laser technologies Si-integrated via heteroepitaxy[37–39], the development of long wavelength, waveguide-integrated, photodetectors via heterogeneous semiconductor materials[40–42], and progress in exploiting nonlinear optics for the generation of integrated frequency combs for advanced multi-mode techniques such as broadband dual comb spectroscopy[43]. Research is now heavily focused on marrying together these engineering breakthroughs into a singular competitive device[44]. Sensitivity—the minimum detectable change in the target parameter—and precision—the variance across multiple measurements—are also centre stage for any integrated gas sensor that wishes to gain a competitive edge over other non-optical schemes. Therefore, it is informative to look towards the cutting edge of optical metrology, pioneered by the use of quantum states of light[45], to guide the development of sensors capable of unparalleled limits of detection.

The field of quantum optical metrology—interested in the study of non-classical light for enhanced measurement precision and sensitivity—has identified optimal states for parameter estimation as being non-classical states of light: single-photon states[46], multi-photon states[47], or squeezed states[48–50]. In

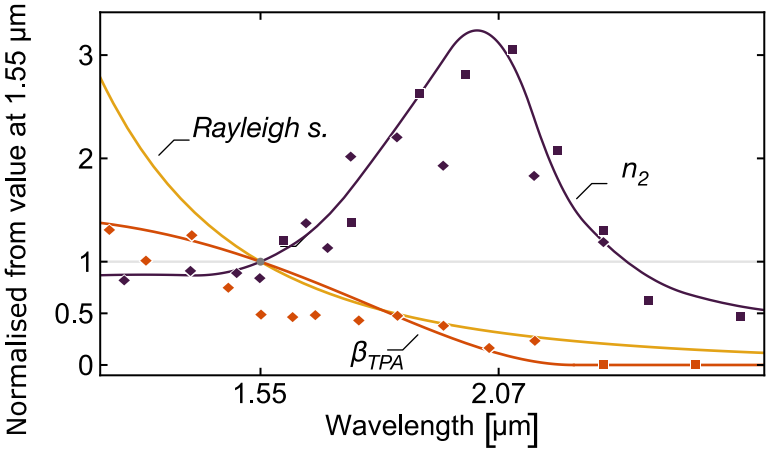

FIGURE 1.3. Nonlinear refraction, nonlinear absorption, and Rayleigh scattering in silicon. These values have been normalised to their value at 1.55 nm. The diamonds and squares are data taken from Z-scan measurements in Refs.[52] and[53]. The blue line, n_2, is a guide for the eye. The red line, β_{TPA}, is plotted using a two-photon absorption model[54]. The graph is taken with permission from Ref.[36].

particular, squeezed states—a resource for reducing the inherent noise within a bright laser beam—are heralded as the most viable route towards a deployable quantum-enhanced sensor as they do not rely on cryogenic temperatures for detection and can provide bright signals. Two key requirements for the production of squeezed states, and indeed all the nonclassical states listed above, are 1) highly nonlinear guiding materials to provide squeezed statistics (see Sec. 2.1.1.4) and 2) low linear and nonlinear losses to preserve high state generation efficiency (see Sec. 2.1.5). In addition to these, low noise high efficiency detection methods—such as homodyne detection (see Sec. 3.1)—are required not only for quantum probe characterisation[51], but also for the optimisation of many optical absorption sensing schemes in which detector efficiency plays a key role in performance.

Historically, telecoms band integrated silicon photonics has utilised a relatively high nonlinear Kerr response to satisfy 1) above (see Sec. 4.1.1 for a description of Kerr nonlinearity). However, at these wavelengths the platform also suffers from high nonlinear loss through a process called two-photon absorption (TPA)[55]. In TPA, two photons are absorbed to produce free carriers that are then able to wreak havoc via broadband free carrier absorption and dispersion[56]. Although TPA can in some instances be a useful property[57,58]—in most scenarios it provides a fundamental limit on the efficacy of silicon for the production of

nonclassical states[59]. Alternative materials with wider band gaps, such as silicon nitride, are a potential solution to alleviating TPA[60,61] at telecom wavelengths. However, silicon nitride displays a lower nonlinear refraction and looser optical confinement meaning far higher pump powers are required to generate the same nonlinearity[36]. Furthermore, variations in the fabrication of silicon nitride across a wafer results in a varied refractive index—a challenge for the scalability of a given technology[62].

A second option is to remain in silicon and shift the working wavelength up the spectrum so as to bring the two-photon energy below the band gap of silicon (~ 1.1 eV). This has the added benefit of shifting towards the application-rich fingerprint region. Figure 1.3 shows the dispersion of the nonlinear TPA coefficient β_{TPA}, nonlinear refractive index n_2, and Rayleigh scattering cross-section. At room temperature silicon displays a two-photon band edge around 2.2 µm where the energy of two photons is insufficient to promote a valance band electron, thus extinguishing TPA. The nonlinear refraction simultaneously has a resonant spike, increasing the efficiency of squeezed state generation. This wavelength band is also comfortably within the transparency range of the commonly used SiO_2 cladding, enabling standard manufacturing processes. At long wavelengths propagation losses are diminished due to reduced Rayleigh scattering from waveguide side-wall roughness[63], and constraints on fabricating sub-wavelength devices become relaxed[64].

Rosenfeld *et al.* have proven the benefits of shifting to longer wavelength in silicon via the first demonstration of single-photon interference above 2 µm[65]. In this thesis, we aim to caplitalise on the enhanced nonlinearity and reduced losses silicon offers at 2.1 µm to develop quantum resources which will pave the way for future quantum-enhanced integrated absorption sensors operating in this region of the spectrum. Crucial resources include, low noise lasers and fast homodyne detection[46,66]. The classical noise and inherent quantum noise within a laser probe fundamentally limits the precision of optical metrology measurements and as such, methods to reduce both noise sources are valuable for enhancing the precision of a given measurement scheme on a per photon basis[45,46]. Once noise is sufficiently suppressed to (and below) the classical limit, low noise, efficient, homodyne detection becomes important for the measurement and verification of the states properties[67,68]. In addition, fast homodyne detectors can be used in conjunction with modulation techniques to shift target information to higher frequencies and thereby circumvent low speed $1/f$ noise present in most sensing schemes[69–71].

At 2 µm, there are currently no shot-noise limited lasers (pulsed or continuous-wave) or high speed homodyne detectors capable of measuring quantum noise. In this thesis we address these shortcomings and develop the first 2 µm homodyne detector with an efficiency > 50% (see Chap. 3)—a key milestone in efficiency that enables the characterisation of exotic quantum states[72]. To address the lack of low noise lasers, we present an all-optical, chip-based, method for the suppression of classical noise within a pulsed 2 µm laser (see Chap. 4). In addition to this, we present theory work that looks to expand our understanding of exactly when it is beneficial to upgrade a classical probe to a quantum probe in absorption spectroscopy. Specifically, we explore the common scenario in which the sample is prone to saturation effects which result in damage at higher probe power[73,74]. In this scenario, we find the obtainable precision is naturally limited by saturation, an effect that we prove can be mitigated via nonclassical states of light (see Chap. 5).

1.1 Thesis Outline

Here I give an overview of the topics discussed in this thesis. Each chapter starts with a declaration of my contribution which details the specific work I have performed for each.

Chapter 2 is an introductory theory chapter covering relevant material in quantum optics (Sec. 2.1) and integrated optics (Sec. 2.2). Quantum optics includes an introduction of quantum electrodynamics (Sec. 2.1), single-mode states (Sec. 2.1.1) and their properties & representations, continuous-mode states (Sec. 2.1.3, and linearisation as a working model for the output state of a continuous-wave laser (Sec. 2.1.4). Integrated optics covers guided modes in waveguides (Sec. 2.2.1), the working principles of key components (Sec. 2.2.3, 2.2.4 & 2.2.5) and integrated beamsplitters (Sec. 2.2.6).

Chapter 3 presents the working principles of homodyne detection (Sec. 3.1), key components required for homodyne detection (Sec. 3.2), simulation & design considerations of building an efficient, fast, homodyne detector for quantum noise characterisation at 2 µm (Sec. 3.4), and the characterisation of the engineered device (Sec. 3.5). Specifically, we discuss homodyne theory for the measurement of continuous-wave (Sec. 3.1.0.1) & pulsed vacuum noise (Sec. 3.1.0.2), and electronic readout of homodyne detection via an electrical spectrum analyser (Sec. 3.1.1.1). We discuss the working principles of the photodiode (Sec. 3.2.1), transimpedance amplification (Sec. 3.2.2), and relative noise considerations for quantum measurements (Sec. 3.2.3). We then build and characterise a homodyne

detector (Sec. 3.5), discussing its performance and impact in the wider field (Sec. 3.6).

Chapter 4 moves on to present work on an integrated all-optical noise suppression scheme for pulsed light. In this chapter we utilise the detector built in the previous chapter to asses noise suppression. We start by introducing noise suppression using Kerr interferometers (Sec. 4.1). In this section we cover Kerr nonlinearity (Sec. 4.1.1), self-phase modulation (SPM) (Sec. 4.1.2), pulsed SPM (Sec. 4.1.3), SPM in a Kerr interferometer (Sec. 4.1.7), and quantum SPM (Sec. 4.1.5). We model the evolution of a shot-noise limited pulse laser through a Kerr interferometer and simulate the expected squeezing resultant from the device (Sec. 4.1.6). The model is adapted to include classical noise and we present the expected classical noise reduction from the device (Sec. 4.1.7). We then move on to discuss the optimal design for maximal noise suppression under 2 µm operation (Sec. 4.2). Previously fabricated devices are then characterised (Sec. 4.3) and noise suppression is measured in comparison to strip waveguide propagation (Sec. 4.4), followed by a discussion and conclusion (Sec. 4.5).

Chapter 5 looks to expand the applicability of quantum states of light in integrated absorption spectroscopy. We present a theory project which models expected precision on estimates of linear absorption through a sample that displays saturation. A semi-classical model of saturation is built (Sec. 5.1) and we employ Fisher information (Sec. 5.1.2) as a tool to quantify and compare the performance of different classical (Sec. 5.3.2) and quantum states of light (Sec. 5.2.6). We present classical probe performance under saturation, giving a few examples of how this result can be applied to existing measurement schemes to enhance performance (Sec. 5.2.1 & 5.2.1.1). We then motivate the use of quantum states of light by deriving a bound on the achievable precision from any single-mode state (Sec. 5.2.2) and proving that Fock states saturate this bound (Sec. 5.2.3). We discuss the required probe brightness for a given target precision for both quantum and classical strategies (Sec. 5.2.5) and introduce squeezed states as a viable route to experimental realisation (Sec. 5.2.6). Finally, we present a fully-quantum model (Sec. 5.3) which we solve numerically, commenting on the validity and applicability of the analytical semi-classical results (Sec. 5.3.2).

Chapter 6 ends the thesis with concluding remarks on a potential viable route to 2 µm integrated silicon squeezing for absorption spectroscopy which overcomes the issues uncovered during this PhD (Sec. 6.1) and a more general discussion on the future of integrated absorption spectroscopy in the 2 µm–band (Sec. 6.2).

Chapter 2

Integrated Quantum Optics

Declaration of contribution: *this chapter covers key concepts required for the rest of the thesis and does not present new research.*

In this chapter we cover key concepts on which the rest of the thesis relies upon. These are broken down into two sections. Section 2.1 gives an overview of quantum optics theory, introducing some key optical states. Section 2.2 then follows on to introduce integrated optics, summarising how we can use photonic chips to manipulate light. Each of the following chapters then builds upon these concepts, introducing additional theory as required for each main result.

2.1 Quantum optics

In classical optics, the dynamics of an electromagnetic field propagating in free space which contains no charges is well described by two vector-valued fields: the electronic, $\mathbf{E}(\mathbf{r}, t)$, and magnetic fields, $\mathbf{B}(\mathbf{r}, t)$, obeying[75]:

$$\begin{aligned} \nabla \cdot \mathbf{B} &= 0, \qquad \nabla \times \mathbf{E} = -\mu_0 \frac{\partial \mathbf{B}}{\partial t}, \\ \nabla \cdot \mathbf{E} &= 0, \qquad \nabla \times \mathbf{B} = \epsilon_0 \frac{\partial \mathbf{E}}{\partial t}. \end{aligned} \tag{2.1}$$

Here, ϵ_0 and μ_0 are the electric and magnetic permeability of free space. These four, first order, differential equations that couple two fields, can be conveniently recast via the following substitution into a single second-order differential equation for one field via:

$$\mathbf{E} \equiv -\frac{\partial \mathbf{A}}{\partial t}, \qquad \mathbf{B} \equiv \frac{1}{\mu_0} \nabla \times \mathbf{A}, \qquad \nabla \cdot \mathbf{A} \equiv 0, \tag{2.2}$$

where **A** is coined the vector field. Note that the last equation in 2.2 is sufficient but not necessary to reproduce Eqs. 2.1. It reflects the invariant nature of **A** to additional arbitrary scalar fields. By choosing to set the divergence to zero, known as the Coulomb gauge, we ensure field values are dependent only on their instantaneous values, a useful property in quantum analysis. Utilising vector calculus identities, we can now express Eqs. 2.1 as:

$$\nabla^2 \mathbf{A} - \frac{1}{c^2} \frac{\partial^2 \mathbf{A}}{\partial t^2} = 0, \tag{2.3}$$

where $c = (\epsilon_0 \mu_0)^{-1/2}$ is the speed of light in free space. Eq. 2.3 is known as the electromagnetic wave equation[76]. A general solution to this equation may be written as a linear combination of possible plane wave solutions:

$$\boldsymbol{A}(\boldsymbol{r}, t) = \sum_k \boldsymbol{A}_k e^{i(\boldsymbol{k}\cdot\boldsymbol{r} - \omega_k t)}. \tag{2.4}$$

Each solution, k, represents a different electromagnetic 'mode' with amplitude vector $\mathbf{A}_k$, wave vector $\mathbf{k}$, and associated frequency $\omega_k = c|\mathbf{k}|$, all defined by the initial and boundary conditions of a particular propagation. As measurable quantities, **E** and **B** must be real-valued vector fields. As such, we require $\mathbf{A}_{-k} = \mathbf{A}_k^*$. We can therefore further expand **A** into:

$$\boldsymbol{A}(\boldsymbol{r}, t) = \sum_k \left(\boldsymbol{A}_k e^{i(\boldsymbol{k}.\boldsymbol{r} - \omega_k t)} + \boldsymbol{A}_k^* e^{i(\omega_k t - \boldsymbol{k}.\boldsymbol{r})} \right). \tag{2.5}$$

We can apply this anzatz to find a general solution to the wave equation for a field propagating along z in a reflective box of cubic volume L^3 to obtain[56]:

$$\boldsymbol{A}(\boldsymbol{r}, t) = \sum_k \left(\frac{\hbar}{2\omega_k \varepsilon_0 L^3} \right)^{1/2} \boldsymbol{e}^{\lambda} \left[a_k \mathrm{e}^{i(\boldsymbol{k}.\boldsymbol{r} - \omega_k t)} + a_k^* \mathrm{e}^{i(\omega_k t - \boldsymbol{k}.\boldsymbol{r})} \right]. \tag{2.6}$$

Here, $\boldsymbol{e}^{\lambda} \in \hat{\boldsymbol{x}}, \hat{\boldsymbol{y}}$ representing the unit polarisation vector. Applying boundary conditions gives $\mathbf{k} = 2\pi/L(n_x, n_y, n_z)$ which defines the allowed wave vectors with $n_x, n_y, n_z = 0, \pm 1, \pm 2....$ In this equation, a_k and a_k^* are complex scalar Fourier amplitudes that are defined to be dimensionless via the preceding normalisation

factor. Quantisation is achieved by recognising these amplitudes as mutually adjoint quantum operators that obey the following bosonic commutation relations:

$$[\hat{a}_k, \hat{a}_{k'}] = [\hat{a}_k^\dagger, \hat{a}_{k'}^\dagger] = 0, \qquad [\hat{a}_k, \hat{a}_{k'}^\dagger] = \delta_{kk'}, \tag{2.7}$$

such that we have:

$$\hat{\boldsymbol{A}}(\boldsymbol{r}, t) = \sum_k \left(\frac{\hbar}{2\omega_k \epsilon_0 L^3}\right)^{1/2} \boldsymbol{e}^\lambda \left[\hat{a}_k \mathrm{e}^{i(\boldsymbol{k}.\boldsymbol{r}-\omega_k t)} + \hat{a}_k^\dagger \mathrm{e}^{i(\omega_k t - \boldsymbol{k}.\boldsymbol{r})}\right]. \tag{2.8}$$

Quantisation in this manner ensures the quantum description of each mode of the electromagnetic field obeys a simple harmonic model with unit mass in which the classical canonical structure of the coordinate system, position and momentum, are adapted to reflect the quantum uncertainty principle[77]. The dynamics of the electric field amplitudes are now described by an ensemble of independent harmonic oscillator modes. The quantum state of each mode may now be discussed independently of one another with each state described by a state vector of the Hilbert space appropriate to that mode. The classical vector potential for a given single-mode state is recovered via the expectation of the vector potential operator. The state of the entire field is then defined in the tensor product space across all modes.

The classical Hamiltonian for the field is given by[75]:

$$H = \frac{1}{2}\int (\epsilon_0 |\mathbf{E}|^2 + \mu_0 |\mathbf{B}|^2)\mathbf{dr}. \tag{2.9}$$

Substituting Eq. 2.8 into Eqs. 2.2, and using those to solve for $\hat{H}$ via Eq. 2.9, we get:

$$\hat{H} = \sum_k \hbar\omega_k \left(\hat{a}_k^\dagger \hat{a}_k + \frac{1}{2}\right). \tag{2.10}$$

This quantum Hamiltonian is the sum over the number of quanta in each harmonic oscillators mode, each of which now has a nonzero vacuum point energy of $\frac{1}{2}\hbar\omega$[78].

2.1.1 Single-mode quantum optics

We now drop the summation over modes and consider a single mode of the quantum harmonic oscillator with governing Hamiltonian:

$$\hat{H} = \hbar\omega \left(\hat{a}^\dagger \hat{a} + \frac{1}{2}\right). \tag{2.11}$$

We can represent any state of a single mode via a decomposition into any complete orthogonal set of basis states that span the Hilbert space. We now cover a few important examples of such decompositions.

2.1.1.1 Number states

The operator product $\hat{a}^\dagger \hat{a}$ has special significance and is called the number operator, denoted $\hat{n}$. We denote $|n\rangle$ to be eigenstates of the Hamiltonian defined by:

$$\hat{H}|n\rangle = E_n|n\rangle \tag{2.12}$$

It follows via the commutation relations for $\hat{a}$ and $\hat{a}^\dagger$ that

$$\begin{aligned} \hat{a}\hat{H}|n\rangle &= (E_n - \hbar\omega)|n\rangle\,, \\ \hat{a}^\dagger\hat{H}|n\rangle &= (E_n + \hbar\omega)|n\rangle\,. \end{aligned} \tag{2.13}$$

We see that $\hat{a}$ and $\hat{a}^\dagger$ act to lower or raise the total energy, or number of photons, by one respectively; this is why they are referred to as the 'annihilation' and 'creation' operators[56]. The eigenstates $|n\rangle$, with $n \in \mathbb{N}^+$, are thus called the photon number states with the vacuum defined by $\hat{a}|0\rangle = 0$. Together, the number states form a complete and orthogonal set of states for the single mode Hilbert space, known as the Fock basis[77]. The action of the creation and annihilation operators is summarised by:

$$\begin{aligned} \hat{a}|n\rangle &= \sqrt{n}\,|n-1\rangle\,, \\ \hat{a}^\dagger|n\rangle &= \sqrt{n+1}\,|n+1\rangle\,. \end{aligned} \tag{2.14}$$

Since $\hat{a}$ and $\hat{a}^\dagger$ are not Hermitian operators, they do not correspond to measurable quantities. Furthermore, the number states, though well defined energy states, are not states with well defined electric field since $\langle n|\hat{E}|n\rangle \propto \langle n|\hat{a} + \hat{a}^\dagger|n\rangle = 0$[77] i.e. the mean electric field of such states is always zero. It is more convenient to consider the following measurable operators, $\hat{x}$ and $\hat{p}$; these are deeply related to the notion of classical position and momentum in a simple harmonic oscillator:

$$\hat{x} = \frac{1}{2}(\hat{a} + \hat{a}^\dagger), \qquad \hat{p} = \frac{i}{2}(\hat{a}^\dagger - \hat{a}), \tag{2.15}$$

referred to as the position and momentum operators[78]. By observation, we can immediately see that $\hat{x}$ is directly proportional to the electric field, and conversely $\hat{p}$ is directly proportional to the magnetic field (or momentum of a classical harmonic oscillator). The commutator relation between these two conjugate variables is:

$$[\hat{x}, \hat{p}] = \frac{i}{2}, \tag{2.16}$$

Using the uncertainty principle, which relates the variance of the probability distributions obtained from multiple measurements of each variable for a given state, we get:

$$\Delta\hat{x}\Delta\hat{p} \geq \frac{[\hat{x},\hat{p}]}{2i} = \frac{1}{4}. \tag{2.17}$$

Here, the variance is given by $\Delta\hat{\bullet} \equiv \sqrt{\langle \bullet^2 \rangle - \langle \bullet \rangle^2}$. Any state which saturates this bound is known as a minimum uncertainty state. For a number states, we have:

$$\Delta\hat{x} = \Delta\hat{p} = \frac{(2n+1)}{2}, \tag{2.18}$$

therefore $|0\rangle$ is a minimum uncertainty state[77].

2.1.1.2 Coherent states

In order to have a nonzero electric field expectation, a superposition state with more than one number state is required. Such a state can be considered as the right eigenstates of the annihilation operator, denoted $\hat{\alpha}$ such that $\hat{a}|\alpha\rangle = \alpha|\alpha\rangle$ where $\alpha \in \mathbb{C}$ with $\alpha = |\alpha|e^{i\vartheta}$. Conversely, the left eigenstates of the creation operator is given by $\langle\alpha|\hat{a}^\dagger = \alpha^* \langle\alpha|$. These states, known as coherent states, are useful as their properties constitute a very good approximation to the quasi-monochromatic states emitted by a narrow-band continuous-wave laser[78]. The coherent state decomposition in the number basis is given by[77]:

$$|\alpha\rangle = \exp\left(-\frac{1}{2}|\alpha|^2\right)\sum_{n=0}^{\infty}\frac{\alpha^n}{\sqrt{n!}}|n\rangle. \tag{2.19}$$

The coherent state is of importance as it provides the correct classical form of the electric field expectation value whilst also including minimum uncertainty vacuum fluctuations. It is interesting to note that $\langle\alpha|\beta\rangle \neq 0$ meaning coherent states are not an orthogonal set of states, however, their overlap decays exponentially with their complex separation.

The photon number statistics of the coherent state are found to be Poissonian, i.e. their mean is equal to their variance:

$$\langle\alpha|\hat{n}|\alpha\rangle = \Delta\hat{n} = |\alpha|^2, \tag{2.20}$$

with a distribution given by:

$$P(n) = |\langle n \mid \alpha\rangle|^2 = \frac{e^{\frac{-|\alpha|^2}{2}}|\alpha|^2}{\sqrt{n!}}. \tag{2.21}$$

Phenomenologically speaking, each photon inside a laser undergoes many independent interactions with excited two-level systems within the gain medium.

Each interaction results in the combined state of the photon-atom entering a superposition of stimulated emission (2 photons) or no stimulated emission event (1 photon). Taking this interaction to a reasonable limit of infinite interactions leads to Poissonian-distributed photon statistics and is the reason why the coherent state is a good approximation to the output of a continuous-wave laser[79].

2.1.1.3 State representation

The orthogonality of the two quadrature operators can be utilised as coordinates to define a 2D space in which all single-mode states can be represented—known as phase space. Under simple plane wave evolution of the mode, we can redefine the phase space axes to be in the rotating frame of the mode such that the state representation remains stationary as time evolves. Propagation along z then leads to the state representation rotating about the origin with phase e^{ikz}. In phase space, the position and momentum quadratures are often referred to as the amplitude and phase quadrature, respectively. This renaming stems from the fact that direct measurement of the electric field intensity via a photodiode gives a current that is directly proportional to the position quadrature[80]. Due to the uncertainty relation given in Eq. 2.16, each space will be represented by a distribution rather than a singular point. There are a number of intuitive ways to define such a distribution via the expectation of each quadrature. Here we make use of the Wigner representation defined by[81]:

$$W(x,p) = \frac{1}{2\pi}\int_{-\infty}^{\infty} \left\langle x - \frac{y}{2}\middle|\hat{\rho}\middle|x + \frac{y}{2}\right\rangle e^{iyp}\mathrm{d}y, \tag{2.22}$$

in which $\hat{\rho}$ is now a density matrix describing the single mode state $|\psi\rangle$ via $\hat{\rho} = |\psi\rangle\langle\psi|$. The Wigner function shares many properties with a joint probability distribution over (x,p) with $\int_{-\infty}^{\infty}\int_{-\infty}^{\infty} W(x,p)\mathrm{d}x\mathrm{d}p = 1$ and with the marginal distributions for a given state calculated via:

$$P(x) = \langle x|\hat{\rho}|x\rangle = \int_{-\infty}^{\infty} W(x,p)\mathrm{d}p, \qquad P(p) = \langle p|\hat{\rho}|p\rangle = \int_{-\infty}^{\infty} W(x,p)\mathrm{d}x. \tag{2.23}$$

Though the uncertainty principle forbids explicit measurement of the Wigner function, it can be used to calculate the distribution of a measurement of a given quadrature. It is possible to have a negative-valued Wigner function, however, the marginal distributions remain positive and thus the Wigner function is referred to as a quasi-probability distribution. Highly non-classical states of light often display such a Wigner function with a key example being a pure Fock state, Fig. 2.1(b)[72].

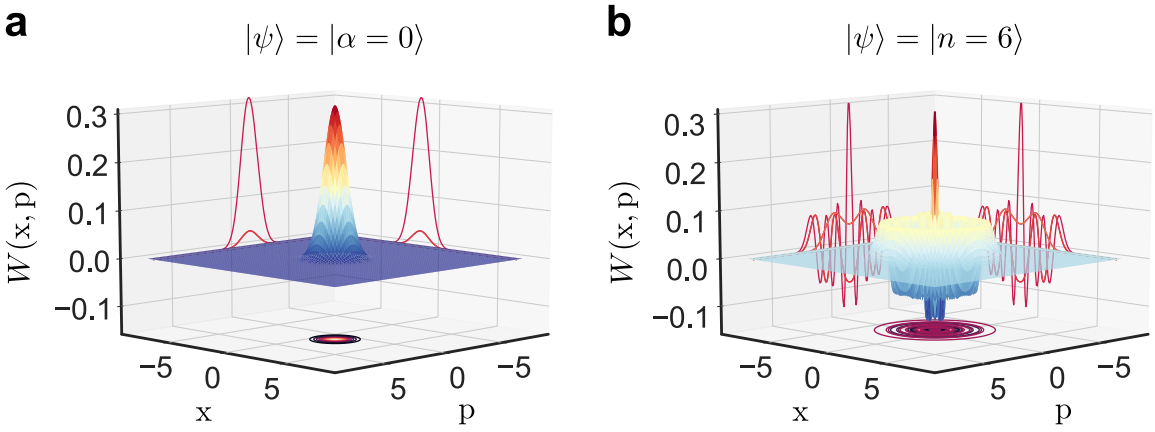

FIGURE 2.1. Wigner representation of (a) the vacuum state and (b) a number state with 6 photons. Each Wigner function has its marginals projected onto the X and P quadratures shown in red lines.

The Wigner function of a coherent state and Fock state are given by:

$$W(x,p) = \frac{1}{\pi} e^{-(x-x_0)^2-(p-p_0)^2}, \qquad W(x,p) = \frac{(-1)^n}{\pi} L_n\left[2\left(x^2+p^2\right)\right] e^{-x^2-p^2}, \quad (2.24)$$

respectively, where $L_n[x] = \sum_{k=0}^{n} \frac{n!}{k!(n-k)!} \frac{(-1)^k}{k!} x^k$ are the L'eguerre polynomial functions[77]. The figure above plots the Wigner function in phase space for both the coherent vacuum state and a pure number state containing 6 photons. We can see that the number state Wigner function is symmetric across all quadratures suggesting the state has no well-defined notion of phase. The Wigner function also drops below zero in comparison to the Gaussian-shaped positive Wigner function of the vacuum. Other quasi-probability distributions that can be used to describe quantum states are the Husimi Q representation and the Glaube-Sudarshan P representation[56]. In this thesis, we will stick to the Wigner representation.

2.1.1.4 Squeezed states

A state is defined as quadrature squeezed if the variance of any quadrature is less than one half[78]. Figure 2.2, below, depicts where squeezed states are located on a map of amplitude and phase quadrature variance. Note that this is only one such fixed set of orthogonal quadratures, with a state being said to be quadrature squeezed for any quadrature phase with variance less than one half.

Squeezing can be generated by any process that mixes the input mode opera-

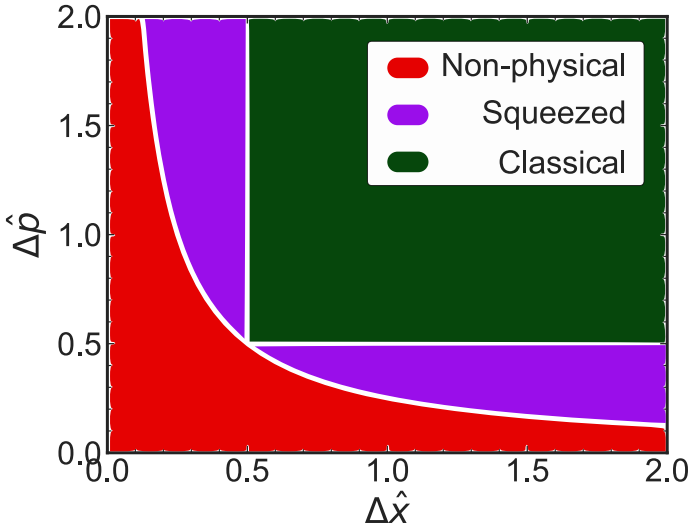

FIGURE 2.2. A map of non-physical, quadrature squeezed and classical states as defined by the multiplication of their quadrature variances.

tors $\hat{a}$ or $\hat{a}^\dagger$ into a combination that obeys:

$$\begin{aligned} \hat{a} &\mapsto u\hat{a} + v\hat{a}^\dagger, \\ \hat{a}^\dagger &\mapsto u\hat{a}^\dagger + v\hat{a}, \end{aligned} \tag{2.25}$$

such that $u^2 - v^2 = 1$[82]. We can consider how a time-independent Hamiltonian, $\hat{H}$, maps an operator in the Heisenberg picture of quantum mechanics. The Schrodinger equation states that $|\psi\rangle$ is mapped to $|\psi'\rangle$ via $|\psi'\rangle = \hat{U}|\psi\rangle$ where $\hat{U} = \exp(-i\hat{H}t/\hbar)$. As such, the expectation of a given operator of interest, $\hat{A}$, as measured on the output state, is given by:

$$\langle \hat{A} \rangle = \langle \psi | \hat{U}^\dagger \hat{A} \hat{U} | \psi \rangle. \tag{2.26}$$

The operation may therefore be considered to map the operator via $\hat{A} \mapsto \hat{U}^\dagger \hat{A} \hat{U}$.

To generate the required map, presented in Eq. 2.25, for squeezed statistics, it can be proven that a quadratic term in creation or annihilation is required in the generating Hamiltonian[82]. In practice, this mapping is provided by nonlinear optics phenomena in which two or more fields are mixed together[83]. A prototype Hamiltonian of the form:

$$\hat{H} = \frac{i\hbar}{2}(z\hat{a}^2 - z^*\hat{a}^{\dagger 2}), \tag{2.27}$$

can be considered in which $z = re^{i\theta}$ dictates the relative magnitude and quadrature phase of the produced squeezing. We can act the associated squeezing op-

erator, $\hat{S}(z)$, on both the annihilation and creation operators to give[78]:

$$\hat{S}(z)^\dagger \hat{a} \hat{S}(z) = \hat{a}\cosh(r) - \hat{a}^\dagger e^{i\theta}\sinh(r), \text{ and } \hat{S}(z)^\dagger \hat{a}^\dagger \hat{S}(z) = \hat{a}^\dagger \cosh(r) - \hat{a}e^{-i\theta}\sinh(r). \tag{2.28}$$

The Hamiltonian given above is of importance as it governs prominent nonlinear optics interactions, such as degenerate parametric down conversion and four-wave mixing, often used as a practical means to create squeezing[84]. We can produce a squeezed-coherent state by first squeezing the vacuum and then displacing it via a coherent displacement. The resulting state, $|\alpha, z\rangle$, has the following statistics:

$$\begin{aligned} \langle \hat{x} \rangle &= \sqrt{2}|\alpha|\cos(\vartheta), \qquad (\Delta\hat{x})^2 = \frac{1}{2}\left[e^{2r}\sin^2\left(\frac{\theta}{2}\right) + e^{-2r}\cos^2\left(\frac{\theta}{2}\right)\right], \\ \langle \hat{p} \rangle &= \sqrt{2}|\alpha|\sin(\vartheta), \qquad (\Delta\hat{p})^2 = \frac{1}{2}\left[e^{2r}\cos^2\left(\frac{\theta}{2}\right) + e^{-2r}\sin^2\left(\frac{\theta}{2}\right)\right]. \end{aligned} \tag{2.29}$$

Figure 2.3 shows the associated Wigner functions plotted for this type of squeezed state with $z = 1$ and $z = i$ for comparison. With a squeezing angle of zero, the quadrature of minimum uncertainty is aligned along the $\hat{x}$ quadrature. For a general squeezing angle θ, the minimum uncertainty quadrature is orientated along $\theta/2$ in phase space—as can be seen in Fig. 2.3(b) for $\theta = \pi/2$.

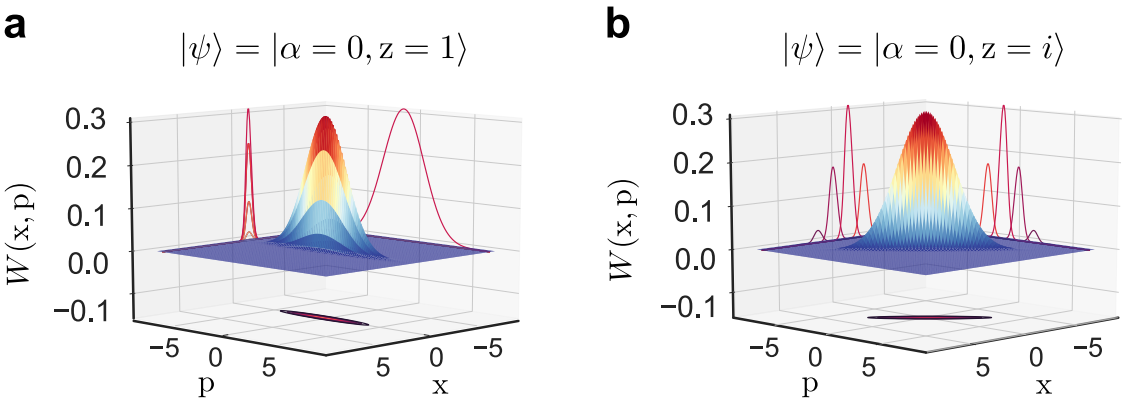

FIGURE 2.3. Wigner representation of (a) the squeezed vacuum state with $z = 1$ and (b) the squeezed vacuum state with $z = i$. Each Wigner function has its marginals projected onto the X and P quadratures shown in red lines.

The photon number statistics of the coherent-squeezed state are given by:

$$\begin{aligned} \langle \hat{n} \rangle &= |\alpha|^2 + \sinh^2(r) \\ (\Delta\hat{n})^2 &= |\alpha|^2\left(e^{2r}\sin^2\left(\vartheta - \frac{1}{2}\theta\right) + e^{-2r}\cos^2\left(\vartheta - \frac{1}{2}\theta\right)\right) + 2\sinh^2(r)\left(\sinh^2(r) + 1\right). \end{aligned} \tag{2.30}$$

By observation of Eq. 2.30, we see that for specific values of squeezing angle and strength, the state displays sub-Poissonian statistics. For the specific case of amplitude squeezed light, we have:

$$\begin{aligned}(\Delta\hat{n})^2 &= |\alpha|^2 e^{-2r} + 2\sinh^2(r)\left(\sinh^2(r)+1\right),\\ (\Delta\hat{x})^2 &= \frac{e^{-2r}}{2}.\end{aligned} \tag{2.31}$$

By comparison of these two variances, the amount of amplitude squeezing becomes synonymous with the amount of photon number squeezing in the limit of $|\alpha| \gg r$ i.e. e^{-2r}. In the rest of this thesis, unless stated otherwise, we use bright amplitude squeezing synonymously with photon number squeezing.

In the next chapter we will use this type of squeezed state to suggest a viable route towards enhanced absorption sensing of delicate samples. In chapter 4 we introduce a different type of squeezing Hamiltonian generated by the process of self-phase modulation.

2.1.2 Displacement operator

In the Heisenberg picture of quantum mechanics, we can generate coherent states by acting an the coherent state in much the same way the squeezing operator acts on creation and annihilation operators to produce squeezing. The operator is know as the displacement operator since it can be visualised as applying a vector displacement to the position of the vacuum state in quadrature space, whilst leaving the states statistics unchanged. The displacement operator is defined by[78]:

$$\hat{D}(\alpha) = \exp(\alpha\hat{a}^\dagger - \alpha^*\hat{a}) \tag{2.32}$$

and maps the creation and annihilation operators like:

$$\hat{D}(\alpha)^\dagger \hat{a}\hat{D}(\alpha) = \hat{a} + \alpha, \text{ and } \hat{D}(\alpha)^\dagger \hat{a}^\dagger \hat{D}(\alpha) = \hat{a}^\dagger - \alpha. \tag{2.33}$$

2.1.3 Modes in free space

In Section 2.1, we make the assumption that the electric field is contained in some box of finite volume which leads to a discrete set of supported modes. In free space propagation, confinement along the direction of propagation z is extended to infinite whilst the field remains confined in the perpendicular plane. This leads to a continuous space of supported frequencies with the summation in Eq. 2.6 replaced with an integral[78]:

$$\sum_k \to \frac{1}{\Delta\omega}\int d\omega, \quad \delta_{k,k'} \to \Delta\omega\,\delta\left(\omega-\omega'\right), \tag{2.34}$$

where $\Delta\omega = 2\pi c/L \to 0$ in the spacing between modes which approaches zero in the limit of infinite confinement and is required to ensure the correct normalisation. In the continuous picture, the bosonic operators map to:

$$\hat{a}_k \to \sqrt{\Delta\omega}\,\hat{a}(\omega) \quad \text{and} \quad \hat{a}_k^\dagger \to \sqrt{\Delta\omega}\,\hat{a}^\dagger(\omega), \tag{2.35}$$

and as such, are no longer dimensionless quantities. This renormalisation ensures the following standard commutation relations:

$$\left[\hat{a}(\omega), \hat{a}\left(\omega'\right)^\dagger\right] = \delta\left(\omega - \omega'\right) \quad \text{and} \quad \left[\hat{a}(\omega), \hat{a}\left(\omega'\right)\right] = 0. \tag{2.36}$$

Putting this all together gives:

$$\hat{\boldsymbol{A}}(\boldsymbol{r}, t) = \left(\frac{\hbar}{4\pi c\varepsilon_0 A}\right)^{1/2} \boldsymbol{e}^\lambda \int \left[\hat{a}(\omega) \mathrm{e}^{i(\boldsymbol{k}.\boldsymbol{r} - \omega_k t)} + \hat{a}^\dagger(\omega) \mathrm{e}^{i(\omega_k t - \boldsymbol{k}.\boldsymbol{r})}\right] \mathrm{d}\omega. \tag{2.37}$$

Under the condition that the bandwidth of an excitation is much smaller than its central frequency, we can define the Fourier transform of the continuous mode creation and annihilation operators via:

$$\hat{a}(t) = \int_{-\infty}^{\infty} \hat{a}(\omega) e^{-i\omega t} d\omega, \quad \hat{a}(\omega) = \int_{-\infty}^{\infty} \hat{a}(t) e^{i\omega t} dt. \tag{2.38}$$

As such, we see that the vector potential can be considered as a continuous set of time dependent modes. It follows that $\hat{a}^\dagger(\omega) = \left[\hat{a}(-\omega)\right]^\dagger$. This will be a useful property that we will use in the following discussion on the sideband picture.

2.1.4 Linearisation & the sideband picture

In the main results of this thesis, we will rely on linearisation as a method for propagating continuous mode quantum noise through optical components. In linearisation, we utilise the Heisenberg picture of quantum mechanics to represent a narrow-band quantum state, $\hat{A}(t)$, as the sum of its classical mean value, given by $\left\langle \hat{A}(t) \right\rangle = \langle 0| \hat{D}^\dagger(\alpha) \hat{A}(t) \hat{D}(\alpha) |0\rangle = \alpha(t)$ (for a coherent state carrier), and a small quantum fluctuation, $\hat{a}(t)$, such that[80]:

$$\hat{A}(t) = \langle \hat{A}(t) \rangle \hat{I} + \hat{a}(t) = \alpha(t)\hat{I} + \hat{a}(t). \tag{2.39}$$

Here, $\hat{A}(t)$ is defined in a frame that rotates in phase space at the speed of the carrier frequency, ω_0. As we are operating in the Heisenberg picture, the expectation taken above is over the initial state—the vacuum—with the displacement operator evolving the continuum of quantum modes. Statistical variations are accounted for via the second term $\hat{a}(t)$ which may have some initial continuum

state that is not the vacuum to reflect any additional noise or modulations present at frequencies about the narrow-band carrier accounted for by $\langle \hat{A}(t) \rangle$.

This representation is powerful as it allows us to more easily consider the dynamics of both signals and noise as they propagate through a system. Additionally, the representation leads to an intuitive description of quantum noise in Fourier space, the space often measured in experiments. Crucial to the approximation of linearisation is the assumption that the central frequency bandwidth is much less than the central frequency such that all other frequencies can be considered to be in orthogonal, well-defined, modes. As a simple example, we consider straight detection via a photodiode which measures intensity via the number operator $\hat{N}(t) = \hat{A}^\dagger(t)\hat{A}(t)$. We consider the initial state to be a continuous-wave laser well approximated by a coherent state and sufficiently narrow-band such that linearisation holds and $\langle \hat{A}(t) \rangle = \alpha \in \mathbb{R}$. In this case, all other frequencies about the carrier can be considered to be in the vacuum state. To first order, we get:

$$\hat{N}(t) = \alpha^2 + \alpha \hat{x}(t), \tag{2.40}$$

The quantum fluctuations in the intensity measurement stem from the continuous mode equivalent of the position quadrature. We can take the Fourier transform of this to analyse the spectrum of the detected current:

$$\begin{aligned} \hat{N}(\Omega) &= \delta(\Omega)\alpha^2 + \alpha\big(\hat{a}^\dagger(\Omega) + \hat{a}(\Omega)\big), \\ &= \delta(\Omega)\alpha^2 + \alpha\hat{x}(\Omega), \\ &= \delta(\Omega)\alpha^2 + \alpha\big([\hat{a}(-\Omega)]^\dagger + \hat{a}(\Omega)\big). \end{aligned} \tag{2.41}$$

Here, $\Omega = \omega - \omega_0$ as we are in the rotating frame of the carrier. The DC peak at $\omega = \omega_0$ corresponds to the average power from the carrier. The last equality highlights an important point—measurements of a given quadrature at frequency Ω contain components from both the positive and negative sidebands symmetric about the carrier. Therefore, in frequency space, we can consider the dynamics of the state to be captured by a static DC component and noise in symmetric sidebands. We will see in chapter 4 that squeezed statistics are a result of partial correlations across these sidebands introduced by nonlinear effects.

We can further take the variance of this signal to give:

$$\mathrm{Var}(\hat{N}(\Omega)) = \alpha^2 \langle 0 \big| \hat{x}(\Omega)^2 \big| 0 \rangle . \tag{2.42}$$

This equation tells us that the PSD of the intensity noise in a coherent state is linear in state amplitude, white, and generated by vacuum amplitude quadrature fluctuations in sideband modes about the carrier. We will use linearisation

in chapter 4 to consider how fluctuations and signals map through nonlinear optical components. We now consider a crucial linear operation: a beamsplitter operation.

2.1.5 Beamsplitters

A general, lossless, beamsplitter couples light from two spatial modes, labelled a, b, into two orthogonal output modes, c, d. We may represented this operation by the following unitary matrix. Here η is the transmission across a to c and $1-\eta$ is the reflection from a into d[85]:

$$\begin{pmatrix} \sqrt{\eta} & i\sqrt{1-\eta} \\ i\sqrt{1-\eta} & \sqrt{\eta} \end{pmatrix} \begin{pmatrix} \hat{a} \\ \hat{b} \end{pmatrix} = \begin{pmatrix} \hat{c} \\ \hat{d} \end{pmatrix}. \tag{2.43}$$

The matrix in this equation is defined as $\hat{U}_{\mathrm{BS}}$ and is a unitary matrix. The form of this operation, with a phase upon reflection, stems from the requirement that the commutation relations for each mode are preserved. As the beamsplitter is lossless, photon number is also conserved with $\hat{n}_a + \hat{n}_b = \hat{n}_c + \hat{n}_d$.

A beamsplitter is a linear operation on the input modes and so we can treat the mapping of both the full quantum operators and fluctuations the same giving:

$$\mathrm{Var}(\hat{q}_c) = \eta \mathrm{Var}(\hat{q}_a) + (1-\eta)\mathrm{Var}(\hat{q}_b), \tag{2.44}$$

where q is any given quadrature operator. This equation has important consequences when one input mode has Piossonian statistics, even if the second input mode is the vacuum with zero mean energy. We can model loss, or inefficient detection, as a virtual beamsplitter transformation in which vacuum fluctuations are added and power is lost from the mode of interest. Figure 2.4 plots the amount of squeezing retained under varying levels of linear loss for 10 dB, 5 dB, and 2 dB input quadrature squeezing.

We can see from the above graph that high amounts of squeezing are less resilient to loss but that once squeezing is obtained, a small amount will endure loss and will be measurable provided the detection resolution and shot-noise clearance is sufficient.

2.2 Integrated optics

We now review integrated optics and the key operating principles behind components utilised in this thesis.

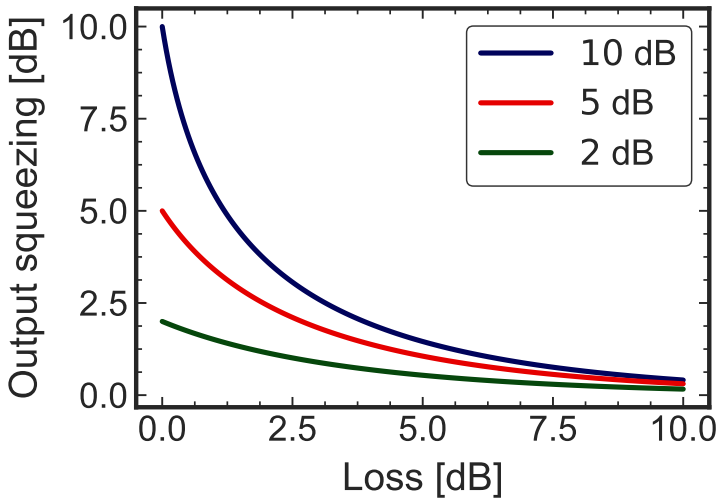

FIGURE 2.4. The effect of loss on quadrature squeeing for varying input amounts of squeezing.

2.2.1 Light in a dielectric

Considering an isotropic dielectric material, the total polarisation **P** induced from the electric dipoles created within the medium is well approximated by a term linear in the instantaneous applied field **E**[86]:

$$\mathbf{P} = \epsilon_0(\omega)\chi^{(1)}\mathbf{E}. \tag{2.45}$$

Here, ϵ_0 is the vacuum permittivity constant and $\chi^{(1)(\omega)}$ is the wavelength-dependent, first order susceptibility of the medium, given here by a complex scalar.

We can adapt Maxwell's equations for the flux densities induced by a propagating electromagnetic field through a polarised material[87]. Eliminating the magnetic field in favour of the electric field, we get a governing equation for the propagation of an electric field through a dielectric[86]:

$$\nabla^2\mathbf{E} - \frac{1}{c^2}\frac{\partial^2\mathbf{E}}{\partial t^2} = \mu_0\frac{\partial^2\mathbf{P}}{\partial t^2}, \tag{2.46}$$

We will make the assumption that the field is linearly polarised along the unit vector $\hat{\mathbf{x}}$ which does not change as the wave propagates along z.

We can insert Eq. 2.45 into Eq. 2.46 and define a new, adapted, permittivity $\epsilon(\omega) = (1 + \chi^{(1)}(\omega))$:

$$\nabla^2\mathbf{E} = \frac{\epsilon(\omega)}{c^2}\frac{\partial^2\mathbf{E}}{\partial t^2}, \tag{2.47}$$

where the index of refraction is now $\epsilon(\omega) \approx n(\omega)^2$. We can represent the electric field as a combination of a perpendicular mode distribution described by $F(x, y)$

and a fast varying propagation phase along z such that:

$$\mathbf{E}(\mathbf{r}, t) = \frac{\hat{\mathbf{x}}}{2}\Big(F(x, y)e^{i(\beta z - \omega t)} + \text{c.c.}\Big). \tag{2.48}$$

Inserting Eq. 2.48 into Eq. 2.47 gives the following eigenvalue problem in β:

$$\nabla^2 F(x, y) = \left(\beta^2 - \frac{\omega^2 n(\omega)^2}{c^2}\right)F(x, y), \tag{2.49}$$

which, along with appropriate boundary conditions in x and y, can be solved to give a wavelength-dependent propagation constant, β.

2.2.2 Waveguides

An optical waveguide is a structure that utilises two or more dielectric mediums to give a refractive index contrast in the plane perpendicular to the desired propagation direction to confine the light. The contrast in refractive index defines confined modes which can then guide light of specific wavelengths over long distances. A key example is an optical fiber which allows transatlantic low-loss transmission of signals[86]. In an optical fiber, and in most standard integrated optics waveguides, a core region of high refractive index, n_{core}, is surrounded by a low index cladding, n_{clad}, which is then extruded in the direction of travel. In a purely classical picture, a light wave traveling down the core will reflect of the interface multiple times in a process known as total-internal reflection. The number of modes supported at a given wavelength is defined by the geometry of the cross-section. The speed of propagation along the waveguide is governed by the effective mode index n_{eff}.

In general, Eq. 2.49 only has an analytically solution when a high level of symmetry is present in the confining cross-section, such as that provided by a slab. Fully confined solutions in 2D require numerical mode solver techniques, often requiring software such as Lumerical used in this thesis. We use such software to model the propagation constant, dispersion and effective modal area of supported modes of a waveguide, focusing our discussion to strip waveguides, depicted in Fig. 2.5.

These waveguides provide good confinement in the x and y plane and are therefore ideal for nonlinear optics. The height of the waveguide is mostly fixed by the manufacturer and is determined by the uniform growth of the silicon layer. The waveguide width can be tuned to change the dispersion properties of the waveguide. In this thesis, strip waveguides are used for integrated beamsplitters,

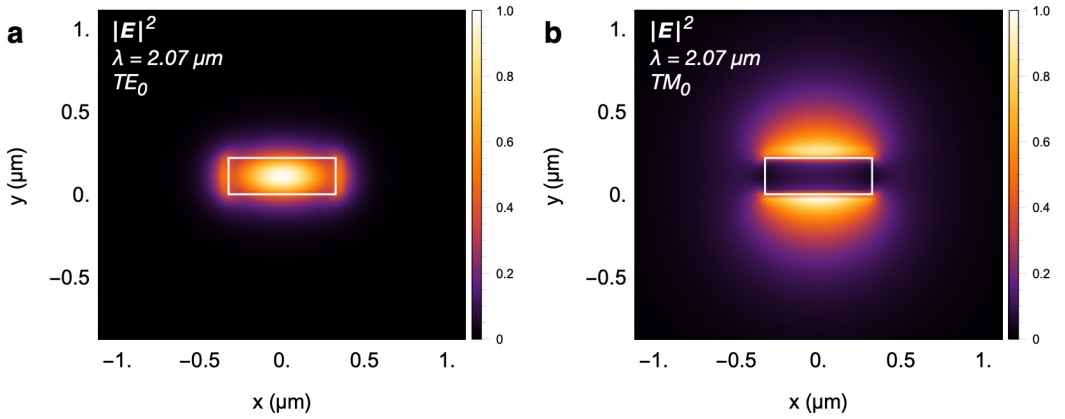

FIGURE 2.5. TE and TM mode electric field intensity in a strip waveguide. Figure taken with permission from Ref.[36].

nonlinear spirals and routing. The field intensity of a single-mode strip waveguide at 2.07 μm, showing both the fundamental transverse electric (TE) and transverse magnetic (TM) modes, is presented in Fig. 2.5. The TE mode is often the preferred mode of choice as it provides higher confinement inside the core and is more resilient to bend losses. The dominant loss mechanism of a TE waveguide arises from overlap of the optical mode with variations in the sidewalls (see Sec. 4.2 where we present a model for this). This loss mechanism has been shown to scale with λ^{-3} [88,89] suggesting a natural benefit from moving to longer wavelength light.

The modal area of a waveguide quantifies the size of the mode and is of great importance in nonlinear optics in which nonlinear effects scale with the intensity of the field inside the waveguide. There are a few definitions of modal area, for this thesis we use[90]:

$$A_{\text{eff}} = \frac{\left(\iint_{-\infty}^{\infty} |F(x,y)|^2 dxdy\right)^2}{\iint_{-\infty}^{\infty} |F(x,y)|^4 dxdy.} \tag{2.50}$$

The dispersion in a waveguide is due to the combination of a material and geometrical effects. A common approach is to Taylor expand the propagation constant about a central frequency ω_0 [86]:

$$\beta(\omega) = \beta_0 + \beta_1(\omega - \omega_0) + \frac{\beta_2}{2}(\omega - \omega_0)^2 + \frac{\beta_3}{6}(\omega - \omega_0)^3 + \ldots, \tag{2.51}$$

where

$$\beta_n = \left.\frac{d^n\beta}{d\omega^n}\right|_{\omega=\omega_0} \quad \text{for } n \in \mathbf{Z}^+. \tag{2.52}$$

$\beta_1 = 1/v_g$ relates to the central frequency group velocity at which the pulse centre propagates. β_2 is known as the group velocity dispersion (GVD), determining how fast a pulse contracts or spreads out. A positive GVD is often referred to as normal and a negative GVD is referred to as anomalous.

2.2.3 Fiber to chip coupling

To couple light into an integrated waveguide, we use a grating coupler. A grating couplers consists of a periodic structures that diffracts polarisation-dependent light incident from above the chip, at angle θ_i to the chip surface normal, into the waveguide, Fig. 2.6. The main design parameters of a grating are the etch depth, period, and fill factor (defined as the ratio of the tooth to grating periodicity). A grating is characterised via its insertion loss and 3-dB bandwidth. Coupled light must satify a phase-matching condition which occurs when the waves scattered off the grating have matching phases that constructively add together. Grating couplers have a typical bandwidth of order ~ 100 nm, limited by degraded phase-matching across wider spectrums. A key benefit to grating couplers, however, is there long term stability and ease of alignment of multiple channels via a V-groove array (VGA). When phase-matched, we can obtain an expression for the grating period via solving for the first diffraction order[89]:

$$\Lambda = \frac{\lambda}{n_{\text{eff}} - n_{\text{clad}} \sin\theta_i}. \tag{2.53}$$

where n_{eff} is defined as the weighted effective index for the tooth and trench slab modes and n_{clad} is the index of the cladding.

2.2.4 Directional couplers

Directional couplers provide a method of coupling light between separate waveguides. When two waveguide are routed close to one another, light from one tunnels through to the other via the evanescent field located outside the core of the waveguide. The superpositions of the individual waveguide modes are coined supermodes. Two orthogonal supermodes, known as the symmetric and anti-symmetric supermodes, are excited, each with different effective indices. The difference between the indices of these supermodes, $\Delta n = |n_{\text{odd}} - n_{\text{even}}|$, leads to a beating effect in which the power oscillates between the two waveguides[89]. Via tuning of the length of the coupling region, we can split the power 50/50 across the two waveguides as depicted via an FDTD simulation of a direction coupler

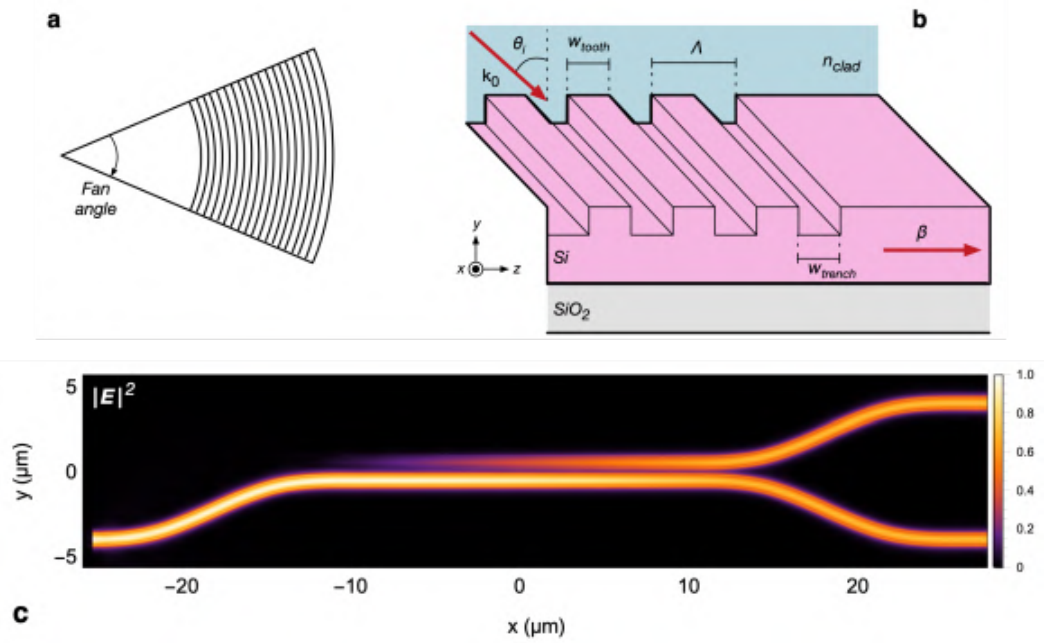

FIGURE 2.6. (a) top down schematic of a grating coupler and (b) in plane schematic of a grating coupler used to couple light into a chip. (c) normalised electric field intensity of a full 3D FDTD simmulation of a balanced directional coupler tuned to 50/50. Figure taken with permission from Ref.[36].

shown in Fig. 2.6(c). At wavelength λ, the 50/50 transfer length is given by:

$$L_{50} = \frac{\lambda}{4\Delta n} \tag{2.54}$$

The unitary matrix that represents the action of a directional coupler on two input mode fields is given by[36]:

$$\hat{U}_{\mathrm{DC}} = \begin{pmatrix} \cos\left(\frac{\pi z}{4L_{50}}\right) & i\sin\left(\frac{\pi z}{4L_{50}}\right) \\ i\sin\left(\frac{\pi z}{4L_{50}}\right) & \cos\left(\frac{\pi z}{4L_{50}}\right) \end{pmatrix}. \tag{2.55}$$

2.2.5 Thermo-optic phase shifters

We can change the phase of light traveling through a silicon waveguide via the thermo-optic effect. Heat from a current-carrying metal element on top of the waveguide alters the refractive index. The thermo-optic coefficient of silicon determines the expected change in index per Kelvin:

$$\Delta\phi = \frac{2\pi L}{\lambda}\frac{\partial n}{\partial T}\Delta T. \tag{2.56}$$

Here, L is the optical path length inside the waveguide and Δn is the induced change in the refractive index. In silicon in the 2.1 µm–band, the thermo-optic coefficient is approximately $\partial n/\partial T = 1.7\text{x}10^{-4}$ K^{-1} [36,91]. The temperature change scales with electrical power through the resistive element atop the waveguide. As such, the phase scales with the square of the applied voltage. Though limited in speed and susceptible to thermo and electrical cross talk between multiple heater channels, thermo-optic phase shifters are sufficient for low-component applications which only require static phase adjustments.

2.2.6 Integrated beamsplitters

We can utilise two 50/50 directional couplers and a phase shifter to build a Mach-Zehnder interferometer (MZI), capable of achieving $\hat{U}_{\text{BS}}$ for any value of η. Figure 2.7 shows a schematic of the interferometer. Using Eq. 2.55 with $z = L_{50}$, we can solve for the composite transfer function of the interferometer, found to be:

$$\hat{U}_{\text{MZI}} = \frac{1}{2}\begin{pmatrix} e^{i\phi}-1 & i(e^{i\phi}+1) \\ i(e^{i\phi}+1) & e^{i\phi}-1 \end{pmatrix}, \tag{2.57}$$

where ϕ is the phase imparted by the heater, as per Eq. 2.56.

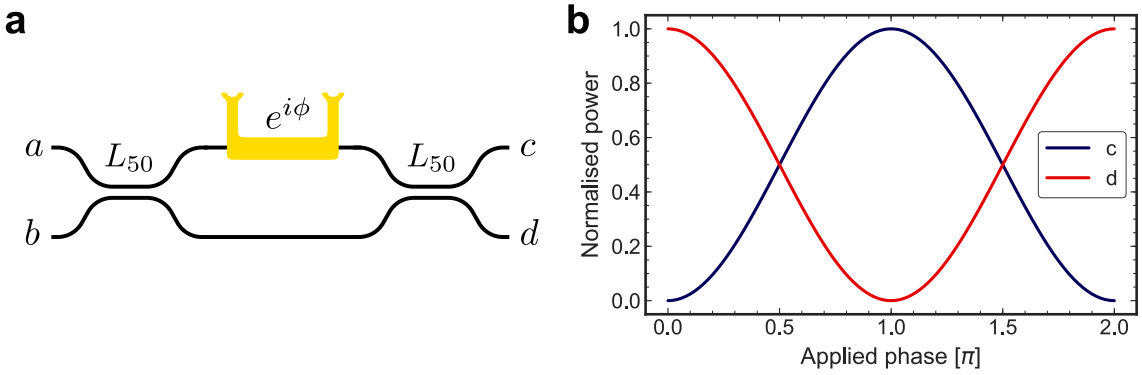

FIGURE 2.7. (a) schematic of an MZI beamsplitter, mapping input modes a, b to output modes c, d. (b) the normalised output mode power with applied phase given input into mode a.

Chapter 3

Shot-noise Limited Homodyne Detection in the 2 µm–band

Declaration of contribution: *the detector design was adapted for 2 µm operation from a design made by Joel Tasker, University of Bristol. All simulations, component selection, and device assembly were carried out by myself, along with full detector characterisation and measurement of vacuum noise. The research paper on which this chapter is based was also written by myself, with feedback and advice given by the additional authors.*

In this chapter we present the design, characterisation and employment of a novel homodyne detector capable of megahertz-speed shot-noise limited quantum light characterisation in the 2 µm–band. Sections 3.1 & 3.2 present key homodyne theory and relevant electrical design considerations. Section 3.5 then presents the characterisation of the device which closely follows work I have published in Ref.[92], with some text quoted verbatim and figures adapted from the publication.

Invented by Yuen and Chan in 1983[93], homodyne detection is a powerful tool in both classical and quantum optics for the measurement of field quadratures. In homodyne detection, the target field is mixed with a brighter optical field of the same wavelength, known as a local oscillator (LO), via a 50:50 beamsplitter; the two resulting fields are detected via high-efficiency photodiodes. The photocur-

rents are then subtracted and amplified into a voltage via a current-to-voltage converter. The output RF signal is proportional to the target field's quadrature with the quadrature phase determined directly by the LO phase.

In classical optics, this method is often used to provide a reference signal for lock-in amplification[94] or to suppress unwanted quadrature noise in sensing measurements by isolating the target quadrature[95]. In quantum optics, homodyne detection offers a unique method for the direct measurement of quadrature noise within a state and can be used for full continuous-variable quantum state tomography[51]. Although homodyne detection offers direct measurement of a quantum phenomena at room temperature with standard laboratory signal analysis equipment, the method is not without its complexities. The main complexity arises from the fact that the DC currents generated in each photodiode are orders of magnitude greater than the subtraction signal. Therefore the detector circuit must feature a high common-mode rejection ratio (CMRR). In addition, the quantum noise level measured, although naturally amplified by the technique, remains comparable to electronic $1/f$ noise and so requires extremely low-noise voltage supplies and amplification to ensure the measurement is shot-noise limited.

Off-the-shelf homodyne detectors have so far been limited to the visible and telecoms bands for two main reasons: 1) they naturally required high-efficiency photodiodes which historically have only been available in these bands and 2) key optical infrastructure such as low-noise lasers and passive components have been lacking outside these regions. As a result, the investigation of quantum light through homodyne detection has been extensively pursued in the near-infrared and has enabled many flagship experiments across quantum computing[96], quantum entanglement[97], quantum communications[98], and quantum state measurement[99,100]. Other key quantum use cases for homodyne detectors include: quantum random number generation[101], comb-based absorption spectroscopy[102], and quantum teleportation[103].

In recent years, the demand for homodyne detection in the mid-infrared (MIR) spectral region has increased. This increase has largely been driven by MIR quantum state preparation for novel sensing applications[65,104,105] and free space communications[106]. The atmosphere's MIR transparency window, with much reduced Rayleigh scattering cross sections compared to the telecoms band, makes 2 µm a good candidate for free space communications[106]. In sensing, the availability of continuous-variable quantum MIR sources has set the scene for compelling quantum sensing applications in the fingerprint region with source

characterisation often requiring homodyne detection. 2 µm has also been identified as a beneficial wavelength for avoiding nonlinear loss present at 1550 nm in silicon quantum photonics.[65]

A similar technique to homodyne detection is balanced detection which has already been investigated in the MIR for a number of classical applications including frequency-modulation spectroscopy[69], difference-frequency laser spectroscopy[70], balanced radiometric detection[71], and Doppler-free spectroscopy[107]. To perform shot-noise limited homodyne detection, required for quantum state measurement, greater electrical noise suppression is needed in comparison to balanced detection, making it harder to engineer for. By developing a detector that affords a high signal-to-noise ratio, we also help facilitate higher sensitivity in classical schemes that employ balanced detection to monitor amplitude modulation signals[108], reject classical laser noise[109] or map information from optical frequencies to the RF via coherent heterodyne beating of optical frequency combs[110].

Mansell *et al.* and Yap *et al.* have both previously employ extended InGaAs photodiodes in a homodyne configuration to measure squeezing at 1984 nm in the audio band, however, these demonstrations require a pre-amplification scheme for each photodetector and a post-processed photocurrent subtraction[104,105]. The bandwidth of both experiments is restricted to ≤ 500 kHz by the need for high gain amplification required to provide shot-noise clearance above excessive electrical noise. Using the same post-processing configuration, Gabbrielli *et al.*[111] recently demonstrated shot-noise limited homodyne detection in the MIR (around 4.5 µm) enabling the first characterisation of quantum noise with a quantum cascade laser source. Gabbrielli *et al.* were able to overcome the low conversion efficiency of state-of-the-art 4.5 µm HgCdTe detectors to measure shot-noise with a total efficiency of 38% and maximum clearance of 7 dB.

Here, we move beyond the audio band and employ extended InGaAs PIN photodiodes integrated into a single device capable of megahertz-speed shot-noise limited homodyne detection in the 2 µm–band with 57% efficiency. This is already sufficient to use with squeezed light generation to construct optical sensors with sensitivity[112] and precision[50] beyond the classical limit. This efficiency is also greater than the 50% threshold required to measure negative-valued Wigner functions, which is a clear signature of non-classical behavior for non-Gaussian quantum states[113]. We test this detector by using it to perform a homodyne measurement of vacuum quadrature noise via a 2.07 µm pulsed mode-locked fibre laser, proving the device capable of quantum noise measure-

ment. We characterise the efficiency, bandwidth, shot-noise clearance (SNC), and CMRR; these are each important considerations for using the detector to perform future squeezed light detection at 2.07 µm. In the following chapter, we will employ this detector to measure how classical noise is affected in a nonlinear silicon interferometer.

3.1 Homodyne theory

In this first section, we outline the key theory behind homodyne detection. Following the nomenclature of Ref.[80] and inline with chapter 2, we represent the signal and LO fields via time-dependent continuum quantum operators $\hat{A}_s(t)$ and $\hat{A}_{\mathrm{LO}}(t)$. The word *homodyne* means pertaining to two waves which radiate from a single radiation source and thus both fields are phase stable and have the same wavelength. Figure 3.1 below shows a typical schematic for homodyne detection. We interfere both fields on a 50:50 beamsplitter and then detect the mixed fields with photodiodes. We have control of the LO phase, ϕ, via a phase shifter in the LO arm.

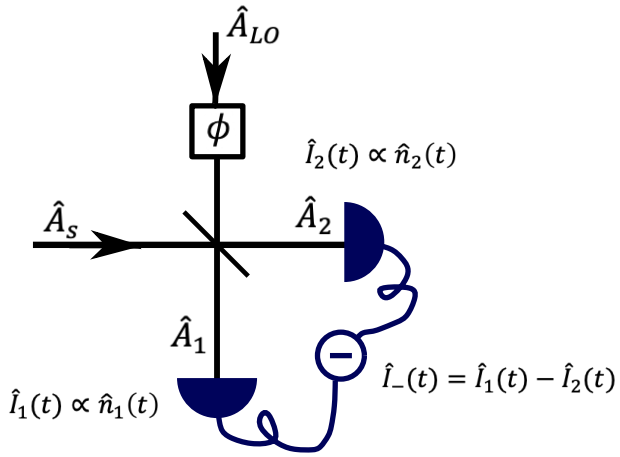

FIGURE 3.1. A schematic of homodyne detection. The signal field and LO field are mixed on a 50:50 beamsplitter. The mixed field amplitudes are then detected via photodiodes. The resulting currents are subtracted.

Following theory laid out in Section 2.1.4, we split the two fields via linearisation into their classical, static, mean expectation value $\alpha_s, \alpha_{LO} \in \mathbb{C}$, plus some small, fast varying, quantum noise $\hat{a}(t)$:

$$\begin{aligned}\hat{A}_s(t) &= \alpha_s \hat{I} + \delta\hat{a}_s(t),\\ \hat{A}_{\mathrm{LO}}(t) &= (\alpha_{\mathrm{LO}}\hat{I} + \delta\hat{a}_{\mathrm{LO}}(t))e^{i\phi}.\end{aligned} \tag{3.1}$$

Where $\hat{I}$ is the identity operator. We now make the following approximations:

1. The LO is brighter than the signal such that $|\alpha_{\mathrm{LO}}|^2 \gg |\alpha_s|^2$ and $|\alpha_{\mathrm{LO}}|^2 \gg |\hat{a}_s(t)|^2$.
2. All higher order terms in quantum fluctuations, i.e. $O(\delta^n)$ where $n \geq 2$, are negligible.
3. Without loss of generality we can expand $\alpha_{\mathrm{LO}} = |\alpha_{\mathrm{LO}}|e^{i\phi_{\mathrm{LO}}}$ and assume $\phi_{\mathrm{LO}} = 0$.

Under these assumptions we can represent the two fields as:

$$\begin{aligned}\hat{A}_s(t) &= \hat{a}_s(t),\\ \hat{A}_{\mathrm{LO}}(t) &= \hat{I}|\alpha_{\mathrm{LO}}|e^{i\phi}.\end{aligned} \tag{3.2}$$

By applying the beamsplitter relations[81] (Sec.2.2.6) we get:

$$\begin{aligned}\hat{A}_1(t) &= \frac{1}{\sqrt{2}}(|\alpha_{\mathrm{LO}}|e^{i\phi} + \hat{a}_s(t)),\\ \hat{A}_2(t) &= \frac{1}{\sqrt{2}}(|\alpha_{\mathrm{LO}}|e^{i\phi} - \hat{a}_s(t)).\end{aligned} \tag{3.3}$$

The instantaneous photocurrent generated by each photodiode is given by:

$$\hat{I}(t) = \eta_{\mathrm{c}}\mathscr{R}\hat{A}^{\dagger}(t)\hat{A}(t), \tag{3.4}$$

where η_{c} is the coupling efficiency and $\mathscr{R}$ is the photodiode responsivity. The photocurrent from each diode is therefore equal to:

$$\begin{aligned}\hat{I}_1(t) &= \frac{\eta_{\mathrm{c}}\mathscr{R}}{2}\left[|\alpha_{\mathrm{LO}}|^2 + |\alpha_{\mathrm{LO}}|[\hat{a}_s(t)e^{i\phi} + \hat{a}_s^{\dagger}(t)e^{-i\phi}]\right],\\ \hat{I}_2(t) &= \frac{\eta_{\mathrm{c}}\mathscr{R}}{2}\left[|\alpha_{\mathrm{LO}}|^2 - |\alpha_{\mathrm{LO}}|[\hat{a}_s(t)e^{i\phi} + \hat{a}_s^{\dagger}(t)e^{-i\phi}]\right].\end{aligned} \tag{3.5}$$

Taking the subtraction of the photocurrents removes the larger, slow varying, DC components from the LO mean power:

$$\begin{aligned}\hat{I}_-(t) &= \hat{I}_1(t) - \hat{I}_2(t)\\ &= \eta_{\mathrm{c}}\mathscr{R}|\alpha_{\mathrm{LO}}|[\hat{a}_s(t)e^{i\phi} + \hat{a}_s^{\dagger}(t)e^{-i\phi}]\\ &= \eta_{\mathrm{c}}\mathscr{R}|\alpha_{\mathrm{LO}}|\hat{q}_{s,\phi}(t),\end{aligned} \tag{3.6}$$

where $\hat{q}_{s,\phi}(t)$ is the instantaneous quadrature operator of the signal mode defined by phase ϕ of the LO field.

Equation 3.6 holds under the assumptions that the total efficiency is equal for both photodiodes and that the 50:50 homodyne beamsplitter is ideal. In reality, each photodiode will have a slightly different responsivity and coupling coefficient, and the beamsplitter will not be perfectly 50:50. These imperfections only degrade the efficiency of the quadrature measurement and can be minimised by fine-tuning the coupling of each photodiode to ensure the detector remains balanced. For a full analysis of the imperfect case, we direct the reader to Refs. [114,115].

In reality, the detector will also have some finite response time. There will also be some unwanted electrical noise. We can approximate for these effects by adapting Eq.3.6 to:

$$\hat{I}_{-}(t) = \eta_{\mathrm{c}}\mathscr{R}\int_{-\infty}^{\infty} r(t-t')|\alpha_{\mathrm{LO}}|\hat{q}_{s,\phi}(t')dt' + \hat{I}_{\mathrm{d}}(t) \tag{3.7}$$

Here, $r(t)$ is the detectors unit response function and $\hat{I}_{\mathrm{d}}(t)$ is the detector dark current produced by local defects and minority carriers. In the ideal detector with infinite bandwidth, $r(t) = \delta(t)$. We now apply this equation to two relevant scenarios, continuous-wave illumination, and pulsed illumination.

3.1.0.1 Homodyne with a continuous-wave laser

Let us consider the case where the LO is constant i.e. a continuous-wave (CW) laser source well described by the coherent state $|\alpha_{\mathrm{LO}}\rangle$, and we are interested in measuring the signal quadrature defined by some desired temporal mode $\hat{Q}_{\mathrm{targ}} = \int_{-\infty}^{\infty}\Phi(t)\hat{q}_{s,\phi}(t)dt$ where $\Phi(t)$ is our desired temporal mode. Due to the finite response of the detector, each measurement of photocurrent will consist of a weighted sum of instantaneous quadratures integrated over a temporal mode defined by the response function $r(t)$. Let us define this measured quadrature to be:

$$\hat{Q} \equiv \int\int_{-\infty}^{\infty} r(t-t')\hat{q}_{s,\phi}(t')dt'dt. \tag{3.8}$$

$\hat{Q}_d \equiv \int_{-\infty}^{\infty}\hat{I}_{\mathrm{d}}(t)dt$ corresponding to the electrical noise contribution. Equation 3.7 then becomes:

$$\hat{I}_{-} = \eta_{\mathrm{c}}\mathscr{R}|\alpha_{\mathrm{LO}}|\hat{Q} + \hat{Q}_d \tag{3.9}$$

Reference[114] proves that in the common case that the desired signal temporal mode bandwidth is known, and the detector bandwidth is comparable to or greater than the desired measurement bandwidth, the effect of the detector response on the measurement is negligible with $\hat{Q} \approx \hat{Q}_{\mathrm{targ}}$.

3.1.0.2 Homodyne with a pulse laser

We now consider the case where the LO consists of a train of pulses with repetition rate R_r and pulse width much shorter than the time resolution of the electronics. Under this assumption, we can assume the response of the detector to a single pulse centred at $t = 0$ to be given by just the response function:

$$\hat{I}_-(t) = \eta_c \mathscr{R} r(t) \alpha_{LO} \hat{Q}_p + \hat{I}_d(t). \tag{3.10}$$

We define $\hat{Q}_p$ to be the normalised quadrature operator corresponding to the temporal mode defined by the shape of the single LO pulse, given by:

$$\hat{Q}_p = \alpha_{LO}^{-1} \int_{-\infty}^{\infty} \alpha_{LO}(t) \hat{q}_{s,\phi}(t) dt \tag{3.11}$$

where $\alpha_{LO} = \sqrt{\int_{-\infty}^{\infty} |\alpha_{LO}(t)|^2 dt}$ is a normalisation coefficient[114]. For a pulse train, we must consider the case where the detector bandwidth is less than R_r. In this case, the output photocurrent is in fact the sum of detector responses to several pulses. Each pulse will run into the previous pulse, consequently polluting the measurement of the desired pulse quadrature with previous pulse quadratures. We can represent this as a sum over the surrounding j pulses to the pulse of interest with index $j = 0$. At time t, the current is given by:

$$\hat{I}(t)_- = \eta_c \mathscr{R} \alpha_{LO} \sum_{j=-\infty}^{\infty} \hat{Q}_{p,j} r(t - j/R_r) + \hat{I}_d(t) \tag{3.12}$$

The addition of this ringing effect degrades the efficiency with which $\hat{Q}_{p,0}$ is measured. Reference[114] finds that in the case of a Gaussian response function, the degradation in efficiency is non-negligible for detector bandwidths $< 0.4R_r$. i.e. when $j \neq 0$ terms become comparable to the $j = 0$ term.

To test the homodyne detector's efficacy of quantum noise measurement, we will perform homodyne detection on the vacuum state ($|\alpha\rangle_s = |0\rangle$) with a pulsed laser. Since measurements of vacuum quadrature are inherently phase invariant, we will omit phase dependence from this point onwards.

3.1.1 Electronic readout

In the previous section we determined that the output current from the homodyne configuration is proportional to the target field's quadrature, with the quadrature-phase determined directly by the phase of the LO . We now discuss how that current is amplified into a voltage and analysed. Since flat, low noise,

amplification electronics are crucial for the accurate and efficient assessment of quantum noise in the target light field, we employ a transimpedance amplifier (TIA) to amplify the subtracted current into an output voltage[116]. Section 3.2.2 gives an in-depth discussion of TIA. Employing TIA, over passive conversion through an RC-circuit, helps enable a greater measurement bandwidth with favorable noise statistics[117].

The TIA amplifies the output subtraction photocurrent into a voltage given by:

$$\begin{aligned}\hat{V}(t) &= R_f \hat{I}_-(t) \\ &= R_f \left[\eta_c \mathscr{R} \alpha_{\mathrm{LO}} \sum_{j=-\infty}^{\infty} \hat{Q}_{\mathrm{p,j}} r(t - j/R_r) + \hat{I}_{\mathrm{d}}(t) \right]\end{aligned} \tag{3.13}$$

where R_f is the TIA's feedback gain resistor. Note that $\hat{I}_{\mathrm{d}}(t)$ is now a combination of several noise sources that we will outline in Section 3.2.3.

3.1.1.1 Electronic spectrum analysers

To analyse the spectrum of quadrature noise, we use an electronic spectrum analyser (ESA) that measures the power spectral density (PSD) of the amplified voltage signal. The ESA we employ makes used of the heterodyne principle, depicted in Fig .3.2[118]. In short, the input voltage signal is mixed with an internal LO, amplified, and then filtered by a fixed internal frequency filter. The 3-dB bandwidth of this filter is known as the resolution bandwidth (RBW) of the measurement. The filter position is fixed, with frequency selection performed by sweeping the LO. For each LO frequency, the filter output is logarithmically amplified and detected via an envelope detector which outputs a voltage corresponding to the amplitude of the selected frequency component. A low-pass video filter is then used to remove noise from the detector output, the bandwidth of which is known as the video bandwidth (VBW). For VBW<RBW, this filter effectively reduces the noise in the output spectrum. Analog-to-digital converters are then used to convert the signal for display or further processing and analysis. For an in-depth discussion on ESAs, we point the reader towards Ref.[119,120].

The PSD about frequency Ω is well approximated by[50]:

$$\langle \hat{p}_\Omega \rangle = \frac{2}{R_{\mathrm{imp}}} \left\langle \int_{\Omega - B/2}^{\Omega + B/2} |\tilde{\hat{V}}(\omega)|^2 d\omega \right\rangle \tag{3.14}$$

where ω is the radio frequency, R_{imp} is the analyser's input impedance and B is the RBW. Here, $\tilde{\bullet}$ denotes the Fourier transform.

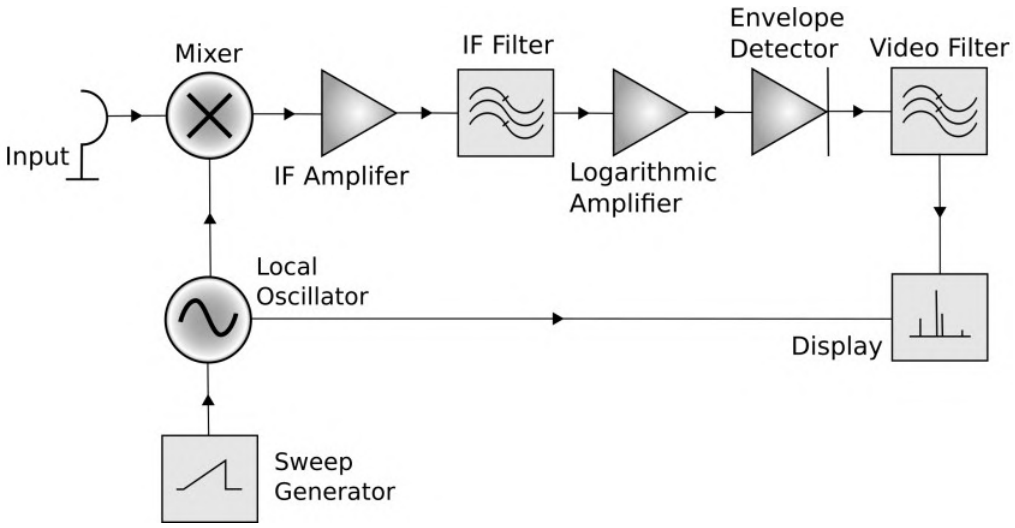

FIGURE 3.2. A schematic of an electonic spectrum analyser operating on the hetrodyne principle. Figure taken with permission from Ref.[118].

When analysing the spectrum of optical noise for comparison to signal levels in a signal-to-noise measurement, there are a few extra considerations to be aware of regarding how the ESA processes the input signal. The first results from the fact that the low-pass video filter is effectively averaging over the envelope detector output which itself is proportional to the square of a logarithmically amplified signal. Averaging of the logged power signal is fundamentally different to logging the average power and produces a different result[120]. For signals with Gaussian distributed noise, these measurements are the same[118,120], however, for broadband noise measurements, which follow a Rayleigh distribution, this effect results in an under-response of 2.51 dB. We must therefore correct for this power when measuring an absolute value of broadband noise sources such as optical shot-noise. The voltage of CW signals is typically Gaussian distributed, and therefore this correction factor does not apply[118].

A second important consideration is that the resolution filter has a Gaussian shape, instead of a square shape, to improve the transient response and speed up the measurement. In Eq. 3.14, a square shaped RBW, B, is assumed. We can correct for this assumption in the case of broadband noise by calculating the equivalent square bandwidth that would measure the same $\langle p_\Omega \rangle$ as a Gaussian filter. The required correction factor is calculated by Ref.[120] to be 0.24 dB which must be subtracted from the measured noise power.

We take the Fourier transform of the voltage to give:

$$\tilde{\hat{V}}(\omega) = R_f \eta_c \mathscr{R} \alpha_{\mathrm{LO}} \sum_{j=-\infty}^{\infty} \hat{Q}_{\mathrm{p,j}} e^{\frac{-2\pi i \omega j}{R_r}} r(\omega) + R_f \tilde{\hat{I}}_{\mathrm{d}}(\omega) \tag{3.15}$$

In the case of a pulsed vacuum measurement, we can insert Eq. 3.15 into Eq. 3.14 and take the expectation with respect to the quantum ensemble of the signal vacuum state. Doing so gives:

$$\langle \hat{p}_\Omega \rangle = \frac{2R_f^2}{R_{\mathrm{imp}}} \left[\frac{hc}{\lambda} \eta_c^2 \mathscr{R}^2 \alpha_{\mathrm{LO}}^2 \int_{-\Omega-B/2}^{\Omega+B/2} |\tilde{r}(\omega)^2| d\omega + |\tilde{I}_\Omega| \right] \tag{3.16}$$

A factor of photon energy, hc/λ, results from the conversion of natural to standard units. Here, $|\tilde{I}_\Omega|$ is the electronic-noise contribution integrated across the resolution bandwidth. In this calculation, we have made use of the fact that $\langle \hat{Q}_k \hat{Q}_j^\dagger \rangle_{\mathrm{vac}} = \delta(k-j)$.

Within the bandwidth of the detector, we assume the Fourier transform of the unit impulse response function flat such that $\int_{\Omega-B/2}^{\Omega+B/2} |\tilde{\hat{r}}(\omega)|^2 d\omega \approx B$. By analysing how the output voltage scales with LO power, α_{LO}^2, we asses the detectors ability to measure quadrature noise. If the detector fully rejects classical noise, the PSD will scale linearly with LO power as per Eq. 3.16, if not then we expect the PSD to scale with the square of the power. We use this linear dependence to infer whether the detectors are shot-noise limited in their measurement of the vacuum and are thus suitable for sub-shot-noise quantum state measurement.

3.2 Key components and considerations

We now move on to discuss the key components required to build a Homodyne detector, and the relevant consideration of each for utility in the 2 µm–band.

3.2.1 The photodiode

A photodiode is defined as a semiconductor PN junction which has the ability to convert photons to electrons. Here, 'P' and 'N' refer to positive or negative doped semi-conductor materials, typically from periodic groups III and V. At the boundary where the two materials meet, carriers recombine to leave behind charged ions which result in an intrinsic potential field, known as the depletion region. When a photon of sufficient energy strikes the junction, an electron-hole pair is created via the photoelectric effect which is then extracted via a reverse bias potential (under photo-conductive operation)[116]. The resultant current is

proportional to the square of the amplitude of the field or equivalently the number of incident photons[121]. With no photons incident on the junction, local impurities in the depletion region which require less energy to be excited into the valency band can still generate electron-hole pairs through thermal excitation[122]. This dark current is extracted at zero bias by the intrinsic potential in the depletion region and grows in magnitude with increasing reverse bias. The wavelength range over which a particular diode has a good responsivity is determined by the choice of III-V material and absorption region depth. Crucially, a photon must have enough energy to excite an electron into the valency band within the depletion region.

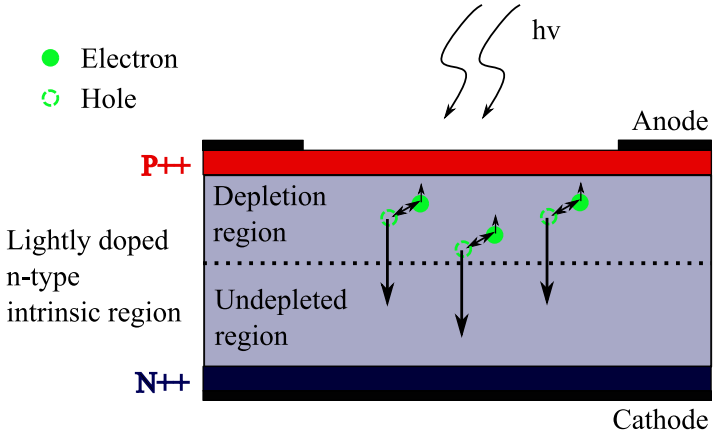

FIGURE 3.3. A schematic of a vertically stacked PIN photodiode with a heavily N-doped region (dark blue), lightly n-doped region (pale blue) and a P-doped region (red). Photons enter the top window and are absorbed across the intrinsic region, creating electron hole pairs. These charge carriers are then extracted towards the Anode and Cathode via a reverse bias potential. The resulting current is proportional to the number of photons entering the photodiode.

Figure 3.3 displays a typical configuration of a vertical PIN photodiode. Here, the 'I' stands for intrinsic region and is lightly N-doped in this example and typically highly resistive. The intrinsic region is added to some photodiodes as it brings a number of benefits. Firstly, the wider absorption region (typically of depth $1/\alpha$ where α is the absorption coefficient of the material) allows for the collection of more light thereby increasing the efficiency. Secondly, the diode becomes responsive over a larger wavelength range as photons release carriers over a range of depths proportional to photon wavelength. Thirdly, the high resistivity of the intrinsic region leads to a much larger depletion region. The has an effect on the speed of the photodiode in response to a pulse of photons by reducing the

capacitance across the diode. Conversely, a greater reverse bias voltage is usually required in PIN diodes as carriers have further to travel which can also increase the amount of dark current extracted, negatively effecting the signal-to-noise ratio.

The photocurrent of interest, I, can be directly calculated for a given incident wavelength via the photodiode responsivity $\mathscr{R}(\lambda)$ [A/W] [121]:

$$\begin{aligned} I(\lambda) &= \mathscr{R}(\lambda)\eta_c P_{\text{in}} \\ &= \frac{\eta_{QE}\lambda e}{hc}\eta_c P_{\text{in}} \end{aligned} \tag{3.17}$$

Here, η_{QE} is the quantum efficiency of the diode, a direct measure of the percentage of incident photons that are converted to electrons and extracted from the junction, P_{in} is the incident optical power, and η_c is the coupling efficiency. e is the electron charge, c is the speed of light and h is Planck's constant.

We can model the electronics of a photodiode with a discrete circuit model consisting of an input current, dark current, and parasitic elements as seen in Fig. 3.4. In the ideal photodiode model, the shunt resistance represents the resistance felt by the dark current at zero bias voltage. This effective resistance has an associated thermal-dependent noise that is well modelled by the Johnson noise of an actual resistor (see Sec.3.2.3) [121]. A high shunt resistance is desireable to reduce photodiode Johnson noise. The series resistance models the semiconductor material and pad resistance and is generally of order tens of ohms. The junction capacitance models the stored charge effect of the photodiode's depletion region which is well modelled by two parallel plates separated by the depletion region. The capacitance is proportional to the active area of the photodiode and inversely proportional to depletion width [121]. In response to AC signals, the junction capacitance and shunt resistance give a combined impedance magnitude of $|Z| = \left(R_{\text{shunt}}^{-2} + (2\pi f C_{\text{pd}})^2\right)^{-1/2}$, where f is the AC frequency. Close to DC, a small shunt resistance will result in greater bias voltage noise coupling into the photodiode current. Conversely, at higher frequencies, junction capacitance will determine the strength of this additional noise source with smaller capacitance presenting greater impedance. As we will see Section 3.2.2, junction capacitance also contributes to the overall parasitic capacitance on the input of the homodyne detector which will have an effect on not just the noise properties, but also the stability and bandwidth of the detector.

Industry has delivered several photodiode options for the 2 µm–band with applications geared towards classical absorption sensing of gasses active at this

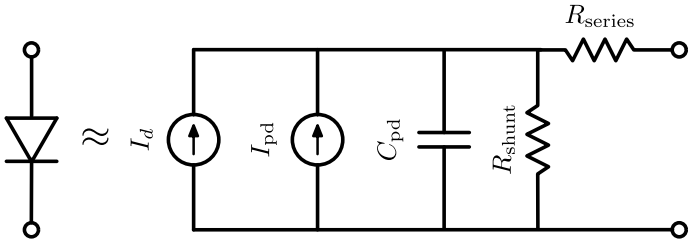

FIGURE 3.4. An equivalent photodiode model for a photodiode in reverse biad. The photodiode is represented as a dark current source (I_d), light current source (I_{pd}), parallel capacitor, parallel resistor, and a series resistor. This equivalent model is used to simulate the response of a photodiode under illumination.

wavelength e.g. CO_2, Fig. 1.1. These range from the first- developd GaInAsSb on GaAs substrate architectures to the most popular current solution of extended InGaAs on an InP substrate[123,124]. An InP substrate is chosen for its high reflectivity in this band resulting in a higher collection efficiency as light is reflected back into the intrinsic region. Here, we employ vertically-illuminated extended InGaAs PIN photodidoes which have been made responsive up to 2.6 µm by increasing the indium content and absorption region depth[122]. These differences, required to gain a response at longer wavelengths, results in very different electrical properties when compared to commonly used InGaAs PIN photodiodes for 1550 nm. For the sake of comparison, we compare Laser Components 1550 nm InGaAs photodiode (IG7X250S4i), labelled PD15, with their extended InGaAs photodiode (IG26X250S4i) for operation up to 2.6 µm, labelled PD26, both of which have the same active area. Firstly, additional strain applied in fabrication to extend the diode leads to a greater number of defects and results in a decrease in shunt resistance and an increased dark current. At 0.25 V bias, PD15 has a dark current of 45 pA compared to PD26 with 2 µA – a near 50000 increase. The shunt resistance in PD26 at 10 mV bias is 60 kΩ compared to PD15 with 830 MΩ. At 0 V bias, the junction capacitance of PD15 is 15 pF compared to PD26 with 35 pF. At 1 V bias, the capacitance of both diodes are near equal with PD26 at 8 pF and PD15 at 9 pF. Although this suggests the limiting factor at 0 V bias was the intrinsic potential, we cannot infer the cause of this difference for these particular diodes without more information.

The transit time limited rise time of PD26 at 0 V bias in response to a square pulse is approximately 230 ns compared to PD15 which shows a rise time 80 ns. As such, the 3-dB bandwidth of the extended photodiode into a simple 50 Ω load resistor is limited to 1.5 MHz. At 0 V bias, the depletion region is smallest and

light will be absorbed in both the depletion region and charge neutral zone. For extended diodes, the transit time is most likely limited by the diffusion of minority carriers in the charge neutral zone[125]. To gain a response from PD26 at higher speeds, a reverse bias potential is required at the cost of greater dark current. Additionally, all extended InGaAs photodiodes for 2 µm operation are free space coupled as opposed to fiber coupled. This will result in additional coupling losses from Fresnel reflections off the glass housing which ultimately limit the coupling efficiency[126].

3.2.2 Transimpedance amplification

We now cover TIA as a preferred method of photocurrent readout. Transimpedance is defined as the ratio of the output voltage to the input current of a current-to-voltage converter. We will consider TIA as a DC circuit first to understand how amplification arises. We then discuss the AC case in which we consider the bandwidth and stability.

3.2.2.1 DC analysis

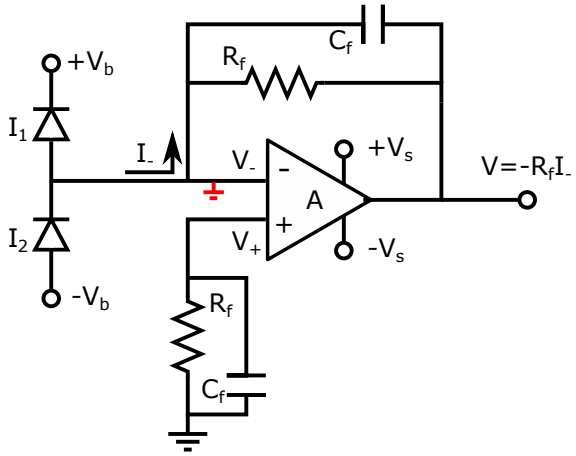

FIGURE 3.5. A DC electrical circuit diagram for TIA amplification of a photosubtraction signal.

The diagram above shows a TIA circuit employed to amplify the subtracted photocurrent. TIA employs an operational amplifier (op-amp) in a inverting feedback configuration[117,127]. An op-amp can be considered to be a high gain DC voltage amplifier[128]. It has two inputs labelled inverting $(-)$ and non-inverting $(+)$. Given the input voltages V_+ and V_-, the op-amp will output a voltage given

by:

$$V = A(V_+ - V_-) \tag{3.18}$$

where A is the open-circuit gain of the op-amp, considered to be large ($\sim 10^6$). We note that the range of output voltages is limited by the supply rails of the op-amp such that $V \in \{-V_s, +V_s\}$.

In a TIA configuration, the central net of the two photodiodes which carries the photocurrent subtraction is tied to the op-amp's inverting input. The non-inverting input is tied to ground such that we can consider $V_+ = 0$. The input nodes of an op-amp see a high impedance which shunts the photocurrent up through the resistor R_f. Using first principles to solve for the voltage drop across a resistor, we can find V_- to be given by $V_- = V + R_f I_-$. Plugging this into Eq. 3.18 and solving for the transimpedance of the circuit gives:

$$\begin{aligned} \frac{V}{I_-} &= -R_f\left(\frac{A}{1+A}\right) \\ &\approx -R_f \end{aligned} \tag{3.19}$$

In effect, the op-amp output signal is attempting to hold the potential difference between the two op-amp inputs to zero. This creates a virtual ground between the two photodiode which has the immediate advantage of holding the bias voltages stable. There are several other benefits to this scheme. We first note that changing the feedback resistance will not effect the input impedance from the prospective of the source. This is a desirable quality that helps isolate the photodiode from the gain resistor impedance and is not achieved through simple loading of a resistor. In the negative feedback configuration, the output of the op-amp has characteristically low input impedance which additionally isolates the gain resistor from further loading of the circuit upstream.

In reality, the op-amp allows some small but non-zero input bias current, I_b, to flow into the two inputs. This results in a small DC offset voltage in the output signal given by $-I_b R_f$. To counteract this, we add a resistor to ground in the non-inverting arm which shifts the hold point up by $I_b R_f$, thereby correcting for this offset. In addition, a capacitor is added in parallel to help shunt its noise.

3.2.2.2 AC analysis

To analyse the response of the detector to AC signals, we must consider the inherent bandwidth of the photodiode, all parasitic capacitance in the circuit, the finite op-amp gain bandwidth product, $A\omega_0$, and the phase compensation of the setup.

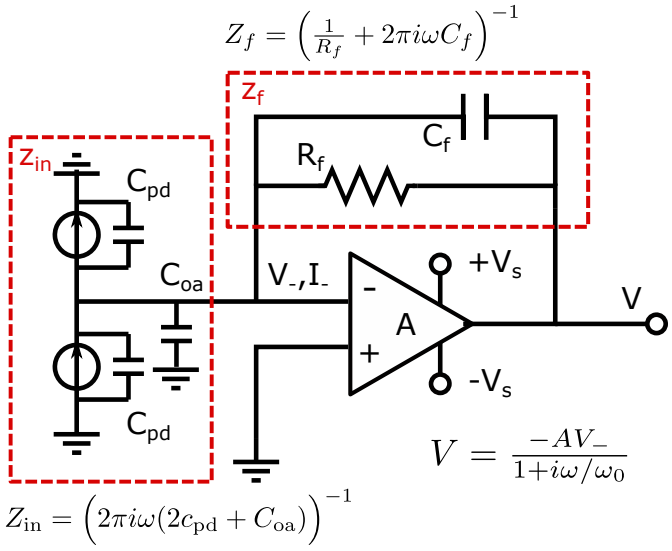

FIGURE 3.6. An AC electrical circuit diagram for TIA amplification of photosubtraction.

The photodiode bandwidth is determined by the response time of the diode to a pulse of light. The overall response time of the diode is the sum of different carrier drift, diffusion and relaxation process through the junction to the anode and cathode that occur under illumination along with the RC time constant of the connected circuit[125]. In the extended InGaAs PIN photodiode used here under 1 V reverse bias, the dominating time constant is likely to be set by the thermal diffusion of minority carriers (holes) through the non-depleted region through which they must travel to reach the cathode. This effect is more pronounced for longer wavelength applications such as ours. In any case, the overall response time of the photodiode is of the order nanoseconds under bias resulting in a gigahertz frequency response that does not limit the overall response of the homodyne detector.

Parasitic photodiode junction capacitance at the input of the op-amp results in unstable operation at higher frequencies[117]. In AC analysis, we can consider all voltage sources to be ground due to their constant nature. We can therefore consider the parasitic junction capacitance to be coupled to ground on the input to the TIA, Fig. 3.6. The input impedance of the TIA is similar to that of an inductor in that it rises with frequency. This effective inductance, in combination with the parasitic capacitance to ground, forms an LC circuit which oscillates with some resonate frequency. The effect is unstable operation close to this frequency. To counteract this, a feedback capacitance is added in parallel with the feedback resistor creating an RC filter to reduce the gain about the resonance. Appropri-

ate tuning of this capacitance can fully counteract the resonance leaving stable operation across the full bandwidth of the detector.

We can solve for the gain spectrum, $|\tilde{r}(\omega)|^2 = \left|\frac{V}{I_- R_f}\right|^2$, of a TIA by utilising first principles to solve for I_-:

$$I_- = \frac{V_-}{Z_{\text{in}}} + \frac{(V_- - V)}{Z_f}. \tag{3.20}$$

where Z_{in} is the impedance on the input and Z_f is the impedance on the feedback loop (defined in Fig. 3.5)[129]. To eliminate V_- we use the open-loop op-amp gain, Eq. 3.18, adapted to account for frequency dependence, given in Fig. 3.5. The resulting function is a second-order Butterworth filter function:

$$\begin{aligned} |\tilde{r}(\omega)|^2 &= \frac{1}{1 + (p^2 - 2)\frac{\omega^2}{\omega^{*2}} + \left(\frac{\omega^2}{\omega^{*2}}\right)^2}, \\ p &= \left(2\pi R_f C_f + \frac{1}{A_0 f_0}\right)\omega^*, \\ \omega^* &= \sqrt{\frac{A_0 f_0}{2\pi R_f (2C_{\text{pd}} + C_f + C_{\text{oa}})}}. \end{aligned} \tag{3.21}$$

where p and ω^* are parameterised by the components and feedback circuitry (see Tab. 3.2 for variable definitions). To produce the desired flat second-order Butterworth response, the feedback capacitor is chosen such that $p \approx \sqrt{2}$, at which point ω^* is then the 3-dB bandwidth of the device.

A further consideration with regards to stability is the phase acquired by the feedback signal. The open-loop op-amp applies some frequency dependent phase to the output signal. This frequency dependent phase, in combination with that applied by the RC filter and feedback trace, degrades the efficacy of the feedback signal. If the total phase exceeds 180 degrees then the feedback signal will no longer be held close to ground and will instead become unstable. We must therefore consider the total acquired phase when modelling potential components to ensure stability over the detectors bandwidth.

As mentioned previously, phase compensation is required to balance the LC circuit produced by the input circuit. Using these equations, we can find the optimal feedback capacitance to ensure a flat gain spectrum:

$$C_f = \frac{1 + \sqrt{1 + 8\pi R_f A_0 f_0 (2C_{\text{ph}} + C_{\text{oa}})}}{4\pi R_f A_0 f_0} \tag{3.22}$$

By inspection of Eqs. 3.21 with an optimal choice of C_f, we see that there is a natural trade-off between gain and bandwidth with $\omega^* \propto 1/\sqrt{R_f}$. The bandwidth

is also limited by the sum of parasitic capacitances in the system, which is ideally minimised. In choosing an op-amp, we must therefore consider the op-amp capacitance alongside the gain bandwidth product.

3.2.3 Noise considerations

In order to use the detector to measure vacuum quadrature noise, we need to have extremely low electrical noise in conjunction with good dynamic range. To give an idea of the level of current noise generated by a homodyne measurement of vacuum quadrature noise, let us assume that we have ideal, noiseless, detection such that $\eta_c = 1$ and $|\tilde{I}_\Omega| = 0$. Let us also assume that photodiode responsivity is 1.4 A/W, and that we are operating with a 2.07 µm LO with an average power of 1 mW. In this case, we can use Eq. 3.16 to find the expected current noise per root hertz that results from the amplified vacuum noise:

$$\begin{aligned} \langle I_-(\omega)\rangle &= \mathscr{R}\sqrt{2\frac{hc}{\lambda}\alpha_{\mathrm{LO}}^2} \\ &= 19.4\,\mathrm{pA}/\sqrt{\mathrm{Hz}} \end{aligned} \tag{3.23}$$

This small amount of current, as we will see, is comparable in magnitude to our dominant noise sources.

To model shot-noise clearance we must consider all dominant noise sources in the detector and compared them to the signal level. Since we are interested in performing optical shot-noise measurements in the 1 MHz–25 MHz range, we must also consider the frequency dependence of these sources.

Dark current shot-noise

The first source of noise to consider is electrical shot-noise resulting from electron-hole pairs that are generated in the depletion region, in the absence of light. Dark current is Poissonian in nature and thus has a variance equal to its mean value. By modelling the extraction of these independent electrons-hole pairs from the junction, it can be proven that the electron shot-noise is frequency independent[130] and gives rise to a white-noise current per root hertz of:

$$\langle I_d\rangle = \sqrt{2eI_d}\,. \tag{3.24}$$

Transimpedance amplifier noise

In addition to the dark current shot-noise, TIA contributes electronic noise observed in the absence of a signal. The total noise, $\langle I_{oa}^{\mathrm{tot}}\rangle$, can be modelled as a

combination of voltage, $\langle V_{oa} \rangle$, and current, $\langle I_{oa} \rangle$, supplies on the op-amp input originating from the internal elements of the op-amp, along with Johnson noise from the feedback resistor. Reference[129] provides a full derivation of TIA noise. $\langle V_{oa} \rangle$ and $\langle I_{oa} \rangle$ are quoted by the manufacturers and can be considered frequency independent above 100 kHz. In addition to these three sources, the input voltage noise interacts with the capacitive impedance at the input of the op-amp and gives rise to an additional current noise proportional to frequency. Johnson noise originates from the thermal motion of charge carriers within the resistor and is also considered a white-noise source. Combining all noise sources gives:

$$\langle I_{oa}^{\text{tot}} \rangle = \sqrt{\langle I_{oa} \rangle^2 + \left(\frac{\langle V_{oa} \rangle}{R_f} \right)^2 + \frac{4kT}{R_f} + \left(\frac{A_0 f_0 \omega}{R_f \omega^{*2}} \right)^2 \langle V_{oa} \rangle^2}. \tag{3.25}$$

Here, T is the temperature of the feedback resistor and k is Boltzmann's constant.

Bias voltage supply noise

In addition to TIA and photodiode noise sources, voltage supply noise, $\langle V_{\text{reg}} \rangle$, will couple through the photodiode into the signal from the bias supplies. As stated previously, the photodiode presents an impedance with magnitude given by $|Z| = \left(R_{\text{shunt}}^{-2} + (2\pi f C_{\text{pd}})^2 \right)^{-1/2}$ to the supply voltage. This frequency dependent contribution results in a current noise given by:

$$\langle I_s \rangle = \frac{\langle V_{\text{reg}} \rangle}{|Z|} \tag{3.26}$$

To minimise this, we employ ultra low-noise linear regulators[131]. For our chosen supplies, the voltage noise falls off exponentially across 1 MHz–25 MHz from 2 nV/$\sqrt{\text{Hz}}$ to 0.1 nV/$\sqrt{\text{Hz}}$.

Shot-noise clearance

We can combine our equations for the signal with the sum total of all noise sources to give an equation for the shot-noise clearance, expressed in dB. We will later use this equation to model the expected SNC for our chosen components:

$$\text{SNC} = 10 \log_{10} \left(1 + \frac{\langle I_- \rangle}{\sqrt{\langle I_{\text{oa}}^{\text{tot}} \rangle^2 + \langle I_d \rangle^2 + \langle I_s \rangle^2}} \right) \tag{3.27}$$

To efficiently measure optical shot-noise, it is important to have sufficient clearance above the noise floor of the detector, otherwise, the optical shot-noise is polluted with electrical noise. This is especially important when performing

sub-shot-noise measurements of optical noise in quantum states of light such as squeezed states. In such measurements, the electrical noise will always degrade the efficiency with which the true squeeze factor can be measured. Not only this, the noise floor will ultimately limit the total amount of detectable squeezing.

There are a few options to improve the the SNC. Doubling the LO power will provide double the clearance but this strategy is ultimately limited by op-amp saturation. It is for this reason that improved dynamic range is desirable. Increasing the feedback gain will also increase the SNC but at the expense of bandwidth. This strategy is only effective when op-amp voltage noise dominates the electronic noise. If dark current shot-noise is dominant, increasing the gain will not improve the SNC.

3.2.4 Common-mode rejection

The CMRR of a homodyne detector is defined as the ratio of the signal power with one photodiode blocked compared to the balanced configuration[132]. It is a measure of how well the correlated signal from each photodiode is rejected in the subtraction, leaving just the uncorrelated optical shot-noise. CMRR is degraded by slight variations in photodiode performance which causes an imbalance in the photocurrent. Under pulsed illumination, variation in the photodiodes capacitance will also effect common-mode rejection with each pulse becoming convolved with the finite response of each photodiode. The result is two slightly different pulses which no longer perfectly overlap. Pre-detection, optical path length differences between the two output ports of the homodyne detector will also introduce such mis-matches. Both effects degrade CMRR more at higher frequencies. To some extent, we can fine tune the optical path lengths to match and, additionally, we can tune the bias voltages of each photodiode independently to counteract photodiode variations.

The best CMRR achieved for 1550 nm homodyne detectors is 75.2 dB and requires fine-tuning circuitry to account for slight differences in transit time and responsivity between the two photodiodes[133]. Without this additional electronic tuning, small variations between photodiodes make it difficult to improve the CMRR beyond 60 dB. At 20 MHz, an optical path length difference of less than 1 mm is required to ensure an electronically-limited CMRR up to 60 dB[134].

3.2.5 Power considerations

The dynamic power range over which the detector can perform is bounded by the noise-equivalent power at the lower end and op-amp saturation power at the higher end. Each photodiode can also saturate, above which we can no longer assume a linear relationship between incident power and photocurrent, however, this tends to occur after the op-amp output saturates, despite DC rejection of most of the current in the subtraction. The response from PD25 remains linear below 2 mW of average optical power.

We can model the saturation power, P_{sat}, in the balanced configuration as being approximately equal to the LO power at which the TIA output signal has a $V_{\text{pp}} \approx 2V_s$. In reality, the detector will start to saturate just before this point signified by a drop in power spectral density across all frequencies. It is important to note that if the detector saturates at a single frequency, the electronics may oscillate and result in non-linear behavior across the rest of the spectrum. It is for this reason that we aim for a bandwidth less than the repetition rate of the laser.

Conversely, the noise equivalent power P_{nep} is defined as the optical power at which the signal-to-noise ratio is 3 dB. We will be considering both of these important metrics as we decide which components to use.

3.3 Component choice and projected performance

We design for optimal shot-noise clearance over a desired bandwidth of approximately 1 MHz–25 MHz. We are limited at the upper end of this frequency range by the repetition rate of the pulse laser as the TIA must have sufficiently low gain at the repetition rate to avoid saturating at this frequency. The tables below summaries the chosen components and their key metrics for optimal performance in the 2 µm–band. We model the expected gain spectrum, dynamic range and SNC in LTSpice[135] given our chosen components.

Table 3.1. A list of the key component model IDs used to build the homodyne detector. (Table taken from Ref.[92].)

Component	Model
Photodiodes	Laser Components (IG26X250S4i)
Op-amp	Analog Devices (ADA4817)
Negative Linear Regulators	Linear Technology (LT3094)
Positive Linear Regulators	Linear Technology (LT3045)

PD26 were used due to their relatively low junction capacitance and high responsivity compared with other leading manufacturers. A responsivity of 1.45 A/W gives a projected quantum efficiency of $\eta_{QE} = 86.5\%$ at 2.07 µm. We bias the detectors at $V_b = 1V$. Biasing at this higher voltage will ensure the diodes transit time response is sufficient for the diode to recover from pulse-to-pulse and therefore remain linear in power. The detector bandwidth is then limited by the TIA response. High bias voltage also has the benefit of further reducing the parasitic capacitance from the photodiode and thus improves detector speed for a given gain. The dark current is not specified above 0.25 V but using a source meter, we measure the dark current across 0 V to 1.1 V with a 1 V bias giving 6.4 µA dark current per photodiode, FIg. 3.7. We can extract the shunt resistance at 1 V bias as the reciprocal of the gradient giving 60 kΩ.

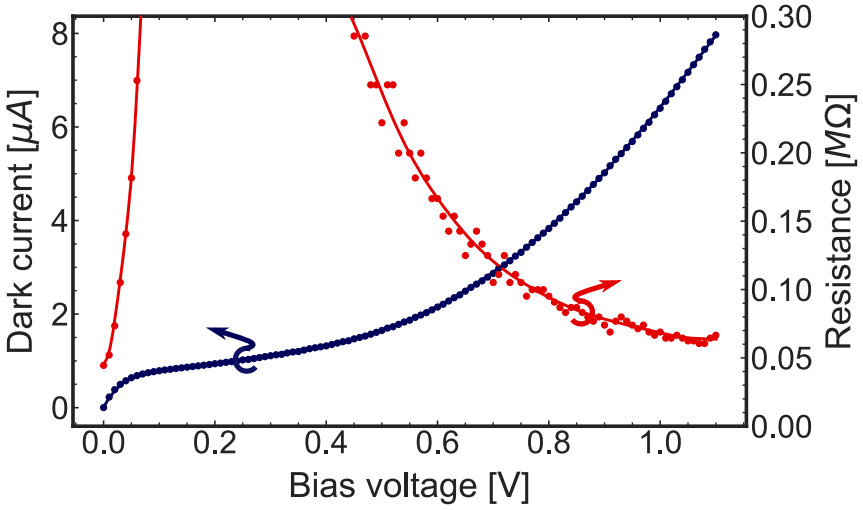

FIGURE 3.7. (a) photodiode IV curve under reverse bias as measured with a source meter and (b) the reciprocal of the gradient giving resistance at each bias voltage.

The resulting dark current shot-noise from two photodiodes in series is 2.03 pA/$\sqrt{\text{Hz}}$. Junction capacitance and dark current both increase with active area and so the photodiode with the smallest active area was chosen. Ideally, several photodiodes would be purchased and tested, with the most similar pair selected for use. We do not perform this step here due to limited funds.

Op-amp ADA4817 was chosen due to its low noise and appropriate gain bandwidth product. A gain resistor of 3.9 kΩ was chosen with a predicted 3-dB bandwidth of $\omega^* = 25$ MHz, assuming an estimated optimal feedback capacitor of

TABLE 3.2. A list of key components and their key properties including the photodiodes, op-amp and feedback circuitry. (Table taken from Ref.[92].)

Component	Property	Value
Photodiode	Responsivity @ 2.1 μm	1.45 A/W
	Junction Capacitance (C_{pd}) @ 1 V_b	8 pF
	Shunt Resistance (R_{sh}) @ T = 20°, 0 V_b	60 kΩ
	Dark Current @ 1 V_b	6.4 µA
	Active Region Diameter	250 µm
	Reverse bias	1 V
Op-amp	Gain Bandwidth Product ($A_0 f_0$)	410 MHz
	Voltage Noise @ 1 MHz	2 nV/$\sqrt{Hz}$
	Current Noise @ 100 kHz	2.5 fA/$\sqrt{Hz}$
	Input Bias Offset Current	1 pA
	Input Capacitance (C_{oa})	1.3 pF
Circuitry	Gain Resistor (R_f)	3.9 kΩ
	Feedback Capacitor (C_f)	4.7 pF
Supplies	Voltage Noise @ 1 MHz	2 nV/$\sqrt{Hz}$

1.43 pF. Using the key metrics in Tab. 3.2, we can calculated the theoretical noise contributions from each term discussed in the previous section along with the total predicted noise.

TABLE 3.3. A breakdown of expected photocurrent noise contributions from components presented in Tab. 3.1 using equations presented in the previous section. (Table taken from Ref.[92].)

Noise Source	pA/$\sqrt{\text{Hz}}$
Dark current shot-noise @ 1 V_b	2.03
Op-amp input current noise	0.0025
Op-amp voltage noise through the feedback resistor @ 1 MHz	0.51
Feedback resistor Johnson noise @ T = 300 K	2.06
Op-amp frequency dependent noise @ $\omega*$ = 25 MHz, 1 MHz	0.34
Bias supply current noise @ 1 V_b, 1 MHz	1.42
Root sum squared total noise @ 1 MHz:	3.28

The two largest noise sources are from the dark current shot-noise and feedback resistor. Increasing the gain resistor would mitigate the resistor noise to a certain extent but would not help counter the dark current shot-noise. We model the circuit in LTSpice to more accurately predict the key characteristics and fine tune the feedback capacitance. Based on this analysis, a feedback capacitor of 4.7 pF was chosen. Figure 3.8 models the gain spectrum with an estimated 3-dB bandwidth of 15 MHz and −7.5 dB of suppression at the repetition rate of the

laser. The acquired phase in the feedback signal remains well below the stability threshold of 180 °. We expect to see a SNC of up to 12.5 dB at 1 MHz with an LO power of 0.5 mW. $P_{\text{nep}} \approx 30\,\mu\text{W}$ at 1 MHz.

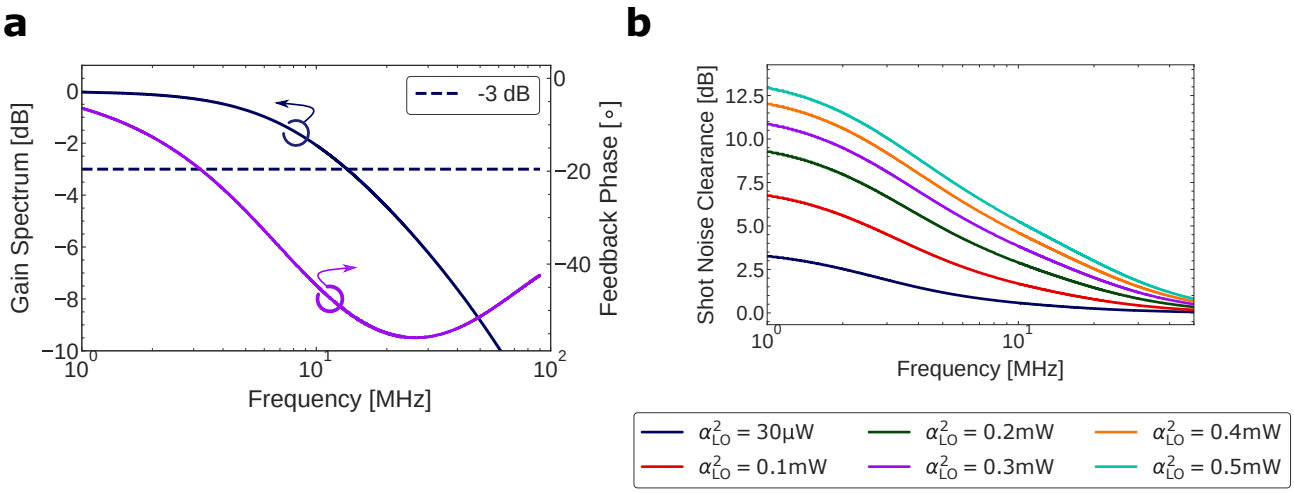

FIGURE 3.8. Simulated homodyne detector (a) gain spetcrum (blue, left) and phase (purple, right). The 3 dB gain point is marked (dashed blue). (b) shot-noise clearance for several local oscillator powers. Both plots have a logged x-axis.

3.4 Detector design and layout

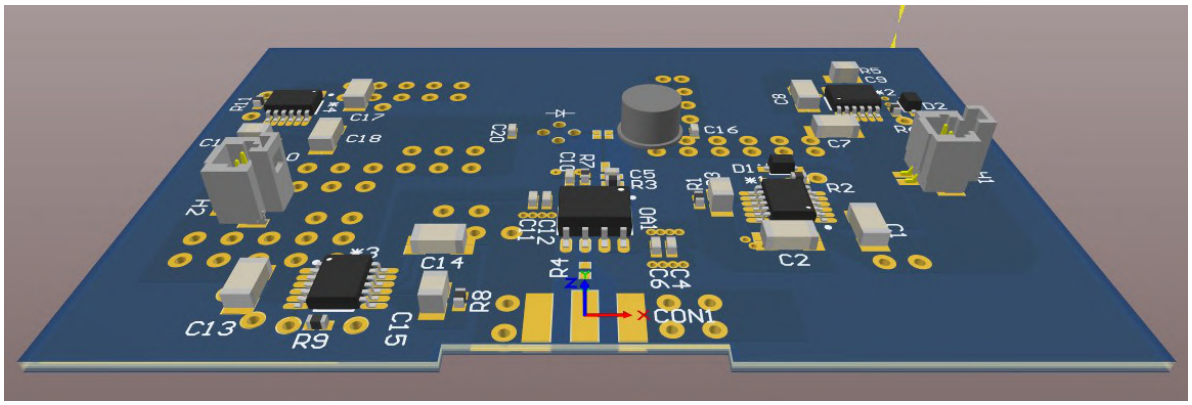

FIGURE 3.9. A 3D model of the printed circuit board designed for homodyne detection. A circuit schematic is given in Fig. 3.10

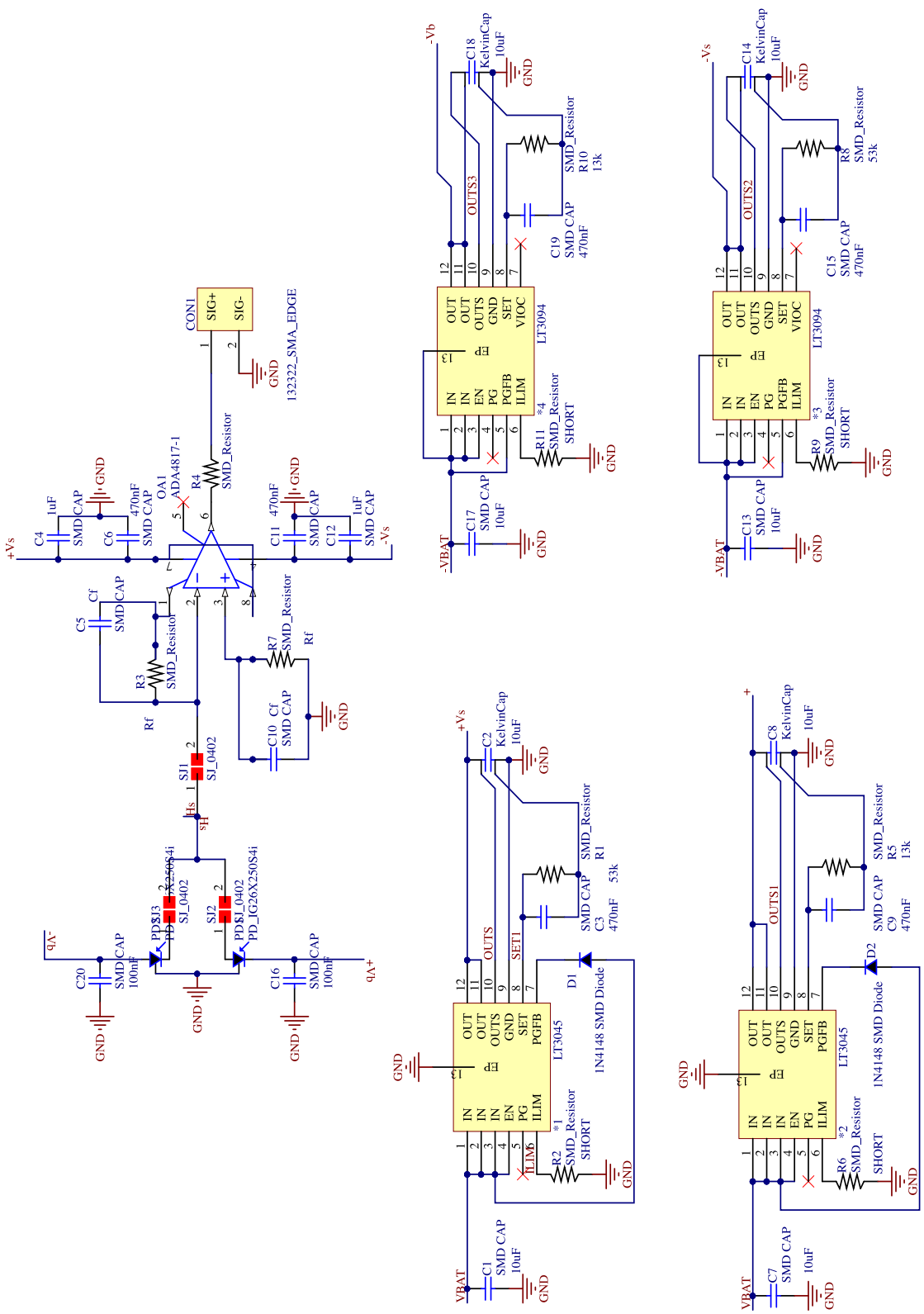

FIGURE 3.10. Full electrical circuit of the homodyne detector showing the battery connectors, positive and negative power supplies, TIA, SMA readout channel and photo-subtraction configuration. Additional decoupling capacitors have been added to suppress noise along with solder jumps for isolated testing and debugging.

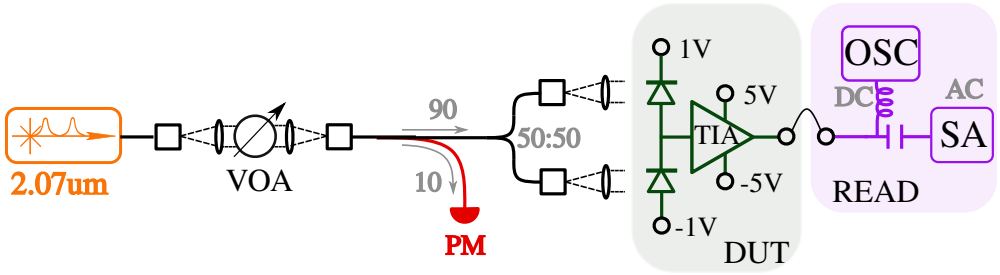

FIGURE 3.11. Experimental diagram of the characterisation setup. A pulsed laser propagates through a variable optical attenuator, split 50:50 via a homodyne beamsplitter and then coupled into each side of the photodiode. Readout is performed via an oscillacope (DC) and spectrum analyser (AC). (Figure adapted from Ref.[92].)

Figures 3.9 & 3.10 show the board layout and schematic respectively. A number of decoupling capacitors have been set to ground on the power and bias supplies with the aim to decouple excess noise in these signals. The power is supplied via two 9 V batteries as batteries provide a lower noise DC voltage source compared to that obtained via a mains transformers. To enable free space coupling into each diode with minimal trace length between them, one is soldered to the back of the PCB and one to the front. The subtraction trace has been isolated from the other planes to reduce parasitic capacitance.

3.5 Device characterisation and vacuum noise detection

The setup used to characterise the detector is depicted in Fig. 3.11. A pulsed 2.07 µm fibre mode-locked laser (AdValue Photonics AP-ML-1) is used for full characterisation. The laser light passes through a free space variable optical attenuator (VOA) and is then coupled back into SMF28 fibre. The VOA consists of a razor blade on a motorised translation stage, used to partially block the beam. The overall insertion loss of the VOA is 4.1 dB. From here, the laser passes through a fibre beam splitter with an intended splitting ratio of 90:10. We characterise this splitter to have an insertion loss of 0.44 dB and an actual splitting ratio of 88.7:11.3. The 11.3% arm is detected via a power meter and is used to monitor the input power. The 88.7% arm is split again via a 50:50 fibre splitter (Thorlabs TW2000R2F1B) with each arm coupled into the photodiodes (PD^+ and PD^-) of the detector. A set of lenses with anti-reflection coating (Thorlabs C037TME-D)

are used to focus the beams down onto PD^+ and PD^-. It is important to match the path lengths to each photodiode from the fibre splitter to ensure good temporal overlap in the subtraction with imbalances in path length leading to poor common-mode rejection at higher frequencies. This is achieved by maximising the rejection of the repetition rate in the output RF signal. The RF output of the detector is split via a bias tee into its DC and AC components. The DC is coupled into an oscilloscope (Tektronix TDS2012B) and the AC component is coupled into an 6 GHz electrical spectrum analyser (FieldFox model N9912A).

We optimise the coupling of each arm separately by temporarily blocking the other and maximising the DC signal for fixed input power. The beam must be focused onto the photodiode's active region with the optimal coverage given by a beam waist slightly less than the active area diameter. We do not focus any tighter to avoid the risk of a nonlinear response from the detector.

The total conversion efficiency, defined as the product of the coupling η_c and quantum η_{QE} efficiencies, is extracted for each photodiode. This is achieved by successively blocking each photodiode and measuring the increase in DC voltage as a function of incident power. PD^+ and PD^- have total efficiencies of $65.3\% \pm 1.5\%$ and $66\% \pm 2\%$ respectively, Fig. 3.12(a). The voltage offset is measured to be 2.4 mV at room temperature, though this is expected to be temperature-dependent.

Figure 3.12(b) plots the detector gain as a function of frequency. Fitting to the data, we obtain $p = 1.76$. Fine-tuning the feedback capacitor can improve this further. Since the response is not perfectly flat, ω^* will overestimate the true bandwidth. By reading off -3 dB from the fit we determine the bandwidth to be 13.2 MHz.

For homodyne detection of the vacuum, we ensure the detector remains balanced on V_{offset} via the DC signal. We then measure $\langle \hat{p}_\Omega \rangle$ with the spectrum analyser for a range of input laser powers. Figure 3.13(a) plots the output spectrum for increasing laser powers with a resolution bandwidth of 100 kHz. By subtracting the electronic-noise spectra from the shot-noise response and averaging over 1 MHz–13 MHz, we can perform a linear fit to the average voltage variance from the detector with power (Fig. 3.13(b)). We obtain a linear fit with an $R^2 = 0.99$. Note that the detector starts to display saturation above 1.8 mW; these points have been omitted from the regression. The detector electronic current noise level averaged across 1 MHz–13 MHz is 2.79 pA/$\sqrt{\text{Hz}}$ with a shot-noise equivalent incident power of 19 µW.

As mentioned previously, the CMRR of a homodyne detector is defined as the ratio of the signal power with one photodiode blocked compared to the bal-

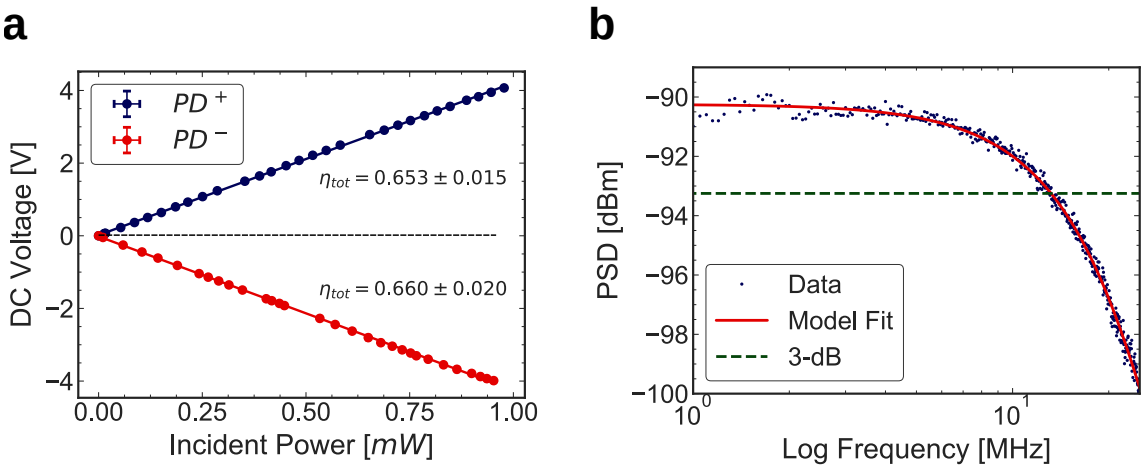

FIGURE 3.12. (a) the DC response from consecutively blocking PD^+ and PD^-. Statistical deviation from a continuous 10-second measurement has been accounted for and total conversion efficiency has been extracted via linear regression. (b) is the detector response with the electronic noise subtracted. From this signal we can fit to the gain spectrum. Data acquired with a resolution bandwidth of 100 kHz and video bandwidth of 100 Hz (blue) fit to a second-order Butterworth function (red) Eq. 3.21 with $p = 1.76$, $f^* = 16$ MHz, $R^2 = 0.82$. (Figure adapted from Ref.[92].)

anced configuration[132]. We perform this measurement using the signal power at the repetition rate of the laser since this supplies a strong classical signal that is not fully rejected by the subtraction. In contrast to the definition of CMRR, we perform the blocked measurement by re-routing all optical power to one photodiode, labelled 'Addition' in Fig. 3.14. When only one photodiode is used, the photocurrent is proportional to optical intensity, and thus, the PSD of the electrical signal is proportional to optical intensity squared. The addition signal from the detector contains twice the optical power (+ 3 dB) compared to the subtraction and consequently the detector PSD is (+ 6 dB) greater when compared to the standard definition of CMRR. We therefore correct the difference of 54 dB by -6 dB to extract a true CMRR of 48 dB, Fig. 3.14.

3.6 Discussion

The detector quantum efficiency η_{QE} at 2.1 µm is quoted by the manufacturer to be 86.5%. In practice, it is difficult to decouple the true responsivity of each photodiode from the coupling efficiency η_{coup} obtained in our setup. Assuming the

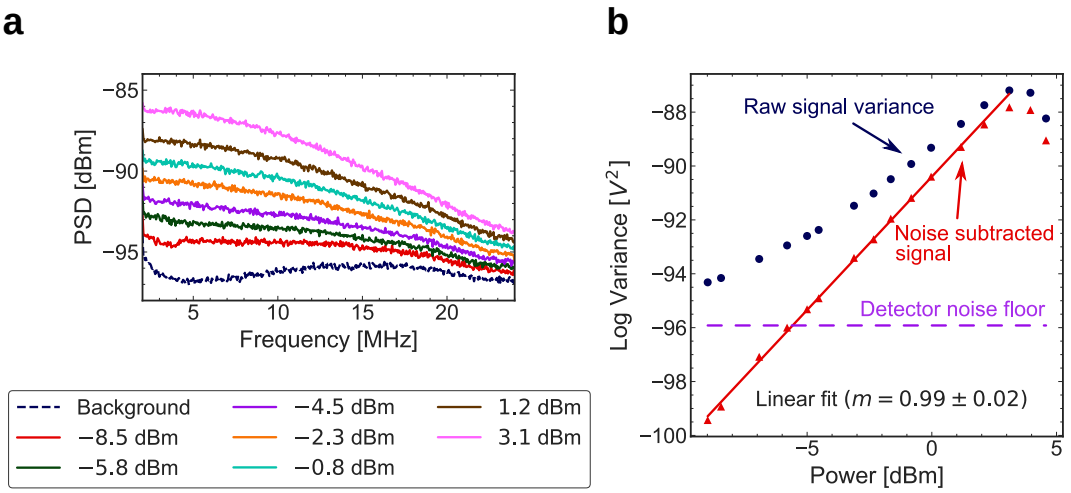

FIGURE 3.13. (a) PSD averaged over 30 traces for varying input power as measured with a the balanced homodyne detector. The measurement resolution bandwidth is 300 kHz, with a video bandwidth of 10 kHz. A moving point average with a Gaussian kernel has been applied with a FWHM of 1.5 MHz. (b) the average noise variance over the frequency range 1 MHz–13 MHz as a function of incident power (blue). Linear regression has been performed via least-squares giving a fit with $R^2 = 1.00$ (red). (Figure adapted from Ref.[92].)

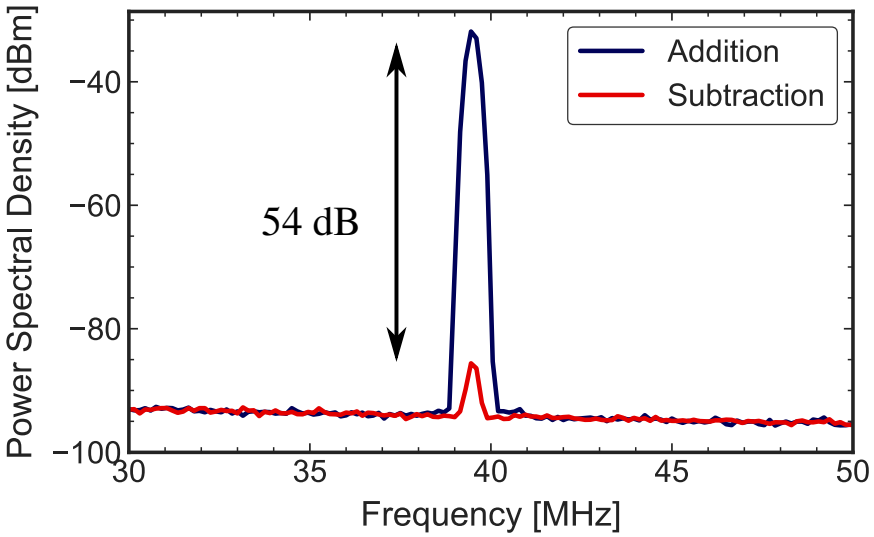

FIGURE 3.14. A comparisson of subtracted and addition photocurrents at the repetition rate of the laser obtained to calculate the CMRR. An LO power of −4.5 dB was used and rejection was first optimised via optical path length tuning. (Figure adapted from Ref.[92].)

quoted η_{QE} is nominal, we then calculate η_{coup} to be 75% for both photodiodes (Eq. 3.17). Coupling efficiency is limited by Fresnel reflections at the air-glass interfaces of the fibre launch, the focus lens and the photodiode housing. It can in principle be improved by using fibre coupled photodiodes with ≤1 dB insertion loss, which are currently only commercially available, at greater expense, when custom made.

In measurements of continuous-variable quantum states, the signal-to-noise ratio (SNR) also effectively degrades the total efficiency. For a given SNR in dB, the corresponding measurement efficiency is $\eta_{SNC} = (SNC - 1)/SNC$[68]. In practice, the negative effect of electronic noise on such measurements can be mitigated by increasing LO power to just below the detector saturation power. The SNR of the detector close to saturation is 9 dB (at 5 MHz) with a corresponding efficiency of $\eta_{SNC} = 88\%$. The total efficiency of the detectors for squeezed light detection at 5 MHz is therefore limited to $\eta_{tot} = \eta_{SNC}\eta_{coup}\eta_{QE} = 57\%$. The main limitation here is not linked to the fundamental properties of the detector but is instead due to the poor coupling efficiency of the photodiodes. Employing state-of-the-art fibre-coupled photodiodes, the total detector efficiency at 2 µm could be readily increased to $\eta_{tot} = 73\%$. Although this is still below standard telecoms band efficiencies of $\eta_{tot} = 95\%$[136], sub-shot-noise measurements are possible with such a device.

By developing a shot-noise limited detector that demonstrates 57% efficiency at megahertz-speeds, we remove a crucial roadblock to quantum state development in the 2 µm–band that will help enable further development of prospective technologies including broadband 2 µm squeezing for quantum-enhanced metrology[50], SWIR-based ground-to-satellite quantum-key distribution[106] and remote LIDAR sensing[137,138]. Specifically, the increase in speed from kilohertz to megahertz could help facilitate the implementation of CV quantum information processing[139] and optical neural networks[140,141] which stand to benefit from reduced two-photon absorption in silicon in the 2 µm–band. By developing a detector that affords a high signal-to-noise ratio, we also help facilitate higher sensitivity in classical schemes that employ balanced detection to monitor amplitude modulation signals[108], reject classical laser noise[109] or map information from optical frequencies to the RF via coherent heterodyne beating of optical frequency combs[110].

The detector bandwidth was designed to sufficiently suppress amplification of the repetition rate of the laser used in our experiment (39.5 MHz). Without doing so, the detector is at risk of saturating at a single frequency which in turn

can cause non-linear behavior in other parts of the spectrum, which can skew the quadrature measurement. By observing the AC signal on the oscilloscope, we see that the detector saturates at the repetition rate first suggesting greater suppression may increase the saturation power further. However, this would come at the cost of decreased detector bandwidth and must be considered for each specific application. Another important consideration is that the quadrature measurement efficiency has been proven to be negatively affected for detector bandwidths less than half the repetition rate of the laser[114]. This is a direct result of each pulse running into the previous pulse which mixes the temporal mode of the quadrature measurement across consecutive pulses. One approach to increase the bandwidth of shot-noise limited performance is to miniaturise the detector's electronic and optoelectronic components to curtail overall capacitance[68]. GeSn integrated detectors for integrated photonics platforms are also being developd that are sensitive to the SWIR and promise a considerable increase in speed[142].

The best CMRR achieved for 1550 nm homodyne detectors is 75.2 dB and requires fine-tuning circuitry to account for slight differences in transit time and responsivity between the two photodiodes[133]. Without this additional path tuning, small variations in transit time make it difficult to improve the CMRR beyond 60 dB. The path length difference between each arm was fine-tuned to maximise rejection inferring 48 dB to be limited by such variations.

3.7 Characterisation of pulsed laser noise

In the next chapter, we present a device capable of classical noise suppression. In preparation for the design & simulations of the device used, we measure the additional classical intensity noise present in the pulsed laser above the shot-noise, Fig. 3.15. This measurement is carried out using the setup depicted in Fig. 3.11. To measure the total noise signal in the pulse laser, we divert all power to one photodiode on the detector. This is then compared to a balanced measurement with the same total input power in which classical noise is rejected leaving only shot noise. Figure 3.15 plots the total noise (red), shot-noise (green) and background detector noise (blue) for an input power of −5 dBm.

The pulsed laser has additional intensity noise above the shot-noise limit across the detector bandwidth, with a peak around 5 MHz of 6 dB of additional noise. Additional intensity noise from pulse-to-pulse can stem from a number of sources and we refer the reader to Section 4.5.1 for a discussion on this. We attribute the peak to intensity noise coupling from the Thulium seed laser used

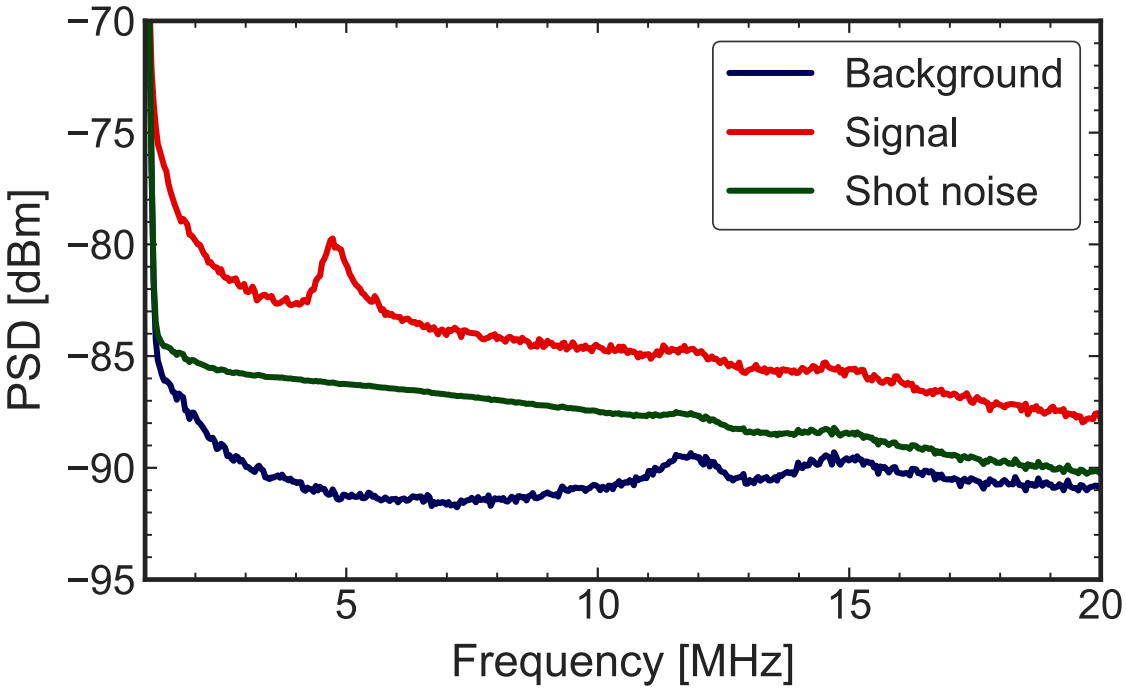

FIGURE 3.15. A breakdown of pulsed laser classical noise (red), shot-noise (green) and background detector noise (blue) for an input power of −5 dBm. A resolution bandwidth of 300 kHz and video bandwidth of 100 Hz was used to acquire the data.

to pump the gain medium in which the pulses are formed[143]. We note that the level of noise above the shot-noise is power dependent with a doubling of incident power leading to a 6 dB increase in classical noise but only a 3 dB increase in shot-noise.

3.8 Conclusion

We have given an overview of the theory and operating principles of homodyne detection for quantum technology, and we have presented a shot-noise limited homodyne detector designed for quantum measurement of pulsed light in the 2 µm–band. Using this detector, we measure megahertz vacuum fluctuations and verified the detector to be shot-noise limited, indicating its efficacy for detecting quantum light and for characterising quantum light fields. Despite the sub-optimal electrical characteristics of the available photodiodes in this band, we show that this does not preclude quantum measurements. The device efficiency of 57% is sufficient to measure Wigner function negativity[72] which requires

≥ 50% overall detector efficiency. We comment on the efficiency of the detector in relation to applications of squeezed light. We note the main limitation on device efficiency to be coupling efficiency, not the fundamental speed or dark current of the extended InGaAs photodiodes. The advent of such a detector opens the door to the measurement and verification of exotic quantum states in the 2 µm–band and is of sufficiency efficacy to employ in future cutting-edge quantum noise limited and quantum-enhanced metrology schemes. Additionally, this detector can also provide a route towards increased signal-to-noise ratio of balanced detectors utilised in schemes to measure weak modulation signals.

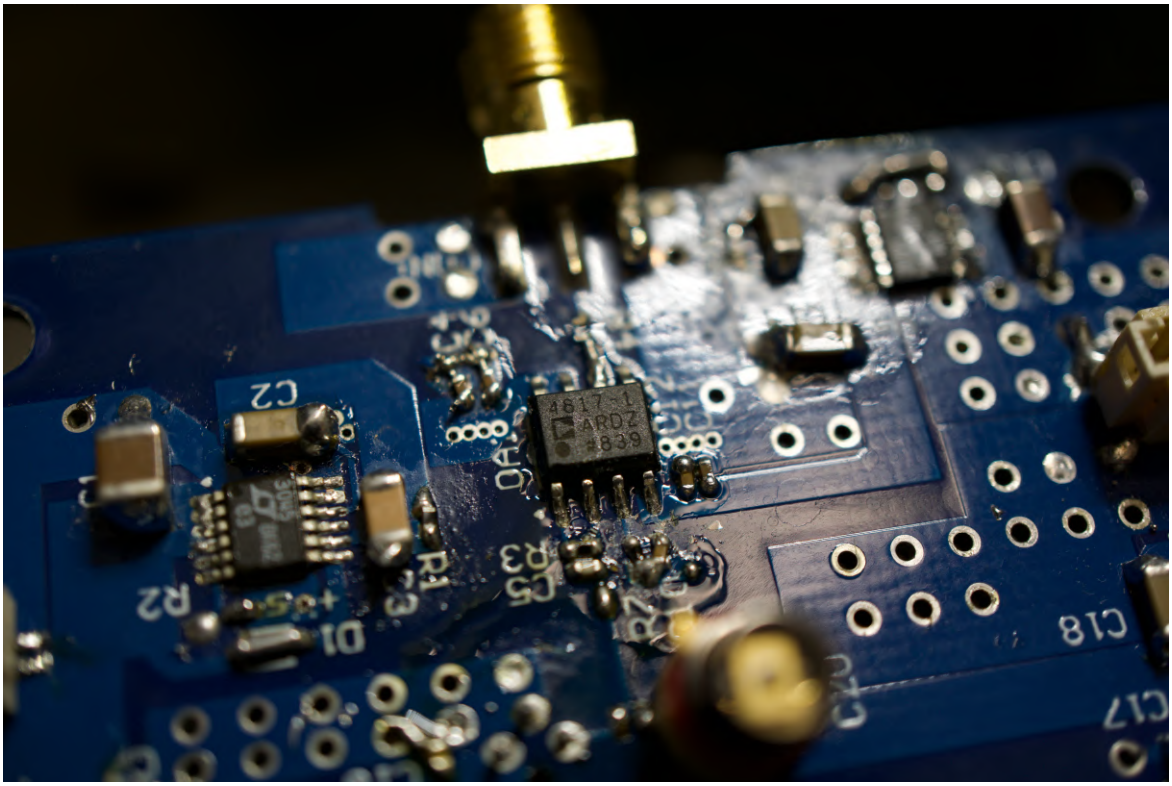

FIGURE 3.16. A photograph of the homodyne detector presented in this chapter (taken by J. W. Silverstone).

Chapter 4

An All-optical Noise Reduction Scheme for Integrated Absorption Spectroscopy in the 2 µm-band

Declaration of contribution: *the integrated devices investigated here were designed by Euan Allen and Lawrence Rosenfeld. The modelling of both the quantum and classical noise limited pulse propagation through the devices was completed solely by me, along with device characterisation and the experimental noise suppression investigation.*

In this chapter, we present an all-optical silicon photonic integrated circuit (PIC) capable of broadband pulsed-laser amplitude noise reduction in the 2 µm-band. In chapter 1 we discussed the motivation behind developing low noise sources of light for absorption spectroscopy schemes and we saw how utilising silicon PIC technology for 2 µm-based applications has the potential to benefit from reduced TPA and increased Kerr-nonlinearity. In the scheme presented here, it is exactly these two favorable properties that we leverage in an attempt to reduce the relative intensity noise (RIN) from a state-of-the-art 2 µm pulsed laser. The devices presented in this chapter are asymmetric Kerr interferometers that were originally designed by Allen *et al.* in Ref.[144] for 2 µm amplitude squeezing and were fabricated by the Cornerstone fabrication facility based in Southampton. Here, we model two scenarios 1) their ability to reduce amplitude quadra-

ture noise under a shot-noise limited laser approximation and 2) their ability to reduce intensity noise under a noisy laser approximation (Sec. 4.1). We then fully characterise the devices (Sec. 4.3), and measure their effect on RIN (Sec. 4.5).

The intensity noise in a laser is a combination of 1/f classical noise sources, such as thermal vibrations in the resonator, noisy drive electronics & mode hopping, and quantum noise sources stemming from intracavity spontaneous emission near resonance and loss-induced vacuum fluctuations far from resonance[145,146]. These noise sources present a significant limitation to high-precision metrology with classical 1/f noise dominating at slower speeds and quantum noise dominating at faster speeds. While some sensing schemes circumvent noise limitations by modulating the target information out to higher frequencies where laser noise is limited only by quantum shot-noise[27,28,147], others employ active or passive noise reduction techniques to overcome this limitation[148]. In active noise suppression, feedback or feed-forward circuitry is used in conjunction with electro-optic modulators to correct for intensity fluctuations in the laser[149,150]. Such schemes, reliant on potentially noisy electronic feedback, are often bandwidth limited by the speed and accuracy of the feedback circuit to ≤10 kHz. In addition, active schemes are limited by the noise characteristics of their drive electronics and can therefore not suppress noise arbitrarily close to the the shot-noise limit. It is possible to employ a hybrid approach in which an optical amplifier is used to improve the bandwidth of the suppression out to GHz[151], however, there are currently no active noise eaters commercially available for 2 µm applications.

Passive techniques employ optical interference, often in conjunction with photocurrent subtraction, to suppress classical intensity noise in the laser. Examples include: rejection of classical noise via balanced detection[71], frequency dependent noise suppression via coherent pulse train interferometry[144], and suppression via nonlinear interferometry (often to levels below the shot-noise limit)[152–154]. Pioneering work in fiber-based and free space optical sensing has already demonstrated bright squeezing via nonlinear interferometry which has subsequently enabled numerous quantum-enhanced metrology schemes[50,112].

Integrated, passive, classical intensity noise reduction in the telecoms band has so far been limited, despite several promising schemes well-proven in fiber[153,155]. Admittedly, this is mostly due to the relative ease of purchasing a shot-noise limited laser at these well supported wavelengths. As such, the last 20 years has seen a strong research focus on the generation of integrated sub-classical noise suppression, with the first integrated squeezing demonstrations using lithium niobate in 2002[156]. With low propagation losses, a relatively high

$\chi^{(3)}$ nonlinearity, and the advent of dual platform silicon – silicon nitride fabrication capabilities which enable the smooth integration of active components, silicon nitride has recently taken over as the preferred integrated squeezing platform. Integrated SiN squeezing dates back to 2015 and all subsequent results are summarised in Table 4.1 below. To date, squeezed state production in silicon has

TABLE 4.1. A summary of silicon nitride integrated squeezing results. DFWM—degenerate four wave mixing, OPO—optical parametric oscillator and DPFWM—dual pump four wave mixing.

Author	Year	Type of Squeezing	Method	Amount
Hoff[136]	2015	Bright Kerr	SiN Ring-enhanced Kerr	4.5 dB
Dutt[157]	2015	Photon number difference	SiN ring DFWM	5 dB
Dutt[158]	2016	Two-mode squeezing	SiN OPO	3.9 dB
Cernensky[159]	2019	Kerr squeezed vac.	SiN Asymmetric Sagnac	1 dB
Vaidya[160]	2020	Single-mode squeezed vac.	SiN Ring-based FWM	4 dB
Vaidya[160]	2020	Photon number difference	SiN Ring-based FWM	7 dB
Zhang[161]	2021	Single-mode squeezed vac.	SiN DPFWM	8 dB

not been achieved due to a range of parasitic effects at 1550 nm. These include power-limiting nonlinear loss from TPA and parasitic broadband noise, stemming from free-carrier absorption and inelastic scattering effects, that swamp any achieved noise reduction[162]. As mentioned in chapter 1, some of these effects are circumvented by moving to 2 µm, however, shot-noise limited lasers are not available at this wavelength and, to the author's knowledge, all previous integrated squeezing result have relied on shot-noise limited lasing. Since active noise eaters are also not yet commercially available in this band, we must therefore look to passive solutions to suppress the excess classical noise in currently available lasers.

In this chapter we present a passive silicon PIC device which we model to be capable of classical intensity noise suppression via the use of a Sagnac-style nonlinear Kerr-based interferometer. We start by reviewing classical Kerr nonlinearity and how it leads to SPM (Sec. 4.1). We then move on to discuss how SPM may be utilised in an asymmetric interferometer to reduce classical intensity noise (Sec. 4.1.4). We utilise a well known model to estimate an upper bound for the amount of amplitude squeezing attainable with these devices, assuming a shot-noise limited pulse laser (Sec. 4.1.6). We then adapt this model to account for excess classical noise over quantum noise (Sec. 4.1.7). Although these specific devices were designed by Allen, we discuss the key design considerations with

respect to optimal noise suppression (Sec. 4.2). In the final section, we present device characterisation and discuss the measured noise suppression capabilities (Sec. 4.3).

4.1 Noise suppression using Kerr interferometers

We start by examining how silicon responds to a bright optical fields.

4.1.1 Kerr nonlinearity

Given a sufficiently intense electromagnetic field, the response from any guiding dielectric medium will become nonlinear[86]. In affect, this is due to the anharmoinc motion of electrons within the medium no longer being sufficiently captured by a simple harmonic model. In an isotropic material, the total polarisation **P** induced from the electric dipoles created within the medium is nonlinear in **E**, the applied instantaneous electric field (assumed to have linear polarisation). Since **P**(**E**) can be considered a continuous function, we can perform a Taylor expansion in **E** and keep only leading order terms[86]:

$$\mathbf{P} = \epsilon_0\left(\chi^{(1)} + \chi^{(3)}|\mathbf{E}|^2\right)\mathbf{E}. \tag{4.1}$$

Here, ϵ_0 is the vacuum permittivity constant and $\chi^{(i)}$ is the i-th order susceptibility, given here by a complex scalar. By performing this expansion, we can characterise materials by their level and order of susceptibility. Due to the inversion symmetry of silicon its second-order susceptibility is zero making $\chi^{(3)}$ its largest non-zero nonlinear response[163]. Materials in which $\chi^{(3)}$ dominate are coined Kerr mediums after John Kerr who discovered a resulting effect known as nonlinear refraction[164]. In general, the Kerr effect describes the parametric coupling of two fields of frequency ω_1 and ω_2 to two output fields of equal frequency. For real $\chi^{(3)}$, where the silicon polarisation does not lead to absorption, a nonlinear refractive index is induced, known as self-phase modulation (SPM), which affects the spectral properties of the laser.

4.1.2 Self-phase modulation

The refractive index of the material, given by $n = \sqrt{1+\chi}$, is consequently expanded into a leading term and small perturbation:

$$\begin{aligned} n &= n + \Delta n, \\ &= n_1 + n_2|\mathbf{E}|^2 \end{aligned} \tag{4.2}$$

$n_1 = \sqrt{1+\chi^{(1)}}$ is the linear refraction coefficient and $n_2 = 3\chi^{(3)}/4n_1^2\epsilon_0 c$ is the nonlinear refraction coefficient. For a wave packet with frequency ω propagating a distance L along the material, with propagation constant k, the induced instantaneous SPM is given by:

$$\begin{aligned}\phi_{\mathrm{NL}} &= \frac{kLn_2P}{A}, \\ &= \gamma LP \quad [2\pi].\end{aligned} \tag{4.3}$$

where P is the power, A is the modal areas and $\gamma \equiv \omega n_2/Ac$ is the waveguide, material and wavelength specific nonlinear propagation constant used to characterise the amount of SPM applied to the field. We will now use the nonlinear propagation constant in a formal derivation of the governing differential equation for a bright classical pulse propagating through a Kerr medium, known as the nonlinear Schrödinger equation.

4.1.3 Pulsed self-phase modulation

Using Maxwell's equations for the flux densities induced by a propagating electromagnetic field through a polarised material[87], we can eliminate the magnetic fields in favour of the electric fields to give a governing equation for the propagation of an electric field through a dielectric[86]:

$$\nabla^2\mathbf{E} - \frac{1}{c^2}\frac{\partial^2\mathbf{E}}{\partial t^2} = \mu_0\frac{\partial^2\mathbf{P}}{\partial t^2}, \tag{4.4}$$

in which $\mu_0 = 1/\epsilon_0^2c^2$, and $\mathbf{E}(\mathbf{r},t)$ and $\mathbf{P}(\mathbf{r},t)$ are the applied electric field and polarisation field, respectively. We will make the assumption that the field is linearly polarised along the unit vector $\hat{\mathbf{x}}$ which does not change along the length of propagation. We also make the assumption that the pulse is quasi-monochromatic, i.e. $\Delta\omega/\omega_0 \ll 1$ where $\Delta\omega$ is the pulse width and ω_0 is the central frequency.

Immediately, we can insert our third order approximation for the polarisation field of a Kerr medium, Eq.4.1, into Eq.4.4. Defining a new, adapted, permittivity $\epsilon = (1+\chi^{(1)}+\chi^{(2)}|\mathbf{E}|^2)$, we get:

$$\nabla^2\mathbf{E} = \frac{\epsilon}{c^2}\frac{\partial^2\mathbf{E}}{\partial t^2}, \tag{4.5}$$

the governing wave equation with a power dependent propagation constant. We can represent the electric field as a combination of a slowly varying pulse envelope along the direction of propagation, $A(z,t)$, a perpendicular mode distribution described by $F(x,y)$ and a fast varying propagation phase such that:

$$\mathbf{E}(\mathbf{r},t) = \frac{\hat{\mathbf{x}}}{2}\Big(F(x,y)\,A(z,t)\,e^{i(\beta z-\omega_0 t)} + \text{c.c.}\Big). \tag{4.6}$$

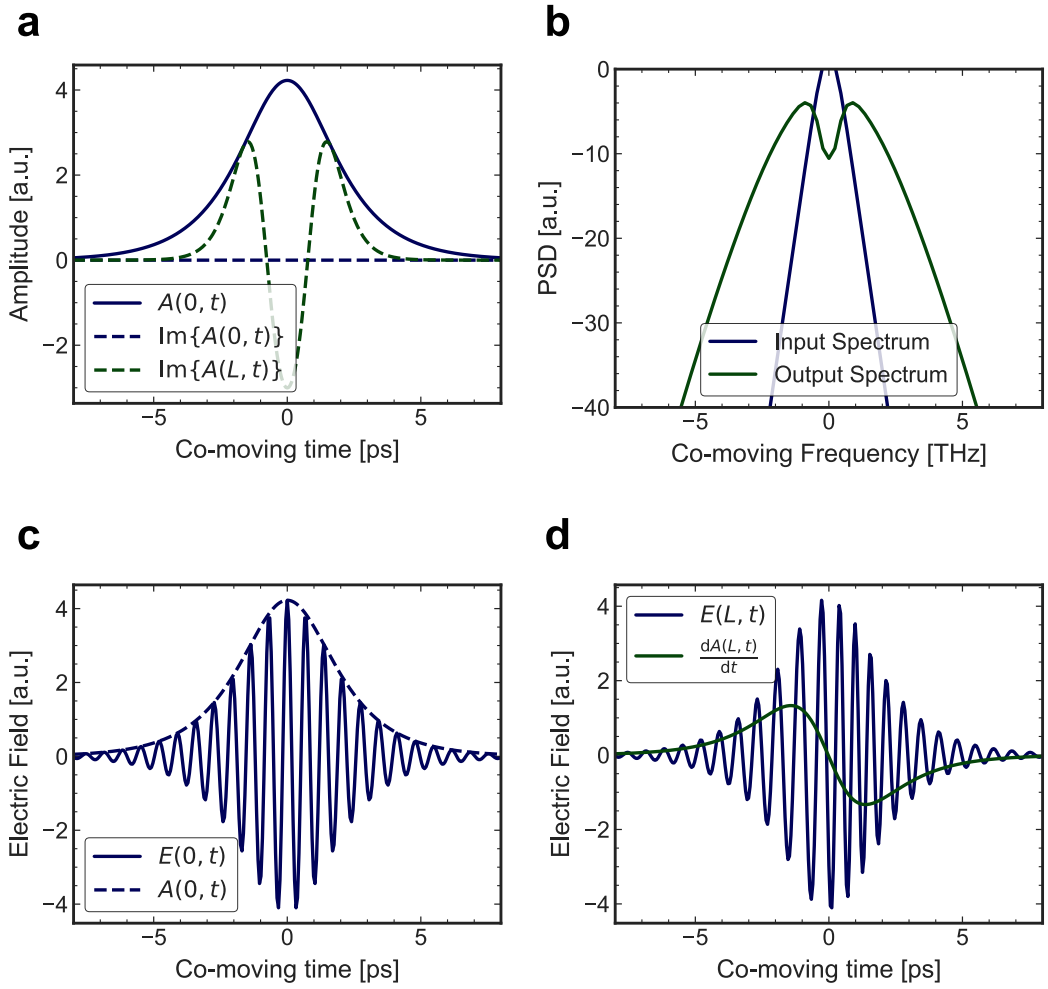

FIGURE 4.1. (a) Input envelope magnitude (blue), input envelope phase (blue-dashed) and output envelope phase after propagation through 1 mm of lossless silicon waveguide (Cornerstone strip). (b) the associated pulse spectrums. (c) The electric field of the input pulse showing carrier oscillations. (b) the chirped output electric field (blue) with phase shift proportional to the rate of change of the envelope magnitude (green-dashed).

To solve Eq.4.5, we take the Fourier transform and apply separation of variables to give an eigenvalue problem. The Fourier transform of Eq.4.6 is given by

$$\tilde{\mathbf{E}}(\mathbf{r}, \omega - \omega_0) = \int_{-\infty}^{\infty} \mathbf{E}(\mathbf{r}, t) e^{i(\omega-\omega_0)t} dt. \tag{4.7}$$

Taking the Fourier transform of the differential Eq.4.5,we get

$$\nabla^2 \tilde{\mathbf{E}} + \epsilon k_0^2 \tilde{\mathbf{E}} = 0, \tag{4.8}$$

where $k_0 = \omega_0/c$. We assume the solution to this equation has the separable form:

$$\tilde{\mathbf{E}}(\mathbf{r}, \omega - \omega_0) = F(x, y)\tilde{A}(z, \omega - \omega_0)e^{i\beta_0 z}, \tag{4.9}$$

where $\tilde{A}(z,\omega)$ is the Fourier transform of the slowly varying pulse envelope and β_0 is to be determined later. Plugging Eq.4.9 into Eq.4.8 and applying separation of variables with eigenvalues arbitrarily labelled as $-\tilde{\beta}^2 F$ gives the following two governing equations

$$\begin{aligned} \frac{\partial^2 F}{\partial x^2} + \frac{\partial^2 F}{\partial y^2} + F(\epsilon k_0^2 - \tilde{\beta}^2) = 0, \\ 2i\beta_0 \frac{\partial \tilde{A}}{\partial z} + (\tilde{\beta}^2 - \beta_0^2)\tilde{A} = 0. \end{aligned} \tag{4.10}$$

Here we have assumed the second derivative $\frac{\partial^2 \tilde{A}}{\partial z^2}$ is negligible as $\tilde{A}$ is a slowly varying function of z. The first equation is solvable by considering the nonlinear refraction as a small perturbation to the linear coefficient. In doing so, we can obtain $F(x,y)$ and the corresponding propagation constant $\tilde{\beta}$. We do not solve this here but in summary, the effect on the propagation is to perturb the linear propagation constant by an amount $\Delta\beta(\omega)$ found to be[86]:

$$\begin{aligned} \tilde{\beta}(\omega) &= \beta(\omega) + \Delta\beta(\omega), \\ &= \frac{n_1 \omega}{c} + \gamma(\omega)|\mathrm{A}|^2. \end{aligned} \tag{4.11}$$

The second equation describes how the pulse envelope will vary along z. The characteristic dispersion length, defined in Ref.[86] as $L_D = \Delta\tau^2/|\beta_2|$, is approximately 6.7 m in our Cornerstone devices where $\Delta\tau$ is the pulse width and β_2 is the dispersion parameter. We can therefore consider $\tilde{\beta}(\omega) \approx \tilde{\beta}(\omega_0)$ to be a good approximation across the pulse for typical integrated waveguide lengths of ~ cm. It then follows that $\tilde{\beta}(\omega)^2 - \beta_0^2 \approx 2\beta_0 \Delta\beta_0$. Using this approximation and taking the inverse Fourier transform of the second equation gives:

$$\begin{aligned} \frac{\partial A}{\partial z} &= i\Delta\beta_0 A \\ &= i\gamma(\omega_0)|A|^2 A. \end{aligned} \tag{4.12}$$

From this equation we see that as the pulse propagates along z, a phase is applied to the slow varying pulse envelope proportional to the instantaneous power at z. Figure 4.1(a) shows how a typical sech-squared pulse envelope accumulates phase after propagating a distance L along z. The spectrum of the pulse becomes broadened due to the additional length-dependent phase acquired by each point on the envelope, Fig. 4.1(b). It is important to note that the pulse envelope in time remains unchanged but is no longer transform-limited. By reintroducing the carrier oscillations, Fig. 4.1(c), we can see the effect of this additional phase on the carrier frequency which acquires a chirp dependent on the rate of change of the envelope intensity, Fig. 4.1(d).

4.1.4 Self-phase modulation in a Kerr interferometer

Shirasaki and Haus first suggested placing Kerr mediums inside interferometers to combine the effect of SPM and interference to give a nonlinear power response[165]. We will see later in the discussion that this nonlinear behavior can lead to a reduction in both classical and quantum noise. For the purpose of this thesis, we will limit our discussion to a Sagnac interferometer configuration and we refer the reader to Ref.[166] for an in depth discussion on Sagnac interferometry. Below is a schematic of the exact interferometer we employ.

The interferometer consists of an integrated tunable beamsplitter, with transmission η, and a spiral of length L in which the pulse will acquire SPM dependent on the power in each arm. In chapter 2 we state the transfer matrix of an integrated tuneable beamsplitter with transmission η, dependent on the phase, θ, applied by a heating element above the waveguide. To analyse the power relation of this device, let us input a single-mode plain wave into port 1 such that $E_1 = E_{\text{in}} e^{i\phi}$ and $E_2 = 0$. We may assume $\phi = 0$ and $E_{\text{in}} \in \mathbb{R}$ without loss of generality and the input power, P_{in} is then given by $P_{\text{in}} = E_{\text{in}}^2$. Using the beamsplitter transfer matrix and Eq.4.3 for acquired SPM, the output power of each port is found to be:

$$\begin{aligned} P_1 &= 2\eta(1-\eta)P_{\text{in}}\Big(\cos\left(\gamma L P_{\text{in}}(1-2\eta)\right)+1\Big) \\ P_2 &= P_{\text{in}} - P_1 \end{aligned} \tag{4.13}$$

In this ideal model with $\eta = 0.9$, step-like behavior occurs in the output power of each port that is dependent on the relative phase acquired between the two arms, as seen in Fig. 4.2. The relative phase is driven by unequal SPM in each arm and is thus power dependent. By observation of Eq.4.13 we see that as the interferometer approaches a symmetric configuration with $\eta = 0.5$, the steps become more pronounced via the factor $\eta(1-\eta)$ but, at the same time, their period approaches infinite through $(1-2\eta)$ meaning more power is needed to reach multiple steps. In reality, visibility of this behavior is degraded by poor interference in the beamsplitter. We can witness the effect by either varying P_{in} with constant splitting ratio or varying splitting with constant power. Witnessing step-like behavior in the output power is a hallmark of nonlinearity and is a strong sign that the device can be utilised to suppress or amplify intensity noise in the input state.

To understand how noise suppression might result from a nonlinear power response, let us consider that we artificially add noise to a constant power signal by applying a weak intensity modulation about 7.5 mW, depicted in Fig.4.2 by

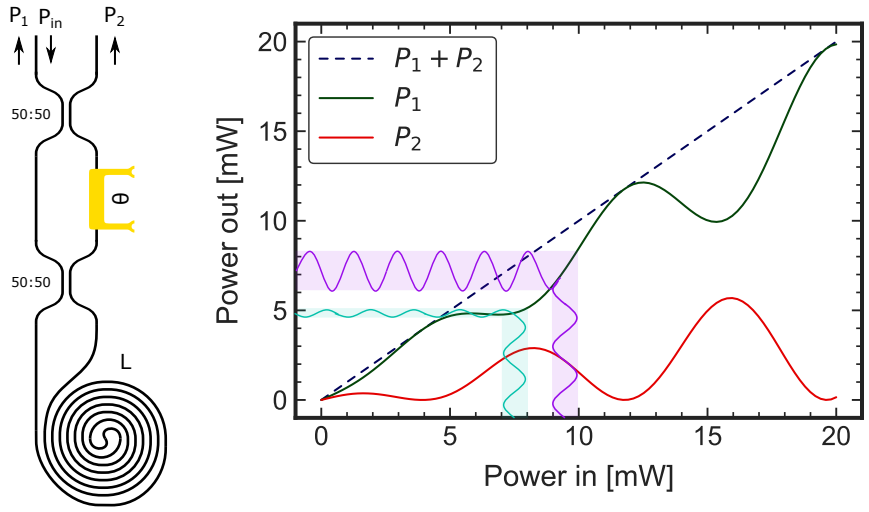

FIGURE 4.2. A schematic of an integrated Sagnac Kerr interferometer. The graph plots the power relations for each port assuming a fixed beamsplitter transmission of $\eta = 0.9$. The purple and green lines show how input power modulation depths are altered by the nonlinearity.

the turquoise oscillation. At this point the power relation for P_2 is close to a turning point meaning comparatively large variations in input power are mapped to smaller variations in the output power. In effect, the modulation depth will decrease. Conversely, driving the same modulation about 9.5 mW will target a steeper part of the curve resulting in a greater modulation depth in the output. It is important to recognise that in the purely classical case, linear loss would also have this effect on the modulation, however, the RIN of the state, defined as the ratio of average power in the modulation to average total power, would remain constant as both are equally effected by loss. In a Kerr interferometer, this is not the case and a reduction in RIN is possible.

We can consider both classical and quantum intensity noise to be the sum of small random modulations occurring simultaneously at a variety of sideband frequencies[80]. The picture given above for a singular modulation frequency also holds true for broadband noise due to the linear nature of an interferometer. Noise suppression is greatest when driving close to the turning point of the power relation curve. The toy model analysed above assumes perfect interference at the beamsplitter and neglects the effect of other processes that will occur concurrently that negatively effect interference, such as spectral broadening from self-phase modulation, which must be considered when analysing noise reduction in a pulse.

Schmitt *et al.* showed that the nonlinear response is a necessary but not suffi-

cient condition for the device to suppress quantum noise in the state due to parasitic losses in the device degrading any squeezing that results from the nonlinearity[167]. The initial scheme presented by Shirasaki and Haus in 1989[165] used optical fiber as a Kerr medium. In their scheme, a pulse is split via a 50:50 beamsplitter and each arm propagates through identical Kerr mediums to acquire squeezing and matched linear phase. The two arms are then combined again on a second 50:50 splitter mapping the pulse to one output and squeezed vacuum to the other. The scheme was considered a breakthrough in that the broadband nature of the squeezing, limited only by the characteristic response time of the beamsplitters, enabled the use of pulsed light which has a higher average power than CW light resulting in a stronger nonlinear effect[152]. The scheme was later adapted to produce bright squeezing and was demonstrated in fiber for the first time in 1998[167]. In this adapted scheme, the 50:50 beamsplitters are changed for 90:10 beamsplitters. Bright amplitude squeezing then arise from the combination of SPM in the bright arm followed by a slight rotation of the squeezed quadrature, via interference with the weak arm, to bring it inline with the amplitude quadrature.

In order to fully understand these quantum noise suppression schemes, we must discuss a quantum analysis of self-phase modulation, first acting on a coherent state, and later on a pulse propagating through an interferometer.

4.1.5 Quantum analysis of self-phase modulation

In the quantum regime, one can derive the (non-Gaussian) generator of SPM via full quantisation of the field as shown by[168]. Assuming a lossless Kerr medium that displays an isotropic response and which is guiding a single circularly-polarised mode, the unitary Kerr operator for that mode is found to be[168]:

$$\hat{U}_{\mathrm{K}} = e^{i\gamma\hbar\omega z\hat{n}(\hat{n}+1)}. \tag{4.14}$$

It is intuitive to consider Kerr evolution of a coherent state $|\psi\rangle_{\mathrm{K}} = \hat{U}_{\mathrm{K}}|\alpha\rangle$. The resulting state, $|\psi\rangle_{\mathrm{K}}$, is known as a Kerr state and is expressed here in the Fock basis[50]:

$$|\psi\rangle_{\mathrm{K}} = e^{-(1/2)|\alpha|^2} \sum_{n=0}^{\infty} \frac{\alpha^n e^{-i\gamma\hbar\omega z n(n+1)}}{\sqrt{n!}} |n\rangle. \tag{4.15}$$

Under Kerr propagation, a relative phase is applied to each basis state dependent on the number of photons present. This can be thought of as an amplitude dependent phase, which agrees with our classical interpretation of Kerr evolution. If we now consider an arbitrary quadrature measurement $\hat{q}_\phi = \hat{a}e^{-i\phi} + \hat{a}^\dagger e^{i\phi}$ and calculate the variance, Eq.4.16, we find that for certain values of ϕ, the state displays

sub-classical variance and is therefore already quadrature squeezed without the use of an interferometer[168]. We can plot the evolution of the quantum noise in phase space via the Wigner representation of the quasi-probability distribution, Fig.4.3 (see Sec. 2.1.1.3). A radially proportional phase is applied as the state propagates resulting in a smeared banana shaped distribution. We can see in the graph that the radial extent of the state remains unchanged, or equivalently – the Kerr operator commutes with the photon number operator leaving the photon number statistics Poissonian. It is for this reason that Kerr evolution alone cannot provide photon number squeezing (or equivalently amplitude squeezing in the high power limit).

$$\mathrm{Var}(\hat{q}_\phi) = 2\mathrm{Re}\{\langle \Delta \hat{a}^2 \rangle e^{-2i\phi}\} + 2(\langle \hat{a}^\dagger \hat{a} \rangle - |\langle \hat{a} \rangle|^2) + 1 \tag{4.16}$$

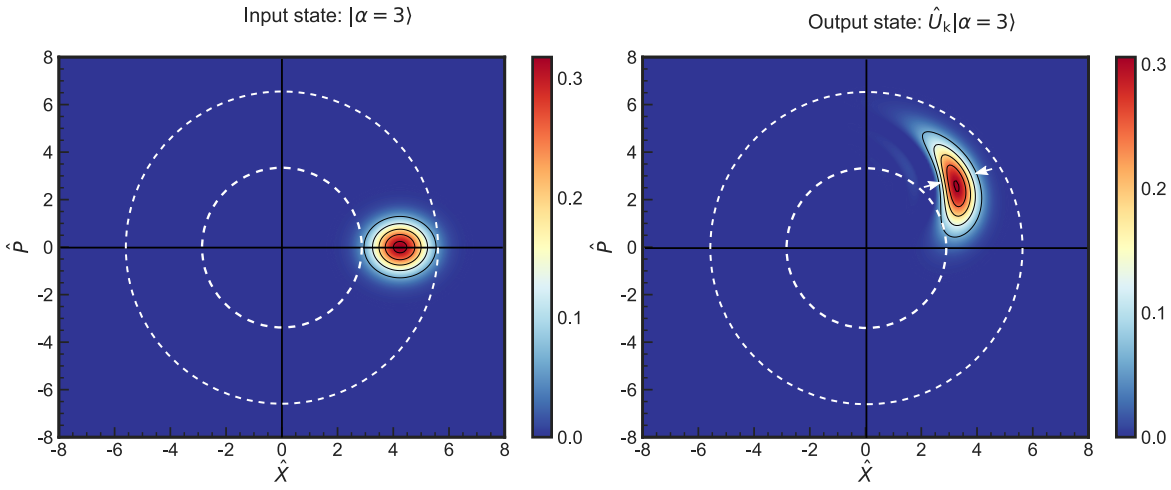

FIGURE 4.3. The Wigner representation of a coherent state with $\alpha = 3$ before and after Kerr evolution. This graph was created using QuTip quantum systems modelling software[169].

4.1.6 Quantum evolution of a pulse through a Kerr interferometer

We will combined the theory presented in the previous sections to model noise reduction in a shot-noise limited pulse propagating through an asymmetric Kerr interferometer. We follow the method presented in Ref.[152,153], which utilises linearisation of the field as presented in Sec. 2.1.4, but tailored for optimal computation of a 2.07 µm high-power pulse laser propagating through the Cornerstone

devices. See Appendix B for a detailed list of pulsed laser and Cornerstone devices specifications used in this chapter.

The pulsed laser, to a good approximation, outputs a transform-limited sech-squared pulse envelope which we discritise into M, equally spaced, modes in time separated by $\Delta\tau$, labelled j. These modes are considered orthogonal and centred on the co-moving time frame of the laser pulse such that $\tau = t - z/v_g$ where v_g is the group velocity of the pulse in the waveguide (defined at the peak wavelength). This approximation is valid only when a frequency independent group velocity adequately captures the evolution of the envelope across its full bandwidth. Each mode j is linearised into a time-independent classical field amplitude, $A(z)_j$, plus a continuum of small quantum noise operators $\hat{a}_j(z,t)$ which obeys the following commutation relations:

$$\begin{aligned}[\hat{a}_j(z,\tau), \hat{a}_j^\dagger(z,\tau')] &= \delta(\tau-\tau'),\\ [\hat{a}_j(z,\tau), \hat{a}_j(z,\tau)] &= 0,\end{aligned} \tag{4.17}$$

as per standard linearisation, presented in chapter 2 and depicted in Fig. 4.4(a) for a the pulse.

We further discritise each continuum of quantum noise operators into the set of M time modes. This is achieved by representing each continuum as a linear combination across the temporal modes j such that $\hat{a}_j(z,t) \equiv \frac{1}{\sqrt{M}}\sum_{k=1}^{M}\left(\mu(z)_j^k \hat{b}_k + \nu(z)_j^k \hat{b}_k^\dagger\right)$, where $\hat{b}_k$ are now time-independent quantum noise operators which obey:

$$\begin{aligned}[\hat{b}_i, \hat{b}_j^\dagger] &= \delta_{ij},\\ [\hat{b}_i, \hat{b}_j] &= 0,\end{aligned} \tag{4.18}$$

for all i, j in the set $\{1,...,M\}$. Here, $\mu(z)_j^k$ and $\nu(z)_j^k$ are matrix elements in $\mathbb{C}^{M\text{x}M}$ which, together with $A(z)_j$, fully capture the dynamics of the system. The normalisation factor is required to recover the correct commutation relations for $\hat{a}_j(z,t)$.

The decomposition of the j-th temporal mode of the pulse, $A(z)_j + \hat{a}_j(z,t)$, is depicted in Fig. 4.4(b) in the sideband picture. In converting to the sideband picture, we take the discrete Fourier transform of $A(z)_j + \frac{1}{\sqrt{M}}\sum_{k=1}^{M}\left(\mu(z)_j^k \hat{b}_k + \nu(z)_j^k \hat{b}_k^\dagger\right)$ and plot the resulting state as a combination of electric field modes across frequency. Note that we remain in the rotating frame of the carrier and thus apply the relevant translation to the axises. The classical contribution gives a DC component at the carrier frequency $\delta(\omega_0)A(z)_j$. The discrete Fourier transform of the quantum noise results in pairs of sideband modes symmetrically placed about

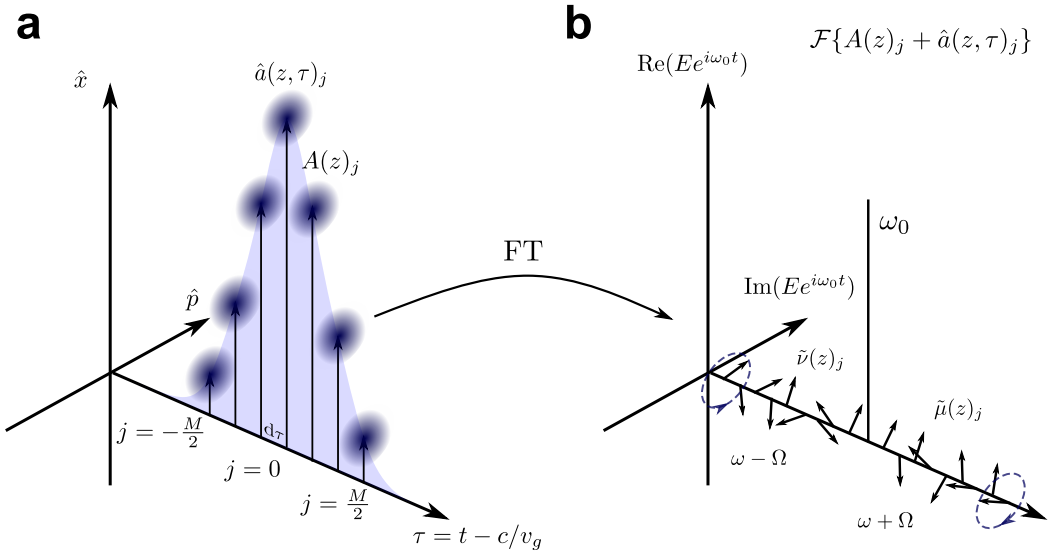

FIGURE 4.4. (a) a schematic showing pulse discretisation and linearisation as performed in the quantum pulsed Kerr propagation model. Each slice has a static classical contribution and a time dependent quantum noise contribution depicted in phase space via the shaded circles. (b) the equivalent sideband model of a single pulse slice which has been discretised further into complex field vectors in sideband modes symmetric about the DC carrier which oscillate in time. The magnitude of these vectors is determined by the vacuum noise level.

DC. All sidebands has a fixed vector of equal magnitude but random phase that reflects the Gaussian nature of the quantum noise in the time domain. As we will see, partial correlation of these random phases across a given sideband, through the action of SPM, gives rise to Piossonian noise statistics in that sideband.

At $z = 0$, the laser is assumed to be shot-noise limited and thus the photon number variance of each temporal mode is exactly $\left|A(0)_j\right|^2$. This dictates that $\nu(0) = 0_M$ and $\mu(0) = I_M$, where 0_M and I_M are the zero and unit matrices of dimension M^2. Putting this all together we get:

$$\hat{A}(z,t) = \sum_{k,j=1}^{M} \left(A(z)_j + \frac{1}{\sqrt{M}} \left(\mu(z)_j^k \hat{b}_k + \nu(z)_j^k \hat{b}_k^\dagger \right) \right) \tag{4.19}$$

We adapt Eq.4.12 for the evolution of a pulse envelope to include linear propagation loss along the length of the waveguide:

$$\frac{\partial \hat{A}(z,t)}{\partial z} = \left(i\gamma |\hat{A}(z,t)|^2 - \frac{\alpha}{2} \right) \hat{A}(z,t). \tag{4.20}$$

It is important to note that including propagation loss in this way only classically accounts for the effect of loss. As noise is suppressed below the shot-noise limit,

loss will couple in vacuum noise and counter the noise suppression. As an upper bound on the achievable noise suppression, we apply classical loss to the amplitude of the envelope but not the quantum statistics. Full analysis of the lossy case is covered in Ref. [153].

We can substitute Eq.4.19 into this governing differential to give equations of motion for μ_j, ν_j and A_j:

$$\begin{aligned}
\frac{\partial A(z)_j}{\partial z} &= \left(i\gamma|A_j|^2 - \frac{\alpha}{2}\right)A(z)_j, \\
\frac{\partial \mu(z)_j^k}{\partial z} &= 2i\gamma|A(z)_j|^2\mu(z)_j^k + i\gamma A(z)_j^2\nu(z)_j^{k*}, \\
\frac{\partial \nu(z)_j^k}{\partial z} &= 2i\gamma|A(z)_j|^2\nu(z)_j^k + i\gamma A(z)_j^{k2}\mu(z)_j^{k*}.
\end{aligned} \tag{4.21}$$

To solve these equations numerically, we discritise z into $n = 1...N$ steps equally spaced by Δz. Each $A(n+1)_j$ is solved for using the first equation via $A(n+1)_j = \exp\left((i\gamma\left|A(n)_j\right|^2 - \alpha/2)\Delta z\right)A(n)_j$. This is then fed into the coupled first order differentials, along with $\mu(n)_j^k$ and $\nu(n)_j^k$, to solve for $\mu(n+1)_j^k$ and $\nu(n+1)_j^k$. As we have found dispersion to be negligible, both $\mu(z)$ and $\nu(z)$ will remain diagonal with zero off-diagonal elements. Making use of this fact allows us to simplify the numerical computation and reduce the calculation time.

As depicted in Fig. 4.2, the input pulse first propagates through a beamsplitter. Using the transfer matrix for an integrated beamsplitter, we map the input pulse $\hat{A}(0,0)$ into two modes inside the interferometer labelled $\hat{A}_c(0,0)$ for clockwise propagation and $\hat{A}_{ac}(0,0)$ for anticlockwise propagation. Each mode is then propagated through the same length of Kerr waveguide using the numerical approach outlined above. The beamsplitter transfer matrix is then applied to the two modulated states such that we get the following two outputs:

$$\begin{aligned}
\hat{A}_1 &= \sqrt{\eta}\,\hat{A}_c(N) + i\sqrt{1-\eta}\,\hat{A}_{ac}(N), \\
\hat{A}_2 &= i\sqrt{1-\eta}\,\hat{A}_c(N) + i\sqrt{\eta}\,\hat{A}_{ac}(N),
\end{aligned} \tag{4.22}$$

in which

$$\begin{aligned}
\hat{A}_c(N) &= \sum_{k,j=1}^{M}\left(A(N)_{c,j} + \frac{\delta}{\sqrt{M}}\left(\mu(N)_{c,j}^k\hat{b}_{c,k} + \nu(N)_{c,j}^k\hat{b}_{c,k}^\dagger\right)\right), \\
\hat{A}_{ac}(N) &= \sum_{k,j=1}^{M}\left(A(N)_{ac,j} + \frac{\delta}{\sqrt{M}}\left(\mu(N)_{ac,j}^k\hat{b}_{ac,k} + \nu(N)_{ac,j}^k\hat{b}_{ac,k}^\dagger\right)\right).
\end{aligned} \tag{4.23}$$

We are interested in calculating the resulting PSD of the photocurrent generated via detection of the brighter state with a photodiode, $\hat{I}_1 = \hat{A}_1^\dagger\hat{A}_1$. Comparing

this to the current generated by a shot-noise limited state of equal power will inform us as to how much noise reduction has occurred. The PSD generated by a photodiode at low frequencies compared to the width of the pulse can be approximated via the DC component of Wiener–Khintchine's theorem, given by[152]:

$$\Phi = \frac{1}{2M^2} \sum_{j,k=1}^{M} \langle \hat{A}_{1,j} \hat{A}_{1,k}, \rangle \tag{4.24}$$

where the expectation is taken over the vacuum as we have assumed the laser to be shot-noise limited. Note that the summation indices j and k represent a discrete autocorrelation. The noise reduction factor is then found by comparing this value to the shot-noise limited case in which $\mu(N)_c = \mu(N)_c = I_M$ and $\nu(N)_c = \nu(N)_c = 0_M$.

In this model, care in needed in choosing M, N, Δz and Δt such that the pulse is well sampled. Δz must be an order of magnitude less than the characteristic nonlinear length of the waveguide given by $L_{\mathrm{NL}} = R_r \Delta\tau / \gamma P_{\mathrm{in}}$ where $\Delta\tau$ is the pulse width in the time domain. We calculate $L_{\mathrm{NL}} = 3\,\mathrm{mm}$ for our Cornerstone devices, therefore, Δz is chosen to be $1\,\mu\mathrm{m}$. The product $M\Delta t$ must be sufficient to cover the full width of the pulse post-broadening. Convergence analysis over all simulation parameters was carried out to ensure a stable and accurate solution. M was chosen to be $M = 2^{11}$ and $\Delta t = 0.013\,\mathrm{ps}$ such that $M\Delta t = 10\Delta\tau$.

The second axis in Fig. 4.5 below plots the expected power relation from a Cornerstone device with spiral length 5.5 cm. We have accounted for $-3\,\mathrm{dB/cm}$ propagation loss and $-5\,\mathrm{dB}$ of grating loss as measured for this device. γ is estimated to be approximately 220 1/Wm using the current best estimate of $n_2 = 1.5\mathrm{x}10^{-18}$ m^2/W in silicon at $2\,\mu\mathrm{m}$[65].

The first axis in Fig. 4.5 shows the associated expected noise reduction with the greatest reduction of $-1.8\,\mathrm{dB}$ occurring at the turning point of the first step. Schmitt *et al.* proved that optimal suppression occurs at 92 : 8 splitting ratio where the two turning points form a saddle point. Divergence away from this point gives two more steep, but less deep, noise suppression minima[167]. This unintuitive behavior stems from the banana-shaped distribution that occurs in SPM. The maximum squeezing ratio is mainly limited by the pulse shape with greater squeezing as the pulse approaches a square shape. This is because at speeds less than the repetition rate of the laser, the measured squeezing is in fact a weighted average of instantaneous squeezing over the high-power section of the pulse and the low-power section between, and on the wings of, the pulse. We also note that this model does not account for additional noise sources that may be present inside the waveguide such as thermo-refractive noise[170].

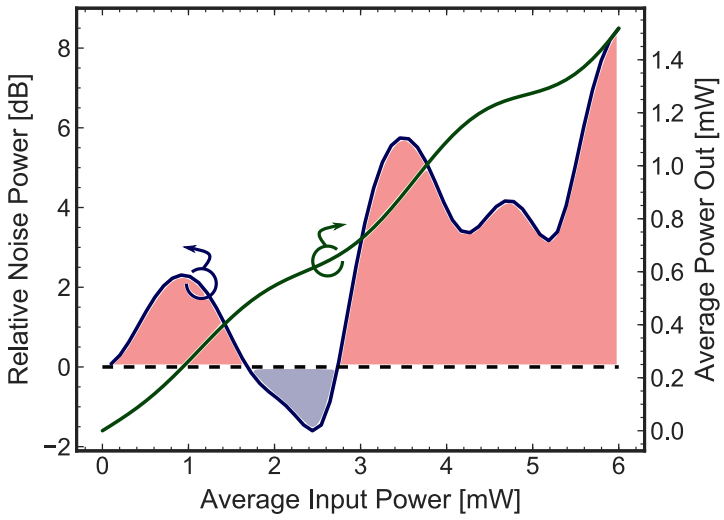

FIGURE 4.5. The power in – power out relations for a Cornerstone 1 device with spiral length 5.5 cm. Propagation loss is −3 dB/cm, chip coupling losses are −5 dB and detector efficiency is assumed to be unity (green). γ is estimated to be approximately 220 1/Wm[36]. Expected relative noise power from the device (blue) compared to the shot-noise limit (dashed blue). Shaded blue regions are regions of expected noise suppression and shaded red are regions of noise amplification.

4.1.7 Accounting for excess classical noise

We have seen how we can use an asymmetric Kerr interferometer to suppress quantum noise in a pulse train below the shot-noise limit. Unfortunately, the only pulsed laser available at 2 µm is far from shot-noise limited (see Sec. 3.7). We must therefore adapt this model to account for classical noise instead of quantum noise. We make the reasonable assumption that the classical noise is Gaussian in phase and amplitude. Adapting the model is straightforward in in a linearised model by replacing the continuum quantum noise operators $\hat{a}(z,t)_j$, which previously had a fixed variance of exactly 1 (defined by the shot-noise of a coherent state), with classical stochastic functions $s_j(z,t)$ that now have an allowed variance greater than 1 and which obey:

$$\begin{aligned} \langle s_j(z,t)s_j(z,\tau)\rangle &= \delta(t-\tau), \\ \langle s_j(z,t)s_j^*(z,\tau)\rangle &= \langle s_j(z,t)\rangle\langle s_j^*(z,\tau)\rangle = 0, \end{aligned} \tag{4.25}$$

the classical equivalent to the commutation relations presented in Eq. 4.17. These relations state that the noise on each time mode is independent across time and uncorrelated across orthogonal quadratures.

Taking the same approach as before, we discritise these into time-independent modes; we employ $\mu(z)^k_j \zeta_k$ and $\nu(z)^k_j \zeta^*_k$, where ζ_k and ζ^*_k are orthogonal stochastic functions that account for the contribution of each discrete pair of symmetric sidebands to the motion of $s_j(z,t)$. By definition, each stochastic function has zero expectation, $\langle \zeta_j \rangle = 0$ and $\langle \zeta^*_j \rangle = 0$, and is independent across all modes, $\langle \zeta_j \zeta_k \rangle = \delta_{jk}$. As previously stated, define these classical fluctuations to have Gaussian statistics such that $\langle \zeta^2_j \rangle = 1$, $\langle \zeta^{*2}_j \rangle = 1$ and $\langle \zeta_j \zeta^*_j \rangle = 0$, with vanishing higher-order moments. Figure 4.6(a) depicts how a single time mode j is broken down into a large stationary vector and a linear combination of two orthogonal stochastic functions in phase space. The input pulse is then given by:

$$A(z,t) = \sum_{k,j=1}^{M} \left(A(z)_j + \frac{\delta}{\sqrt{M}} \left(\mu(z)^k_j \zeta_k + \nu(z)^k_j \zeta^*_k \right) \right), \tag{4.26}$$

with initial conditions $\nu(0) = \mu(0) = I_M \sigma / \sqrt{2}$, where σ is a constant that defines the level of noise above the vacuum in each sideband. This initial condition ensures the quadrature variance of each time mode is exactly σ times that of the vacuum. Here, we model a quadrature noise level 20 dB greater than vacuum.

Using the same method as in the quantum case and utilising the identities listed above when taking the expectation value in Eq.4.24 to cancel terms, we can plot the expected noise suppression in relation to the input noise variance σ.

In Fig. 4.6(b) we see noise is suppressed in line with the change in gradient in the average output power as expected. In the classical case, the double dip phenomena mentioned previously is more pronounced with maximal noise suppression expected to be around -15 dB. This sets the upper limit on what we should expect to measure from a Cornerstone device due to expected degradation of the effect from imperfect interferometer visibility. We also note that as noise is suppressed close to the shot-noise limit, the error in this purely classical model will grow due to the absence of quantum noise in the model. The power of a linearised model is that both the classical and quantum noise could be combined into the same model to give a complete picture.

4.2 Optimal design of an integrated Kerr interferometer

2 µm integrated optics components in silicon have been pioneered by Rosenfeld who spent his PhD designing key components, such as single mode waveguides,

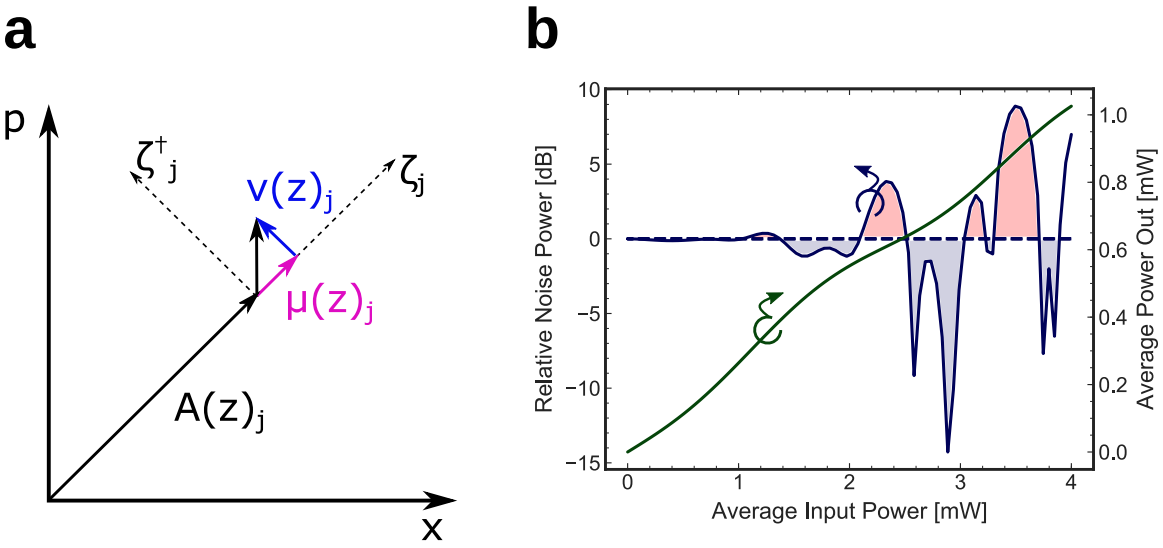

FIGURE 4.6. (a) schematic of classical quadrature noise brokendown into two orthognal stocastic function. (b) the power in – power out relations for a Cornerstone 1 device with spiral length 5.5 cm. Propagation loss is −3 dB/cm and chip coupling losses are −5 dB (green). γ is estimated to be approximately 220 1/Wm. The expected relative noise power from the device (blue) compared to the input noise level (dashed blue). Shaded blue regions are regions of expected noise suppression and shaded red are regions of noise amplification.

gratings, evanescent couplers and integrated beamsplitters, for single photon source development[36]. Allen *et al.*, in collaboration with Rosenfeld, utilised this arsenal of optimised passive components to build a Sagnac interferometer. Below, we outline the key design considerations in designing such a device for noise suppression of a pulsed laser.

One key benefit to performing this scheme in integrated optics, compared to traditional fiber optics[50,171,172], is the relaxed dispersion engineering constraints afforded by low dispersion integrated waveguides. In fiber, it is crucial to maintain soliton behavior in the spiral to ensure the pulse train is not broken down. This is achieved via careful balancing of anomalous dispersion and self-phase modulation[173], thereby placing additional constraints on fiber engineering.

340 x 500 nm single-mode strip waveguides, designed by Rosenfeld for Cornerstone have $\beta_2 = -1.2\ \text{ps}^2/\text{m}$ at 2.07 µm. Figure 4.3 below shows the pulse spectrum obtained via an optical spectrum analyser. The spectral width of the pulse is 2.65 nm. We can estimate the amount of pulse spreading expected due to dispersion via $\Delta\tau \approx DL\Delta\lambda$ where L is the length of the spiral and D is the group

velocity dispersion parameter given by $D = -2\pi c\beta_2/\lambda^2$. Using these values we get $D = 5.28\text{x}10^{-4}$ s/m^2 and $\Delta\tau$ =0.08 ps for a spiral of length 6 cm. Since the temporal width of the pulse has been measured by the manufacture to be 2.8 ps, we can consider this pulse broadening to be negligible. Note that this remains true for a broad range of waveguide widths, Fig. 4.7(inset), giving us the freedom to focus the optimisation of waveguide width and spiral length on the nonlinear coefficient of the waveguide, the acquired SPM, and expected propagation loss.

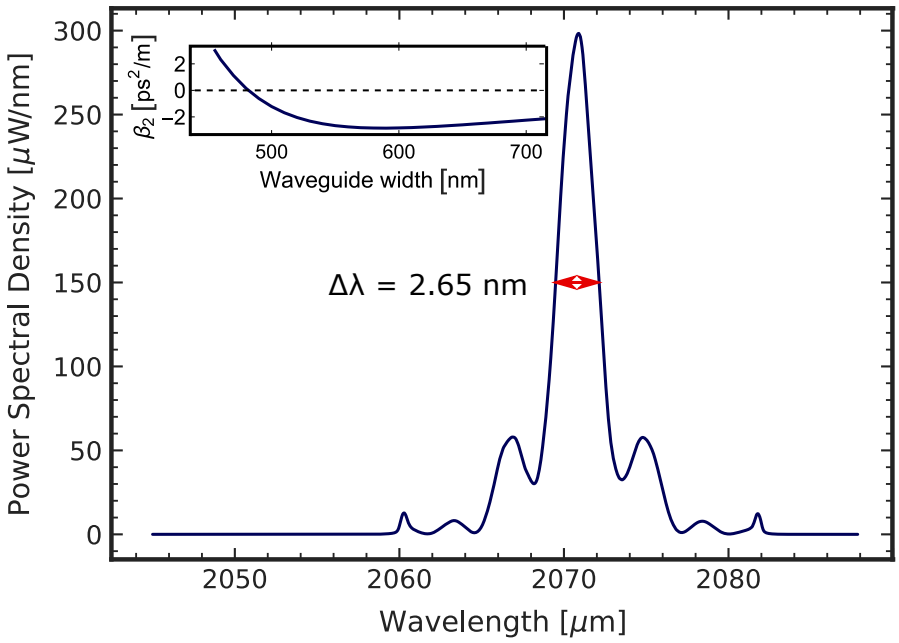

FIGURE 4.7. Raw pulsed laser spectrum displaying a FWHM of 2.65 nm. The inset shows dispersion as a function of waveguide width for Cornerstone technology[65].

Propagation loss from waveguide sidewall roughness is notoriously difficult to model due to the stochastic nature of the variations. Nonetheless, Payne and Lacey have devised a proven model which estimates propagation loss due to sidewall roughness[88,174] via an idealised autocorrelation function which describes the sidewall variation profile. Here, we use this model to estimate the expected sidewall roughness induced propagation loss of strip waveguides of varying width. Hagan found that an autocorrelation with an exponential form produced results that agree well with measured values for waveguides fabricated via optical lithography[174]. The function is defined as follows:

$$R(u) = \sigma^2 e^{-\frac{|u|}{Lc}}, \tag{4.27}$$

where L_c is the sidewall roughness correlation length, typically measured via scanning-electron microscopy, σ is the mean squared standard deviation of the sidewall roughness and u is distance along the waveguide. These are approximated to be 100 nm and 1 nm respectively for Cornerstone devices. Let us assume the waveguide cross-sectional profile is centred on $(x, y) = (0, h/2)$, with width w such that the sidewalls are located at $x = \pm w/2$ and height h such that the bottom of the waveguide is at $y = 0$. The closed form expression for the propagation loss in dB/m is given by Ref.[88] to be:

$$\alpha(w)_L = 4.343 E(w/2)^2 (n_{\text{core}}^2 - n_{\text{clad}}^2)^2 \frac{k_0^3}{4\pi n_{\text{clad}}} \int_0^{\pi} \tilde{R}(\beta - n_{\text{clad}} k \cos(\theta)) d\theta \tag{4.28}$$

where $E(w/2)$ is the normalised-integrated modal field evaluated at the waveguide edge, solved for using Lumerical. n_{clad} is the cladding index, n_{core} is the core index, β is the mode propagation constant and $\tilde{R}$ is the Fourier transform of the auto-correlation function. First we integrate the field over the height of the waveguide and then normalise across the full width of the mode to give:

$$E(w/2) = \frac{\int_0^h E(w/2, y)^2 dy}{\int_{-\infty}^{\infty} E(x)^2 dx}. \tag{4.29}$$

The integral in Eq. 4.28 has a closed form solution presented in[63] which allows for an analytical solution.

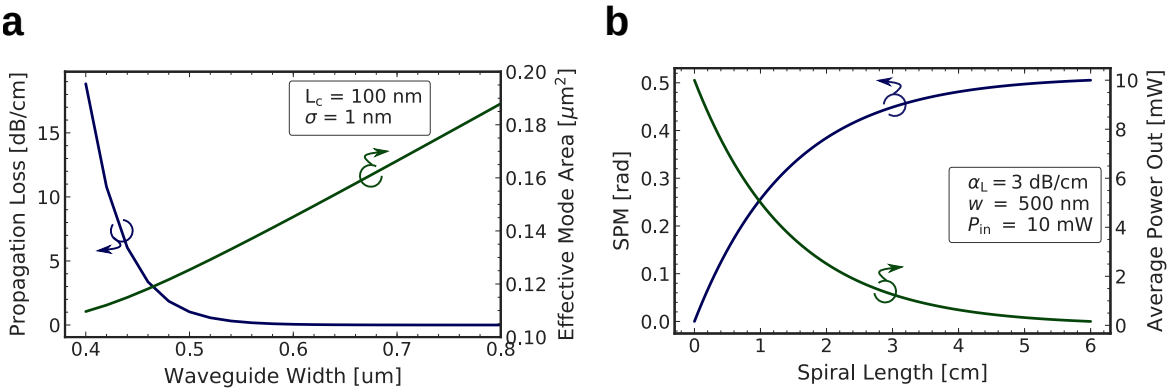

FIGURE 4.8. a) estimated propagation loss and modal area in Cornerstone as a function of waveguide widtha and (b) expected SPM and output power assuming a waveguide width of 500 nm, propagation loss of −3 dB and input average power of 10 mW

As waveguide width is increased, propagation loss falls of exponentially due to an exponential drop in the power concentrated at the sidewalls of the strip. Figure 4.8(a) shows that increasing the width much beyond 0.5 µm has little effect

on the loss and decreases the nonlinear coefficient of the waveguide through increasing mode area. Above 0.561 µm, the waveguide becomes multi-mode which is best avoided, especially in the corners of the spiral where mode-mixing is likely to occur. Based on these simulations, the optimal waveguide width is likely to be close to 0.5 µm.

We can account for the effect of propagation loss via an effective spiral length scaling, a common approximation described in Ref.[86], which scales the length of the waveguide to one that has no loss but which gives the same amount of acquired SPM. Using effective length, Eq. 4.3 is adapted to:

$$\phi_{\mathrm{NL}} = \frac{k n_2 |P_{\mathrm{in}}|^2}{A} \frac{1 - e^{-\alpha L}}{\alpha}. \tag{4.30}$$

The above model of propagation loss does not account for bend loss. As such, we base our estimate of loss on measurements carried out by Rosenfeld and assume $\alpha_L = -3$ dB[65]. Inserting this estimate into Eq. 4.30, we plot the expected SPM as a function of spiral length, Fig. 4.8(a). SPM plateaus due to the effect of waveguide loss. Nonetheless, 0.5 rad acquired by the peak of the pulse is sufficient to see step-like behavior and noise suppression, Fig. 4.5.

4.3 Device characterisation

Before measuring noise suppression from our integrated devices, we first characterise their linear and nonlinear performance. Unless stated otherwise, all characterisation was performed with the pulsed laser. Light is coupled into each test structure at a vertical angle of 12° via VGA consisting of 8 SMF28 fiber ports with 127 µm pitch. Coupling is optimised across all 6 alignment axis.

To characterise the linear propagation loss in the waveguides, along with the grating coupler loss, we use a range of spiral waveguides of increasing length, known as a waveguide cutback (see Fig. 4.9(c)). By plotting the total waveguide length against the transmission for a fixed input power and fitting this data to a linear fit, we can extract the loss per centimeter, given by the gradient. The intercept will be equal to twice the grating coupling loss.

Using this method we characterise a propagation loss of −3.08 dB/cm with a grating loss of −5.85 dB per grating, Fig. 4.9(a). Each spiral contains 54 90° bends with bend radius 19.5 µm. The additional loss acquired in the bends is modelled to be negligible using Lumerical bend analysis. Each spiral has exactly the same number of bends meaning the additional loss will not effect the measurement

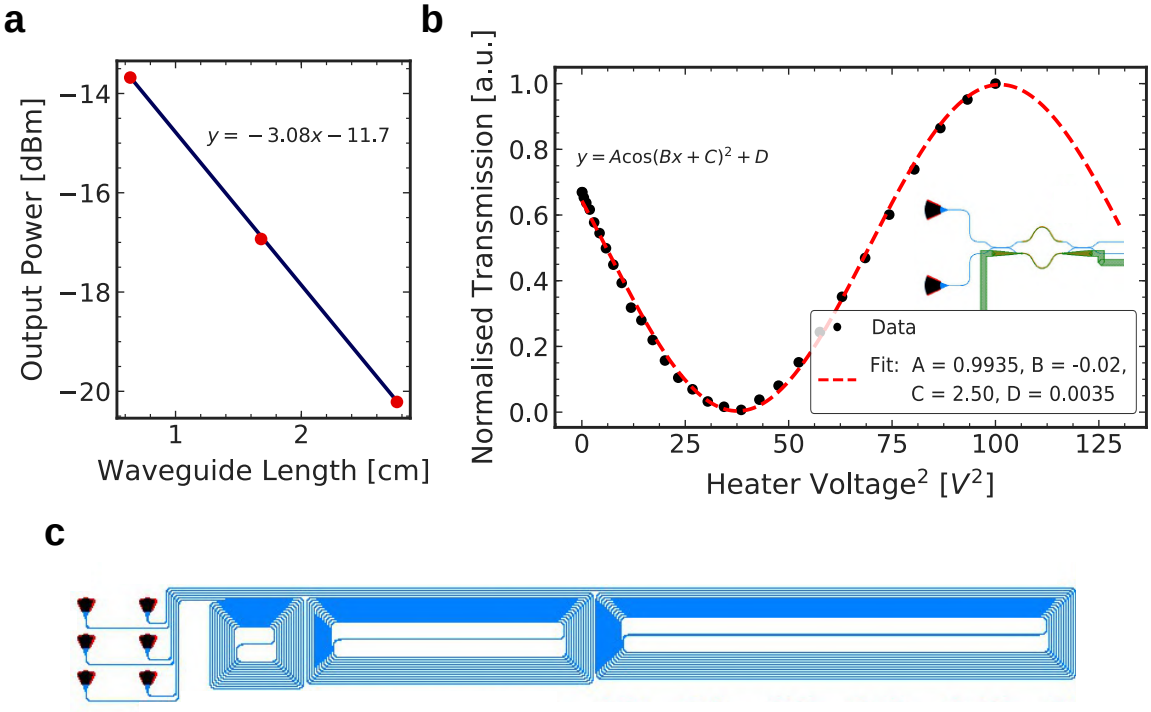

FIGURE 4.9. (a) loss as a function of spiral waveguide length, acquired using the spiral cutback depicted in (c). Data is fit to a linear function to extract propragation loss per centimeter and grating loss. (b) Sagnac dark port transmission, normalised by input power, as a function of heater voltage squared (black), fit to a $\cos^2$ function (dashed red).

of propagation loss but instead will present as a small error in our estimate of grating loss. The input pulse power was kept below 1 mW to minimise the effect of additional nonlinear losses skewing the data, resulting in an overestimate of the linear propagation loss.

In the Sagnac configuration, it is impossible to distinguish between the interference visibility of the Sagnac and the integrated MZI visibility. Access to a tap on the interior of the interferometer would remedy this. Unfortunately, there are are no MZI test structures available of the design depicted in Fig. 4.9(b). By plotting the transmission from the dark port of the Sagnac as a function of heater voltage squared, we can asses the combined visibility of the device, defined as[36]:

$$V = \frac{P_{\max} - P_{\min}}{P_{\max} + P_{\min}}. \tag{4.31}$$

Here, $P_{\max}$ and $P_{\min}$ are the maximum and minimum output powers of the device across heater voltage. Using a least-squares regression, we fit the data to $y = A\cos(Bx + C)^2 + D$ where V is then given by $V = A/(A + 2D)$. This gives a visi-

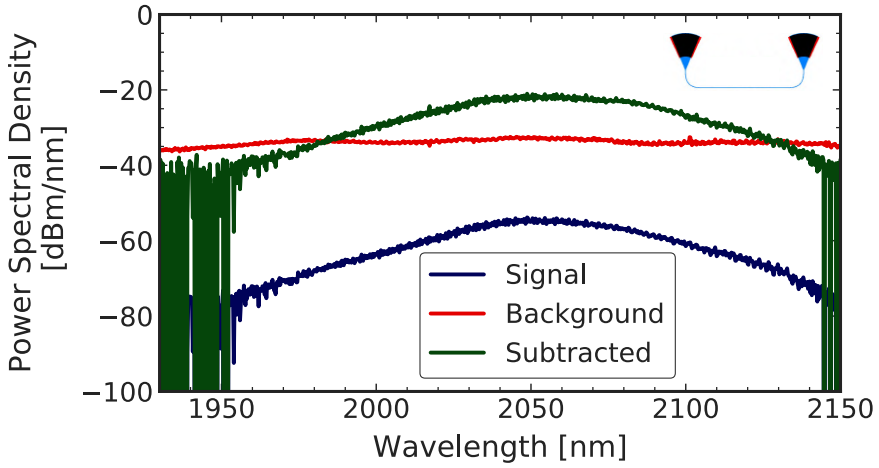

FIGURE 4.10. Grating transmission spectrum acquired via a super continuum laser and optical spectrum analyser. The plot shows the background signal from the laser (red), the grating structure output (blue) and the differenece between the two, the transmission, (green). The structure investigated is depicted in the top right corner.

bility of $V = 99.30\%$. As we increase the pulse power, we expect the visibility to decrease due to pulse broadening in the spiral beyond the working bandwidth of the integrated MZI (see chapter 2 for a discussion on integrated MZI bandwidth.)

The grating coupler bandwidth and central wavelength is characterised via the test structure shown in the top right of Fig. 4.10 with a super-continuum laser source which emits a broadband spectrum. Figure 4.10 shows the optimal wavelength is 2050 nm, 20 nm off from Rosenfeld's design target of 2070 nm. Decreasing the angle of incidence will red-shift the optimal wavelength but may also lead to an overall reduction in coupling efficiency. The bandwidth of the coupler is found to be 50 nm.

We can characterise the nonlinear losses through the spiral by measuring transmission as a function of input peak pulse power. Rosenfeld measured the nonlinear loss parameter, β_2, to be 0.5 cm/GW[36]. Transmission is related to the nonlinear loss parameter via:

$$\frac{P_{\text{out}}(x)}{P_{\text{in}}} = \frac{1}{1 + \beta_2 x P_{\text{in}}} \tag{4.32}$$

where x is distance travelled along the waveguide. Eq. 4.32 is fit to transmission data from a grating coupled 8.8 cm spiral, Fig. 4.11(a)(green), and is found to be 0.21 ± 0.04 cm/GW, resulting in higher loss than expected. For comparison, Fig.

4.11(a)(red) plots the expected relation as per Rosenfeld's measured value for Cornerstone.

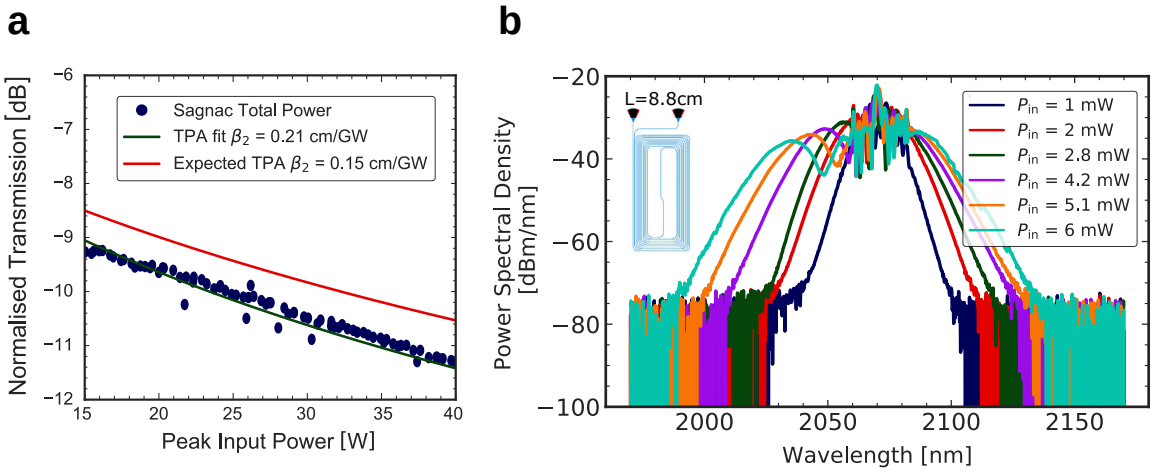

FIGURE 4.11. (a) Sprial transmission as a function of input pulse peak power (blue). The data is fit to Eq. 4.32 over the nonlinear loss coefficient β_2 (green). Expected β_2 is plotted for comparison (red). (b) Pulse spectrums from an 8.8 cm spiral for a range of input pulse powers showing spectral broadening from SPM.

As the pulse propagates through the spiral, TPA will occur alongside pulse broadening. The additional nonlinear loss measured is most likely to be the combined result of pulse broadening and grating filtering, as per the spectrum in Fig. 4.10. Rosenfeld pre-filtered the pulse in his measurement resulting in a narrower spectral width by the time the pulse exits the grating. Figure. 4.11(b) shows how the combined effects leads to an asymmetric pulse spectrum, with greater loss applied to the red side of the spectrum due to the pulse being off-center. Interestingly, this type of composite nonlinear effect has also been utilised in fiber-based experiments to produce 4.5 dB of squeezing in sub-picosecond pulsed solitons[155]. In such a scheme, a narrow-band tunable filter-function is optimal rendering the broad filter function generated by the grating sub-optimal for squeezed state production.

4.4 Measuring noise suppression

The setup used to measure noise suppression in the laser is depicted in Fig. 4.12. The laser propagates through a VOA consisting of a razor blade on a motorised stage. The light is then coupled back into SMF28 fibre. VOA insertion loss is mea-

sured to be −4.1 dB. The laser is then coupled through a 90:10 fiber beamsplitter to tap the input power. This splitter is characterised to have insertion loss −0.44 dB and splitting ratio 88.7:11.3. The 11.3% output is incident on a power meter and is used to monitor the input power. The 88.7% arm is coupled into the silicon device via a VGA. The integrated beamsplitter voltage is set via a Qontrol heater driver and determines the splitting ratio. Light from the other port is collected via the VGA and is incident onto one photodiode of the homodyne detector presented in chapter 3. In this configuration, the detector is used as a amplified photodetector with a current proportional to optical signal intensity. The RF output of the detector is split via a bias tee into its DC and AC components. The DC is coupled into an oscilloscope (Tektronix TDS2012B) and acts as an average power meter and the AC component is passed through a DC-22 MHz low pass filter and then coupled into a 1 GHz electrical spectrum analyser (R&S FPC 1007) giving a measure of the optical intensity squared per hertz.

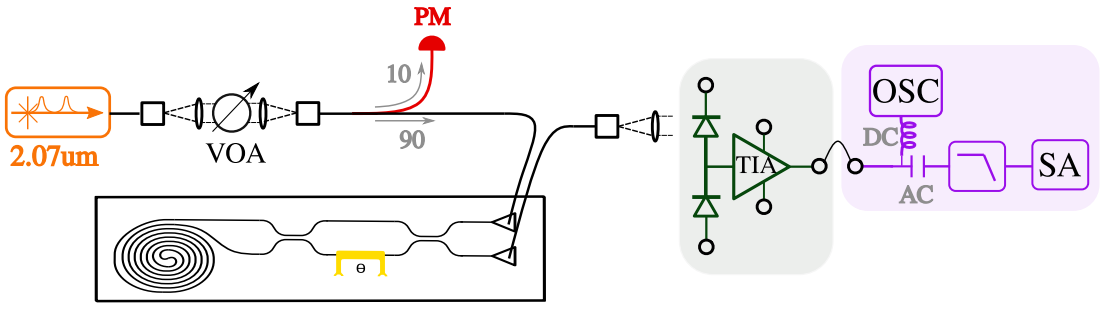

FIGURE 4.12. Experimental diagram of the integrated noise suppression scheme. The pulsed laser is passed through a VOA and is optically coupled to the chip via a VGA. A 10% fiber splitter acts as in input power monitor. Light is collected from the chip via the VGA and is coupled into on side of the homodyne detector. The output RF signal is analysed via an oscilloscope and spectrum analyser.

To asses the noise level of the laser, we measure RIN – a measure of the noise power per hertz normalised by the total average power in the signal. For a classical noise limited laser beam, the RIN is constant with increasing average power since both components scale at the same rate. Note this does not hold true for a shot-noise limited source. Using the standard definition of RIN in linear units, as measured by an ESA with 50 Ω input impedance, we get[175]:

$$\mathrm{RIN} = \frac{50\Omega \cdot \mathrm{PSD}_{\mathrm{lin}}}{BV_{\mathrm{DC}}^2} \quad [1/\mathrm{Hz}]. \tag{4.33}$$

Here, B is the resolution bandwidth of the ESA, $\mathrm{PSD}_{\mathrm{lin}}$ is the power spectral density as measured by the ESA but converted to linear units, V_{DC} is the DC voltage as measured by the oscilloscope (proportional to average laser intensity) and the factor of 50Ω converts voltage PSD to optical PSD. In the results below, we plot the logged-RIN in units of [dBc/Hz] for specific frequencies as functions of input optical power.

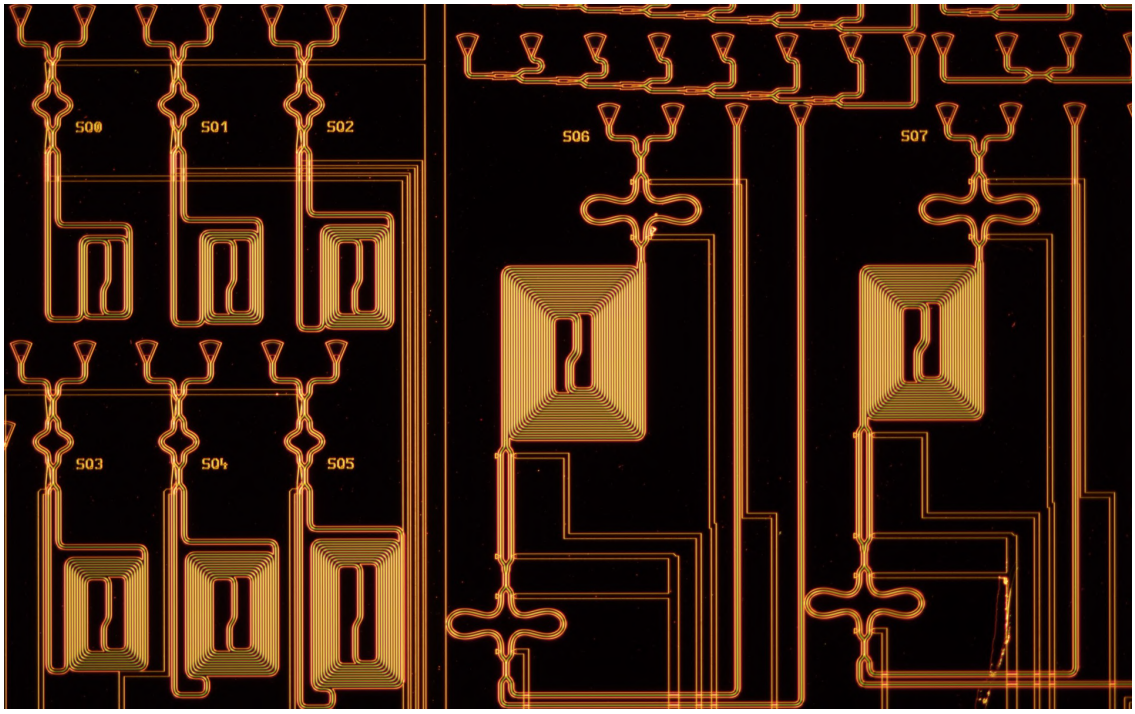

FIGURE 4.13. A photo of Cornerstone Sagnac squeezing devices taken via an Olympus microscope (negative image).

In each measurement, the PSD and DC voltage is averaged over 5 traces of the ESA with a video bandwidth of 100 Hz, resolution bandwidth of 300 kHz, span of 45 MHz and sweep time of 1.6 s. A key benefit to measuring the RIN via our homodyne detector is that both DC and AC components are measured from the same electrical signal. As a result, the RIN measurement is immune to variations in detector coupling or chip coupling on time scales greater than the sweep time of one trace as these dependencies cancel. Chip coupling has been measured to have a standard deviation of 1.1 µW over a 2 s measurement. Detector coupling has been measured to have a standard deviation of 2.6 mV. All other dependencies, such as ESA input impedance and resolution bandwidth, along with parasitic electrical losses, can be considered stable across the trace averaging, giving

a measure that is sufficiently precise and repeatable for output voltage greater than 10 mV.

We start by utilising the setup to measure the RIN of the laser through both an in-out grating and spiral test structure of similar length to the Sagnac spiral. In this measurement, we can asses both the base RIN of the laser through the silicon device, Fig. 4.14(a), and the effect of propagating through a longer section of waveguide to check for additional noise added by the waveguide, Fig. 4.14(b). When performing this measurement, we were expecting the RIN to remain constant and the same for both structures. What we found is that propagation through the spiral introduces additional broadband noise consistent with the theory of modulation instability (MI).

Modulation instability is a nonlinear effect in which small variations in the intensity of the laser grow exponentially across a broadband frequency range about the carrier due to a combination of anomalous dispersion and self-phase modulation[176]. In the frequency domain, it can be considered as four-wave mixing with phase-matching provided by SPM. MI is a well established phenomena often witnessed in near-infrared optical fibers and has been utilised for optical amplification[177]. Following the linear stability analysis of Eq. 4.20, adapted to include the effect of group velocity dispersion as derived by Alem *et al.*, we can model the linear loss corrected MI gain spectrum via[176]:

$$G_{\mathrm{MI}} = \begin{cases} e^{-\alpha L}\left(1 + 2\left(\frac{\gamma P_{\mathrm{p}}}{g}\right)^2 \sinh^2(g L_{\mathrm{eff}})\right) & \omega < \frac{2\gamma P_{\mathrm{p}}}{|\beta_2|} \\ 0 & \omega \geq \frac{2\gamma P_{\mathrm{p}}}{|\beta_2|} \end{cases} \tag{4.34}$$

where $g = -\beta_2\omega\left(\gamma P_{\mathrm{p}} + \frac{\beta_2\omega}{4}\right)$ and P_{p} is the pulse peak power at the input.

Due to the waveguide having low anomalous dispersion, the bandwidth over which MI gain occurs is much larger than the detection bandwidth. Figure 4.14(b) plots the MI corrected RIN at 3 MHz which agrees with the measured RIN for average powers less then 20 mW. The resulting RIN is near 10 dB greater than its base value due to the effects of MI. Above 20 mW, this model overestimates the RIN most likely due to the fact that peak power depletion is not accounted for in the linear stability analysis of MI. Figure 4.14(c) shows that this additional noise is indeed broadband across the detector bandwidth. This additional noise presents a significant problem with using anomalous waveguides for classical noise reduction in this scheme. Next, we characterise the RIN from the asymmetric Kerr interferometer.

Figure 4.15(a) shows the step-like behavior as measured from the the interferometer with three different heater voltages corresponding to three splitting

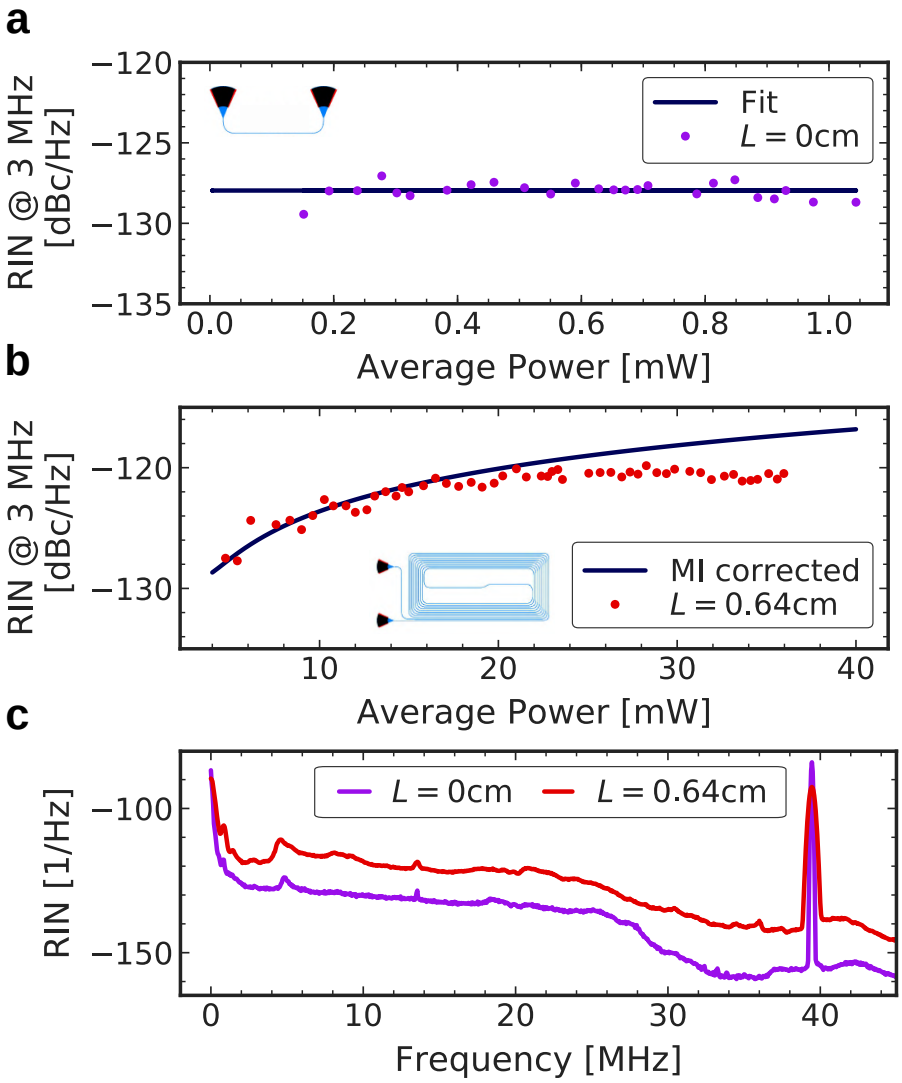

FIGURE 4.14. A comparison of RIN at 3 MHz with power through (a) an in-out grating structure (red), fit to a constant (blue), and (b) a spiral of length 0.64 cm (red), plotted along side the MI corrected RIN (blue). (c) the RIN spectrum through both structures with 40 mW input power.

ratios listed in the legend. As the splitting ratio approaches the balanced 50:50 case, the first step occurs at higher input powers as discussed in Section 4.1.4.

The power scan range has been limited to 0–15 mW as above this range our model for MI has been proven to over-predict the RIN and could therefore lead to an overestimation of noise suppression. The associated RIN for each beam-splitter setting is plotted in Figure 4.15(b), alongside both the laser baseline RIN and the MI corrected RIN. Note that here, we have adapted the MI corrected RIN from that shown in Rig. 4.14(b) to reflect the fact that the Sagnac spiral is slightly

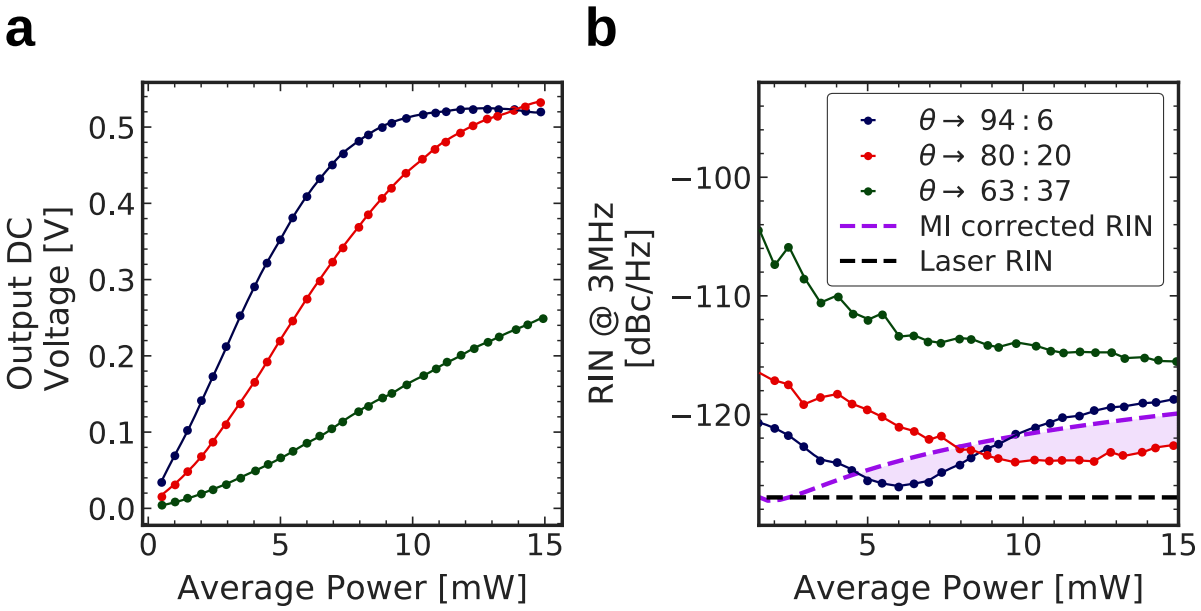

FIGURE 4.15. (a) measured power relations for three Sagnac asymmetric Kerr interferometers with a spiral lenght of 0.58 cm and splitting ratios 94:6 (blue), 80:20 (red) and 63:37 (green). (b) RIN at 3 MHz as a function of input power for each splitting ratio. Data is plotting against the modulation instability corrected RIN from a strip waveguide of equal length (purple) and the laser baseline RIN (black).

shorter with a length of 0.58 cm. In comparing the RIN from each interferometer with the laser baseline RIN, we find that the scheme does not suppress noise below the level of noise exiting the laser. However, noise is suppressed by approximately −2 dB when comparing to propagation through a strip waveguide of equal length.

4.5 Discussion

Modulation instability from a single pump does not occur in normal dispersive waveguides MI[176]. We note that generally modulation instability can occur in the normal dispersion regime but requires cross-phase modulation (XPM) between two wavelengths[178] or orthogonal polarizations in high-birefringence fibers[179] to take effect. As such, designing for a normal dispersive waveguide should counter MI and may result in a device that can suppress noise below the laser baseline RIN, thus providing a benefit for integrated absorption sensing schemes[180]. With a waveguide height of 340 nm, achieving normal dispersion is not possible for

waveguides of reasonable width. Most silicon fabrication houses offer a standard silicon height of 220 nm. At this height, β_2 =13.9 ps^2/m for a waveguide 500 nm wide suggesting this scheme may be better suite to 220 nm technology.

Nonetheless, this device can be used to traverse sections of waveguide in integrated sensors that may have otherwise added to the intensity noise through MI. One point to note in this application is that the output power will also be less depending on the splitting ratio. For example, a Sagnac interferometer with splitting ratio 80:20 could be used to propagate through 0.58 cm of waveguide giving the benefit of −2.2 dB intensity noise reduction in comparison to a strip of equal length but with the additional cost of −1.0 dB less average power.

The applications of such a technology in integrated sensing are not immediately obvious, however, having the ability to offset the unwanted effects of MI may have applications in integrated optical pulse delay lines. Optical delays are essential in communication applications, where they are mainly used for optical signal buffering and synchronization[181,182], and in sensing where they are used in optical coherence tomography[183]. Integrated solutions have been explore as a potential replacement for fiber as they offer greater, sub-ps, delay resolution[184], however, in pulsed applications, real time integrated delays require strict nonlinear optics and dispersion engineering to maintain pulse form, with pulse broadening ultimately limiting communication bit rates. This is typically overcome with soliton engineering which requires broadening from anomalous dispersion be balanced by SPM[173]. In such anomalous waveguides, the effects of additional noise due to MI has been proven to limit the achievable time-division multiplex bit rate of a communication system[185].

4.5.1 Barriers to pulsed noise suppression in silicon

We can summarise several factors that limit the noise suppression performance of the Cornerstone devices, and which stand in the way of an integrated Kerr-based squeezing measurement at this wavelength in silicon:

1. Excess laser noise at megahertz speeds present a greater initial noise floor that must be overcome when attempting to squeeze.

2. The build up of additional broadband noise from modulation instability inside anomalous silicon waveguides.

3. Potential thermo-refractive noise within the silicon waveguides.

In the introduction of this chapter we discuss the potential options for overcoming additional laser noise and conclude that no commercial technology currently exists to actively suppress noise in this region of the spectrum. The RIN dynamics of passive mode-locked fiber lasers are complex and rely on many intracavity and external cavity parameters[186,187]. At megahertz speeds, prominent intensity noise sources are likely to be intensity noise coupling through from the driving laser diode and amplified spontaneous emission. Historically, methods to overcome such noise and provide shot-noise limited pulsed operation rely on techniques that engineer the laser itself such as intracavity spectral filtering or feedback loops into the laser cavity[187]. External methods, such as feedback or feed-forward circuits coupled to an optical modulator or external cavity filtering, all require fast and low-noise electronics[187]. Until the development of such a laser at 2 µm, excess laser noise will continue to be an issue for squeezed state development requiring pulsed lasers.

It is possible to adapt the scheme presented here to provide squeezed vacuum by setting the Sagnac beasmplitter to 50:50[188]. In this configuration, classical noise in the laser is theoretically rejected from the squeezed vacuum output. However, near perfect interference visibility is required to fully reject the classical noise. The broadband spectrum of the pulse presents an issue for high visibility interference due to the limited operational bandwidth of the integrated beamsplitter. One option to improve the bandwidth is to switch the direction couplers for multi-mode interference couplers (MMIs), however, MMIs typically display greater losses which will pollute any squeezed statistics produced. As a rough estimate for the level of extinction required we can use Eq. 2.30 to estimate the number of photons present in a squeezed vacuum with 3 dB squeezing to be just $\langle n \rangle = 13$. To preserve squeezed statistics the coherent amplitude must be sufficiently rejected to a similar magnitude. Attempts to achieve good visibility using the Cornerstone devices presented here were limited to 99.8%. Additionally, the Sagnac configuration will only reject slow classical noise that is correlated across the two counter propagating arms. As such, any noise at speeds comparable to the repetition rate of the laser introduced by the waveguide itself will be present in the output vacuum. In comparison, the second point listed above can be overcome relatively easily via migration to a 220 nm silicon platform that displays normal dispersion at 2 µm.

Thermo-refractive noise stems from statistical variations in the temperature of the chip which drive fluctuations in the refractive index through the thermo-optic coefficient[170]. This effect was recent observed in a silicon nitride squeez-

ing scheme carried out by Cernansky *et al.* who measured excess noise below 500 MHz from this effect[159]. Fast detection was required to overcome this. We cite this as a likely concern here due to the thermo-optic coefficient being an order of magnitude larger in silicon compared to silicon nitride[189]. This noise source has been proven to have a characteristic scaling of $1/\omega^2$. It is possible that once MI is suppressed, thermo-refractive noise will limit the scheme, at which point access to a faster detector would be significant for characterisation.

4.6 Conclusion

In conclusion, we have simulated 2.2 dB as an upper bound on the amount of amplitude squeezing possible when utilising a shot-noise limited 2 µm pulsed laser with pulse properties listed in Appendix B. We present an asymmetric Kerr interferometer device, initially designed for squeezing, as a broadband, all-optical, classical noise suppression device simulated to be capable of up to −15 dB intensity noise suppression at the cost of a 5.6 dB drop in average power. We measure preliminary devices and find that modulation instability, due to anomalous dispersion, adds broadband parasitic intensity noise to the pulsed laser. Despite this, we measure an intensity noise suppression of 2 dB below the level present in a field that traverses the same length in a strip waveguide of equal geometry. We discuss further limitations of this particular scheme for the production of 2 µm squeezed states from enhanced absorption sensing. Note that in chapter 6 we discuss a more viable route towards integrated silicon squeezing at 2 µm based on more recent progress in the field of integrated squeezing.

This concludes experimental work carried out on the production of quantum resources for integrated absorption spectroscopy in the 2 µm–band. We now move on to discuss theory-based work on the utility of quantum states for enhanced sensing applications.

Chapter 5

Maximising Precision in Saturation-Limited Absorption Spectroscopy

Declaration of contribution: *worked carried out in this chapter was solely carried out by myself, under the supervision of Euan Allen. The research paper on which this chapter is based was also written solely by myself, with feedback and advice given by the additional authors.*

In this chapter we explore the effect of unwanted sample saturation on the precision of absorption spectroscopy. This work closely follows results I have published in Ref.[190]. The figures have been adapted from those presented in Ref.[190] with some text quoted verbatim.

In absorption spectroscopy, exceeding sample-specific probe intensities often leads to irreversible damage through a host of saturation-dependent mechanisms[73,74]. It is therefore crucial to investigate how different optical probes perform in the presence of saturation. Only then can we simultaneously optimise performance and minimise the irreversible damage[191–193] of delicate samples such as archaeological finds, living cells, or food products[194–196]. Notably, UV absorption spectroscopy of biological samples is often limited to intensities as low as 1 nW/μm^2 to ensure damage does not occur.

As discussed in chapter 2, many optical probes contain inherent intensity noise stemming from the quantum nature of light. In a coherent state this quan-

tum noise scales favorably with probe power but fundamentally limits the precision of classical absorption measurements. It follows that using a brighter probe will give favorable performance, however, this strategy is limited by the saturation intensity of the sample which places a bound on the achievable measurement precision. By conducting a Fisher information analysis[197] – a measure of how much information about an unknown parameter we can extract – of how saturation affects measurement precision, we are able to present a probe-sample optimisation scheme to help classical measurements obtain the highest precision possible with a classical probe. We find that the optimal probe power is always in the saturation regime ($\geq 50\%$ of the saturation power) which highlights an inherent trade-off between precision and damage that saturation-limited classical schemes will have to navigate. This lower bound motivates the need to find alternative probe states that can provide greater precision per photon.

Previous work in the field of quantum metrology[45] has identified optimal states for parameter estimation as being non-classical states of light capable of enhancing performance when sensing a linear loss or acquired phase for a fixed number of photons[196,198–200]. Results thus far have focused on the linear absorption regime, with the exception of work by Mitchell *et al.*[201] that models the effect of constrained photon number on the performance of Gaussian states for single-parameter estimation. They numerically explored the performance of Gaussian states for measuring optical depth under a semi-classical model of saturation. Here, we derive an analytical bound on the performance of any single mode states (both Gaussian and non-Gaussian) under saturation. To help identify the best strategy for a given measurement, we assess the ability of classical coherent states, technically challenging Fock states, and readily available squeezed states to saturating this bound. The results presented in this chapter show that the Fock state remains optimal for probing in the saturation regime, giving a deeper understanding of when to consider quantum light sources a worthwhile and viable upgrade to saturation-limited measurements. Additionally, the new theoretical framework outlined here opens the door to further analysis of nonlinear absorption spectroscopy schemes which directly employ saturation to enhance image resolution[202,203]. These schemes often incorporate transmission measurements of weak signals into more complex estimators and can therefore build upon the model presented here for further optimisation.

We start by constructing a semi-classical model of saturation. We outline Fisher information (FI) and quantum Fisher Information (QFI) formalisms and uses these to investigate achievable measurement precision for the states men-

tioned above. Using our results, we present a sample-probe optimisation strategy which we later apply to two examples. We then derive a bound on the achievable precision of any single-mode quantum state. Our work shows the FI obtained by the Fock state saturates this bound and is thus an optimal state in the presence of saturation. For a given target precision, we show the quantum probe brightness to be of an order of magnitude less than the required classical probe brightness, making it desirable for ultra-sensitive samples. We identify amplitude-squeezed states as a viable route towards quantum precision enhancement for saturation-limited sensors. The analytical results presented are based on a semi-classical approximation of sample saturation. Complementary to these results, we complete a fully-quantum numerical analysis of the effect of saturation on the higher order moments of the probes photon statistics and find the analytical quantum advantage to be a lower bound on the achievable advantage of employing quantum light.

5.1 Saturation modelling and parameter estimation

We start by presenting a semi-classical model of saturation in guided absorption spectroscopy measurements.

5.1.1 A Semi-classical model of saturation

A schematic of the semi-classical model we consider is shown in Fig. 5.1. A saturable absorber of fixed, known, length $L \in (0, \infty)$ cm and saturation intensity n_s is probed with a resonant optical state. The linear absorption coefficient $a \in (0, \infty)$ cm^{-1} is unknown and is the target variable we wish to estimate. The probe is considered a single optical mode with known mean input photon number $\langle \hat{n} \rangle$. The sample is modelled via an ensemble of independent two-level atoms which are considered to be isolated from the environment, exhibiting no internal interactions or temperature dependent effects. The ensemble distribution is static and homogeneous. We also make the assumption that the evolution is dominated by decoherent effects such that the interaction between the optical mode and ensemble remains classical. This assumption holds true for nearly all absorption spectroscopy measurements that are not specifically designed to exploit coherent interactions such as Rabi oscillations. Although simplified, this two-level model can be readily extended to more complex multi-level systems which display a dominant radiative or non-radiative decay path back to ground[204,205]. To

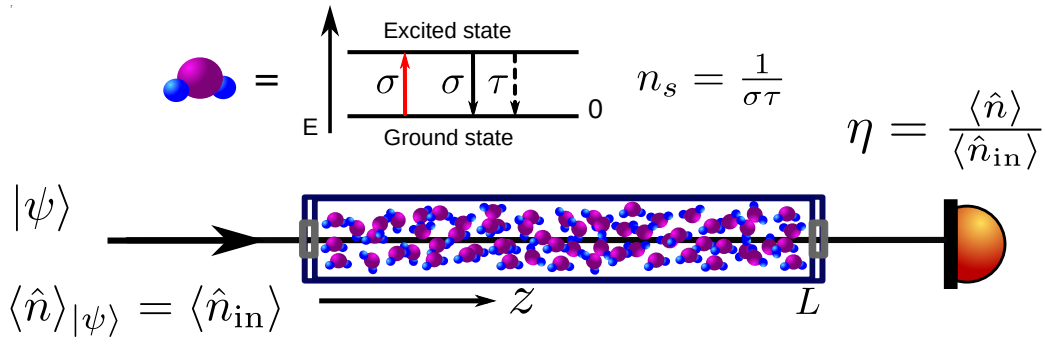

FIGURE 5.1. The model schematic: a probe state of mean input photon number $\langle\hat{n}\rangle$ is propagated along a sample of length L. The sample consists of homogeneously distributed two-level absorbers with density n_t, characteristic transition cross-section σ, and lifetime τ. The output transmission η is measured and used to infer an estimate of the linear absorption coefficient a. (Figure adapted from Ref.[190].)

estimate the linear absorption coefficient, the mean photon number is measured at the output via direct photo-detection. Repeated measurements of the transmission then enable us to build up an estimate of the absorption. It is the precision of this estimate that we analysis to compare the performance of different probe states.

We start by performing a standard population analysis of the ground and excited states in the ensemble as originally performed by Enstien[206]. By doing so, we find an expression for the transmission which expands on the linear Beer-Lambert law[207] to account for nonlinear absorption that occurs across the sample in the high power, low saturation intensity, regime. We solve for the intensity of an optical mode, $\langle\hat{n}(z)\rangle$, as a function of position z along the sample. Note that we assume a unit modal area of 1 without loss of generality and so refer to photon number and intensity synonymously. Each particle has a given interaction cross section σ – the probability a particle will absorb a photon – and a transition relaxation time τ. The total number of particles in the ensemble, n_t, is conserved with n_0 and n_1 accounting for the number of particles in the ground and excited states respectively. It follows that:

$$n_t = n_0 + n_1. \tag{5.1}$$

Following Enstien's derivation, the rate equations for the populations of the ground and excited states at a given position z, accounting for absorption, stim-

ulated emission, and spontaneous emission are[206]:

$$\begin{aligned}\frac{dn_0}{dt} &= -\sigma\langle\hat{n}(z)\rangle n_0 + \sigma\langle\hat{n}(z)\rangle n_1 + \tau^{-1} n_1,\\ \frac{dn_1}{dt} &= \sigma\langle\hat{n}(z)\rangle n_0 - \sigma\langle\hat{n}(z)\rangle n_1 - \tau^{-1} n_1.\end{aligned} \tag{5.2}$$

As the flux of photons passes through a slab of thickness dz, we make the assumptions that the relaxation time of the transition is long enough such that the populations of n_1 and n_0 can be considered constant. Under this steady-state assumption, $\frac{dn_1}{dt} = 0$ and $\frac{dn_0}{dt} = 0$. This allows us to solve for n_1 and n_0 using Eq. 5.1 and either one of 5.2:

$$\begin{aligned}n_0 &= \frac{n_t(\sigma\langle\hat{n}(z)\rangle + \tau^{-1})}{2\sigma\langle\hat{n}(z)\rangle + \tau^{-1}},\\ n_1 &= \frac{n_t\sigma\langle\hat{n}(z)\rangle}{2\sigma\langle\hat{n}(z)\rangle + \tau^{-1}}.\end{aligned} \tag{5.3}$$

Propagating along dz, the change in the probe intensity, $d\langle\hat{n}(z)\rangle$, is given by the net change in population:

$$\frac{d\langle\hat{n}(z)\rangle}{dz} = \sigma\langle\hat{n}(z)\rangle(n_1 - n_0). \tag{5.4}$$

Here we assume spontaneous emission coupling back into the mode is negligible, as is the case for measurement schemes that do not employ cavities. Using the solutions for n_1 and n_0 gives a differential equation for $\langle\hat{n}(z)\rangle$:

$$\frac{d\langle\hat{n}(z)\rangle}{dz} = -\frac{\tau^{-1} n_t\sigma\langle\hat{n}(z)\rangle}{\tau^{-1} + 2\sigma\langle\hat{n}(z)\rangle}. \tag{5.5}$$

Let $a := n_t\sigma$ and $n_s := \frac{1}{\sigma\tau}$. These are the standard definitions of the linear absorption coefficient and saturation intensity. Recast with these substitutions:

$$\frac{d\langle\hat{n}(z)\rangle}{dz} = -\frac{a\langle\hat{n}(z)\rangle}{1 + 2\langle\hat{n}(z)\rangle/n_s}. \tag{5.6}$$

Interestingly, we may expand the quotient into a geometrical series to give:

$$\frac{d\langle\hat{n}(z)\rangle}{dz} = -a\langle\hat{n}(z)\rangle\Big(1 - 2\langle\hat{n}(z)\rangle/n_s + O((2\langle\hat{n}(z)\rangle/n_s)^2)\Big) \tag{5.7}$$

The leading order term recovers the linear Beer-Lambert law of absorbance with additional terms becoming non-negligible as $\langle\hat{n}(z)\rangle/n_s$ grows.

We can now solve for $\langle\hat{n}(z)\rangle$ via separation of variables followed by integration from 0 to z. Let $\langle\hat{n}(0)\rangle := \langle\hat{n}_{\text{in}}\rangle$,

$$e^{\frac{2\langle\hat{n}(z)\rangle}{n_s}}\left(\frac{2\langle\hat{n}(z)\rangle}{n_s}\right) = e^{\ln\left(\frac{2\langle\hat{n}_{\text{in}}\rangle}{n_s}\right) + \frac{2\langle\hat{n}_{\text{in}}\rangle}{n_s} - az}. \tag{5.8}$$

Equation 5.8 has been rearrange into a form with which we can use the Lambert-W function, defined by:

$$W\left(ze^{z}\right) = z. \tag{5.9}$$

Furthermore, using a special case of the Lambert-W function, known as the Wright Omega function[208], defined by $W(e^{z}) = \mathcal{W}(z)$, gives the final solution:

$$\langle \hat{n}(z) \rangle = \frac{n_s}{2} \mathcal{W}\left(\ln\left(\frac{2\langle \hat{n}_{\text{in}} \rangle}{n_s}\right) + \frac{2\langle \hat{n}_{\text{in}} \rangle}{n_s} - az\right). \tag{5.10}$$

The intensity through a sample of length L with linear absorption coefficient a, saturation intensity n_s and input probe intensity $\langle \hat{n}_{\text{in}} \rangle$ is therefore given by:

$$\eta = \frac{n_s}{2\langle \hat{n}_{\text{in}} \rangle} \mathcal{W}\left(\ln\left(\frac{2\langle \hat{n}_{\text{in}} \rangle}{n_s}\right) + \frac{2\langle \hat{n}_{\text{in}} \rangle}{n_s} - aL\right). \tag{5.11}$$

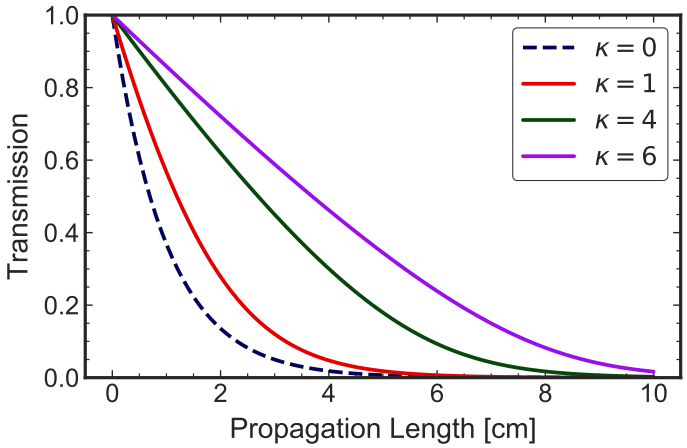

FIGURE 5.2. Sample transmission as a function of length for several κ. $\kappa = 0$ (dashed blue) recovers the linear Beer-Lambert law. $\alpha = 1$ /cm and $n_s = 4$. (Figure adapted from Ref.[190].)

To simplify the maths, we introduce $\kappa = 2\langle \hat{n}_{\text{in}} \rangle / n_s$ as a dimensionless quantity giving:

$$\eta(\kappa) = \frac{1}{\kappa} \mathcal{W}(\ln(\kappa) + \kappa - aL). \tag{5.12}$$

We have plotted a few examples of how this function varies with increasing length in Fig. 5.2. As we increase κ, the transmission function shifts from an exponential, as determined by the linear Beer-Lambert law, to a linear fall-off conducive of saturated absorption. From here onwards, we refer to probing in the saturation regime as $\kappa > 1$. Conversely, $\kappa \leq 1$ is defined as probing in the linear regime.

5.1.2 Fisher information analysis

In this section, we outline FI formalism and use it in conjunction with our equation for transmission to calculate the precision gained on our estimate from a given optical probe. To build some intuition for FI, we start with an informally example. We then move onto a formal definition.

What is Fisher information?

Let us suppose we are trying to estimate the mean number of visits to A&E per hour, y_{mean}. Since this is a discrete random variable, it must follow some probability mass function which we can assume in this case to be Poissonian. We start by collecting a data set, noting down the number of visits per hour over a fixed period. We can then fit this data to a Poissonian and extract an estimate for the mean $y^{\text{est}}_{\text{mean}}$. It is important to note two points: (1) there is no way of knowing whether our chosen probability mass function is a true description of the process and (2) whether the estimate of the mean obtained from our limited data set is close to the true mean. Since we can never know how close to the true mean our estimate is, we instead ask the question: for a given measured number of visits in an hour, y, how much *information* does that measurement contain about the true mean? Here, information is a defined quantity which evaluates the number of probable $y^{\text{true}}_{\text{mean}}$ that could have reasonable lead to the measurement y.

To quantify this notion of information in a data set, we start by mathematically assessing how likely it was that each possible true mean, $y^{\text{true}}_{\text{mean}}$, could have led to each measured value. This is exactly quantify by the probability mass function employed not as a function of the discrete variable y with some fixed mean, but as a function of true mean for some measured y. This is known as the likelihood function and it displays a peak for mean values equal to y and approaches zero for mean values far from y. At this point we note that an assumption about the true probability mass function is still required. We can plot the likelihood for each measurement in a set of measurements, giving a distribution of likelihood (functions).

To quantify the information acquired about the true mean from a set of measurements, we take the derivative of each logged-likelihood function with respect to $y^{\text{true}}_{\text{mean}}$, known as the score function. The derivatives approach zero for $y_{\text{mean}} = y$ on each measurement. These scores, as functions of a discrete random variable y, are also themselves discrete random variables, and therefore display some distri-

bution over the set of measurements. If it is the case that each measured value is likely explained by several possible true mean values i.e. the peak in each score is broad, then we state that our measurements carries low *information* about the true mean as it is reasonable to conclude that the true mean could have been a large number of plausible values. To capture this notion, the Fisher information is then defined as the variance of the distribution of scores. It follows that the smaller the variance, the greater the likelihood that the observed values will give an accurate estimate of the true mean.

Formally, the FI on an unknown target variable x, obtained by the set of quantum positive-operator valued measurements (POVMs), $\hat{\mathbf{M}} = \{m_i\}$ with $\sum_i m_i = 1$, is defined as

$$F(x) = \sum_i p(m_i|x) \left(\frac{\partial \ln p(m_i|x)}{\partial x} \right)^2 \tag{5.13}$$

[197,209]. Here, the probability measurement outcome i is given by

$$p(m_i|x) = \mathrm{tr}\{ |\psi_x\rangle\langle\psi_x| \, m_i \} \, . \tag{5.14}$$

Instead of calculating the FI explicitly using the definition above, we invoke what's known as the Cramér-Rao bound (CRB) relating the FI to the variance of a given estimator of x, inequality *1* of Eq. 5.15[210]. The CRB states that the FI on x is lower bounded by the inverse of the variance of x over a measurement set. This bound is necessarily saturated by an optimal, unbiased, estimator. Here, an unbiased estimator is defined as one that supplies a mean that converges on the true value of x over infinite measurements.

The quantum Fisher information (QFI) $\mathcal{Q}(x)$ is defined as the maximum possible FI obtained by further optimising over all measurement POVMs and is related to the FI via the quantum Cramér-Rao bound (QCRB), inequality *2* of Eq. 5.15[211]:

$$\frac{1}{\mathrm{Var}(x)} \overset{1}{\leq} F(x) \overset{2}{\leq} \mathcal{Q}(x). \tag{5.15}$$

To calculate the FI gained from a probe state $|\psi\rangle$ on the unknown parameter a, we invoke the CRB. This is possible because transmission is an optimal unbiased estimator for the linear absorption coefficient in direct absorption schemes[200]. The FI on the transmission measurement, $\hat{\eta}$, is thus given by:

$$F(\eta) = \frac{1}{\mathrm{Var}(\eta)}. \tag{5.16}$$

Given that $\eta := \langle\hat{n}\rangle / \langle\hat{n}_{in}\rangle$ is a continuous linear differentiable function of output intensity $\langle\hat{n}\rangle$, we can relate the variance in the transmission to the variance of the

output photon number via the error propagation formula[212]:

$$\begin{aligned} \mathrm{Var}(\eta) &= \left(\frac{\partial \eta}{\partial \hat{n}}\right)^2 \mathrm{Var}(\hat{n}) \\ &= \frac{\mathrm{Var}(\hat{n})}{\langle \hat{n}_{\mathrm{in}} \rangle^2}. \end{aligned} \tag{5.17}$$

The FI is therefore given in terms of the photon number variance $\mathrm{Var}(\hat{n})$ of the output state:

$$F(\eta) = \frac{\langle \hat{n}_{\mathrm{in}} \rangle^2}{\mathrm{Var}(\hat{n})}. \tag{5.18}$$

Using error propagation again, the FI on η can be related to the FI on a via the formula:

$$\begin{aligned} F(a) &= \left(\frac{\partial \eta}{\partial a}\right)^2 F(\eta) \\ &= \left(\frac{\partial \eta}{\partial a}\right)^2 \frac{\langle \hat{n}_{\mathrm{in}} \rangle^2}{\mathrm{Var}(\hat{n})}. \end{aligned} \tag{5.19}$$

Using the following formula for the derivative of the Wright Omega function[208]:

$$\frac{d\mathcal{W}(x)}{dx} = \frac{\mathcal{W}(x)}{1+\mathcal{W}(x)}. \tag{5.20}$$

we can calculate the derivative of η via a substitution $u = \ln(\kappa) + \kappa - aL$:

$$\begin{aligned} \frac{\partial \eta}{\partial a} &= -\frac{L}{\kappa}\frac{\partial \mathcal{W}}{\partial u} \\ &= -\frac{L\eta}{1+\eta\kappa}. \end{aligned} \tag{5.21}$$

Combining Eq. 5.19 with Eq. 5.21 gives an expression for the FI gained by a state $|\psi\rangle$ on a as a function of output state photon number variance:

$$F(a) = \left(\frac{L\eta}{1+\eta\kappa}\right)^2 \frac{\langle \hat{n}_{\mathrm{in}} \rangle^2}{\mathrm{Var}(\hat{n})}. \tag{5.22}$$

We now apply Eq.5.22 to several different states, commenting on how saturation effects measurement precision.

5.2 Semi-classical estimation of absorption under saturation

In our saturation model thus far, we make the assumption that the quantum loss channel acts like a beam splitter on the optical mode with reflectivity determined

by $1-\eta(\kappa, a)$. This semi-classical approximation only accounts for the effect of saturation on the first-order moment of the input state's photon number and thus does not account for the effect on its quantum noise. In effect, we approximate the loss on each basis state of a given probe to be the the loss experienced by the states mean photon number. Without this assumption, we cannot analytically solve for the FI. In Sec.5.3, we go beyond this assumption and numerically solve the fully-quantum model allowing us to comment on both the validity and utility of this assumption.

5.2.1 Classical probe performance

In chapter 1, we saw how a classical laser probe is well approximated by a coherent state[213] $|\alpha\rangle$ with $\langle\hat{n}_{in}\rangle = |\alpha|^2$ and $\mathrm{Var}(\hat{n}_{in}) = \langle\hat{n}_{in}\rangle$. The semi-classical loss approximation allows us to define the output photon number variance analytically via a virtual beamsplitter[80,200]:

$$\mathrm{Var}(\hat{n}) = \eta^2\mathrm{Var}(\hat{n}_{in}) + \eta(1-\eta)\langle\hat{n}_{in}\rangle. \tag{5.23}$$

For a coherent input state, the FI, $F_c(a)$, is therefore given by:

$$F_c(a) = \left(\frac{L\eta}{1+\eta\kappa}\right)^2 \frac{\langle\hat{n}_{in}\rangle}{\eta}, \tag{5.24}$$

which is plotted in Fig. 5.3(a). We also define efficiency to be $F_c(a)/\langle\hat{n}_{in}\rangle$, the FI normalised by the number of input photons.

The first thing to note is that the negative effect of saturation on classical probe efficiency, Fig. 5.3(a), is visible for $\kappa \ll 1$ suggesting sample saturation has a measurable impact on shot-noise limited schemes probed far below saturation. For a given sample of known length and estimated absorption, we can maximise the FI over probe power. We find the optimal probe intensity n_{opt} to be:

$$n_{\mathrm{opt}} = \frac{n_s}{2}\mathscr{W}[1+aL] \geq \frac{n_s}{2}, \tag{5.25}$$

with a corresponding sample transmission of $\eta_{\mathrm{opt}} = \mathscr{W}[1+aL]^{-1}$. Interestingly, the probe power resulting in the greatest precision is lower bounded by $\kappa = 1$ implying all classical strategies must be probed in the saturation regime to fully optimise performance. This result highlights an inherent trade-off between potential damage and desired precision that under-performing classical schemes will need to navigate. Such a compromise further motivates a move to the quantum regime which is capable of being more effective on a per photon basis.

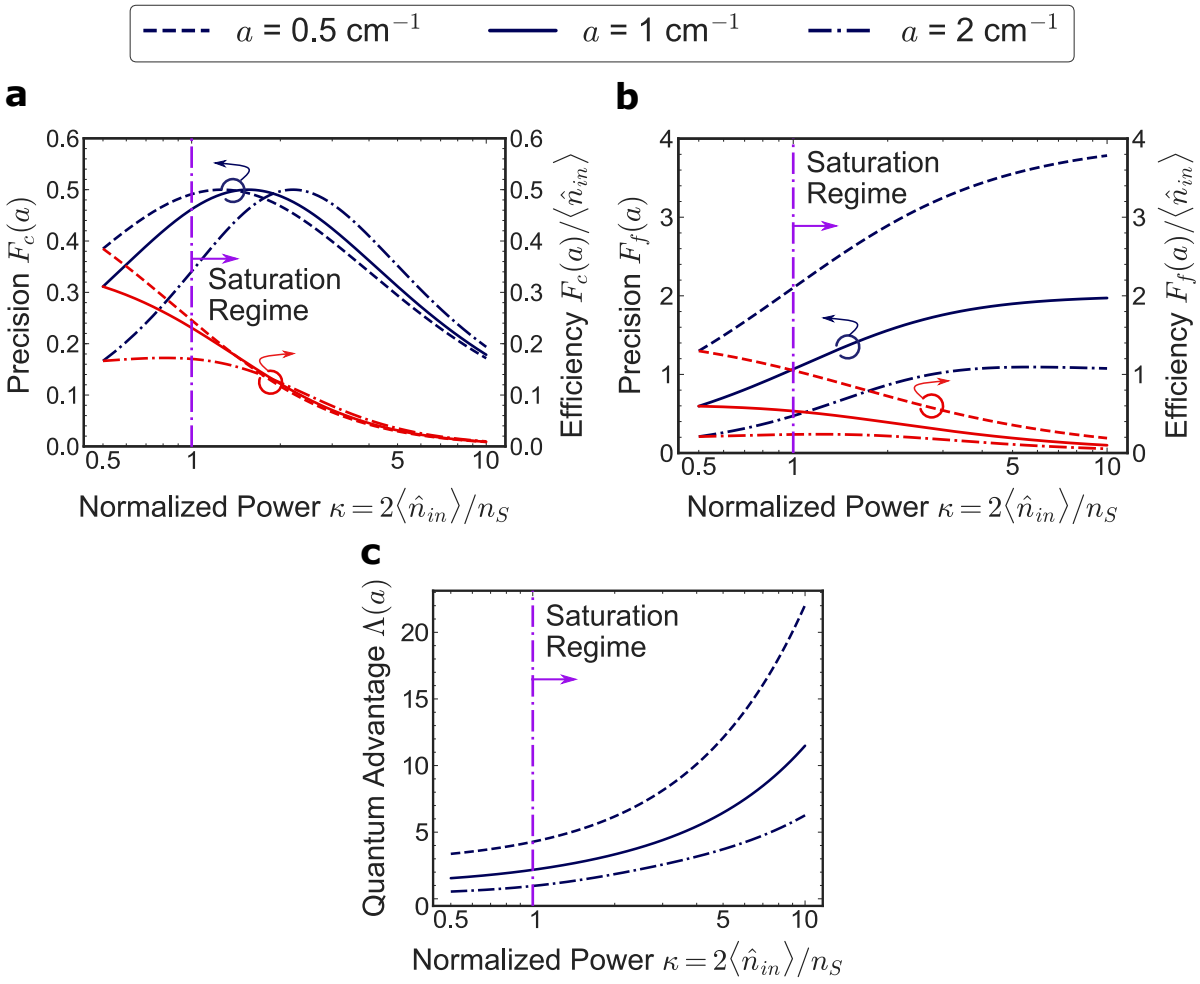

FIGURE 5.3. Precision (blue) and efficiency (red) obtained using (a) a classical probe or (b) an optimal quantum probe, calculated across the linear ($\kappa < 1$) and saturated ($\kappa \geq 1$) pump regimes. (c) shows the quantum advantage $\Lambda(a)$. The sample has a fixed length $L = 1$ cm and is plotted for absorption coefficients $a \in \{0.5\ \text{cm}^{-1}, 1\ \text{cm}^{-1}, 2\ \text{cm}^{-1}\}$[190]. (Figure adapted from Ref.[190].)

5.2.1.1 Examples optimising classical schemes

To highlight the benefits of classical power optimisation, we apply our method to the quantum-limited high-precision absorption spectroscopy of a dilute Cesium vapour cell, used to define the Boltzmann constant k via Doppler broadening thermometry (DBT)[214]. In DBT the characterisation of the line-width profile of a specific transition enables precise estimation of the Boltzmann constant k. DBT is also frequently used to accurately detect and monitor gasses[215] with high measurement precision being imperative to both applications of the technique. In Ref.[214] a shot-noise limited 895 nm laser is used to probe a transition with characteristic saturation intensity $n_s = 2.5\,\mathrm{mW/cm^2}$ through a cell of length 75 mm. A laser intensity of $7\,\mu\mathrm{W/cm^2}$ ($\kappa = 0.005$) is used resulting in a total transmission of $\eta = 17\%$. We can therefore estimate the linear absorption coefficient to be $a = 2.53\,\mathrm{cm^{-1}}$. Using Eq. 5.25, we find the optimal probe intensity to be $2.67\,\mathrm{mW/cm^2}$ ($\kappa = 2.14$) with a resulting sample transmission of $\eta = 47\%$. Employing such a power would result in a 24 dB improvement in the linear absorption estimate precision (total Fisher information). In the absence of saturation, a further 6 dB increase in power would result in a 6 dB increase in precision. Our model shows that once saturation is properly accounted for such an increase in probe power actually results in a -3 dB reduction in precision highlighting the importance of including saturation. Note, the only source of noise we consider here is laser shot-noise. Other sources of noise may scale unfavorably with power (e.g. temperature stability) and therefore may limit the practicality of witnessing such an increase in precision. This example demonstrates the potential gains in accounting for saturation when optimising measurements and highlights the potential for miscalculation when only considering linear absorption.

For a given intensity damage threshold, we can similarly maximise the FI over sample length. As a further example, we investigate the resonant absorption of Chlorophyll A Acetone solution, probed at 661 nm[216]. Chlorophyll A density is routinely measured via absorption spectroscopy in a wide variety of settings[217,218]. The commonly-targeted transition has absorption cross-section $\sigma = 4 \times 10^{-17}\ \mathrm{cm^2}$ with lifetime $\tau = 4\,\mathrm{ns}$[195,219]. Chlorophyll absorption measurements use a typical cuvette width of 1 cm and aim to prepare sample densities that give an output transmission somewhere in the range of $15\% - 50\%$[216]. Suppose we probe a sample with a commercially available high power laser at 1 W ($\kappa = 0.02$) and measure a transmission of 50%. We can infer from this measurement that $a \approx 0.7\,\mathrm{cm^{-1}}$. The optimal sample length of such a measurement is

found to be $L = 2.9\,\text{cm}$ which results in a $3\,\text{dB}$ improvement in precision over the standard $1\,\text{cm}$ cuvette width. Principally, this precision improvement maps directly onto the concentration estimate. As demonstrated above, these results provide simple but powerful optimisation strategies to help improve precision. We now derive a limit on the precision gained via any single-mode state and explore the ability of quantum states to saturate this bound.

5.2.2 A bound on single-mode precision

Birchall *et al.* derived an upper bound on the QFI for single parameter estimation that results in a correlated linear phase and loss being applied to a single mode optical probe[220], which reduces to the following when there is no phase shift applied by the sample:

$$\mathcal{Q}(x) \leq \frac{\langle \hat{n}_{in} \rangle}{\eta(1-\eta)} \left(\frac{\partial \eta}{\partial x} \right)^2 \tag{5.26}$$

The saturation model presented above is insensitive to phase information and depends only on the mean intensity of the input state and sample parameters. Therefore, we can apply this result to our model and note that an optimal quantum probe is one that necessarily saturates this bound. Using Eq. 5.26 in conjunction with Eq. 5.11, we derive a bound on the QFI gained on the linear absorption coefficient a, estimated via the transmission η:

$$\mathcal{Q}(a) \leq \left(\frac{L\eta}{1+\eta\kappa} \right)^2 \frac{\langle \hat{n}_{in} \rangle}{\eta(1-\eta)}. \tag{5.27}$$

Equation 5.27 defines the quantum limit on precision (shown in Fig. 5.3(b)). The Heisenberg limit on precision states that the FI gained from a measurement cannot scale faster than $\langle \hat{n}_{in} \rangle$[221]. Through numerical analysis of Eq. 5.27, we find

$$\lim_{\langle \hat{n}_{in} \rangle \to \infty} \frac{\mathcal{Q}(a)}{\langle \hat{n}_{in} \rangle} = 0 \tag{5.28}$$

Interestingly, the equivalent result under linear absorption converges to a constant[200]. The addition of saturation has therefore degraded the optimal states performance in the high power limit. We now seek to find quantum strategies that saturate this bound and the separation of such strategies from those reliant on classical resources only.

5.2.3 Finding an optimal probe

It is well-known that the Fock state-probe provides an optimal strategy in the linear absorption model[222,223]. We expect this probe to remain optimal under

saturation. To prove this hypothesis, we combine Eq. 5.22 and Eq. 5.23 for a Fock state ($\mathrm{Var}(\hat{n}_{in}) = 0$) to give an expression for the FI achieved via Fock state probing $F_f(a)$:

$$F_f(a) = \left(\frac{L\eta}{1+\eta\kappa}\right)^2 \frac{\langle \hat{n}_{in} \rangle}{\eta(1-\eta)}. \tag{5.29}$$

The FI for a Fock state is indeed equivalent to Eq. 5.27, hence Fock state probing remains an optimal quantum strategy for maximising the precision of the absorption coefficient estimate in the presence of saturation. By setting $\kappa = 0$, we recover well-known linear absorption estimation results with new insight gained for all $\kappa > 0$.

To benchmark the optimal quantum strategy against an equally bright classical strategy we define the quantum advantage $\Lambda(a) := \mathcal{Q}(a)/F_c(a)$ explicitly given by $\Lambda(a) = \frac{1}{1-\eta}$, shown in Fig. 5.3(c). By performing a Taylor expansion around $a = 0\,\mathrm{cm}^{-1}$ we find an expression for the quantum advantage gained under the saturated probing of weakly absorbing samples:

$$\Lambda(a) = \frac{1+\kappa}{aL}, \tag{5.30}$$

valid for $\kappa \geq 1$ and $a \leq \frac{1+\kappa}{L}$. This tells us that we can expect to obtain at best a linear increase in precision with probe power when switching from the classical probe to an optimal quantum probe.

5.2.4 The effect of saturation on precision

Saturation imposes a limit on the maximum precision a Fock, Fig. 5.3(b), or coherent, Fig. 5.3(a), state provides with increasing optical power. This is diametrical to linear loss which suggests probe brightness can always be increased to enhance precision[200]. The knock-on effect is impaired efficiency due to diminishing returns in precision. Whilst the probe power is above saturation, the effective linear absorption is low which limits the information on the loss coefficient carried by each photon. Both the quantum and classical strategies suffer due to this effect, however, the coherent state performance is affected further due to greater optical noise in the input state. The combined effect is a quantum advantage that scales linearly with κ in the saturation regime. The quantum advantage is strongest for weakly absorbing samples, as is the case in trace detection schemes[224,225] or even single-molecule direct absorption schemes[202].

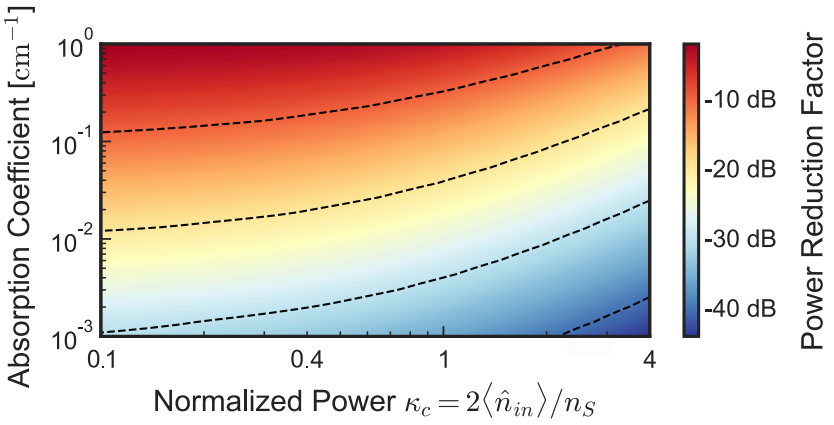

FIGURE 5.4. The probe power reduction achievable by switching from a coherent probe of input intensity κ_c to a Fock state probe without loss of precision. The sample has a fixed length $L = 1$ cm and is plotted for several absorption coefficient. (Figure adapted from Ref. [190].)

5.2.5 Inefficient detection and probe brightness

For a fair comparison between classical and quantum strategies, we can account for the effect of imperfect detection in the quantum case by adding in a static loss pre-detector. We model this again via a beamsplitter with reflectivity $1-\gamma$, where γ is the quoted detector efficiency (see Eq. 5.23). Under this model, the measured transmission is defined as $\eta_m := \eta\gamma$. Following the same analysis as above, the FI on the measured transmission accounting for inefficient detection is given by the CRB:

$$F(\eta_m) = \frac{1}{\mathrm{Var}(\eta_m)}. \tag{5.31}$$

Using the formula $\mathrm{Var}(aX) = a^2\mathrm{Var}(X)$ gives:

$$F(\eta_m) = \frac{1}{\gamma^2\mathrm{Var}(\eta)}. \tag{5.32}$$

The FI on the measured transmission can be related to the FI on the linear coefficient via:

$$F(a) = \left(\frac{L\eta\gamma}{\gamma+\eta\kappa}\right)^2 \frac{\langle \hat{n}_{\mathrm{in}} \rangle^2}{\mathrm{Var}(\hat{n})}. \tag{5.33}$$

The superior performance in combination with resilience to saturation allows for probing with a Fock state at much weaker probe powers, without a compromise in performance. This enables a significant reduction in the energy flux incident upon the sample, even with imperfect detection. In Fig. 5.4 we quantify this reduction in required power for a given linear absorption coefficient and classical probe power κ_c. For a target absorption of $a = 1\,\mu\mathrm{m}^{-1}$ probed at $\kappa = 1$, assuming

85% efficient detection, employing the optimal quantum probe offers a reduction in probe brightness of −36 dB which has the potential to drastically reduce sample damage.

Returning to our example of DBT and accounting for a detector efficiency of 85%, if we allow the classical strategy to optimise its power such that $\kappa = 2.14$ as previously calculated, we find a possible power reduction factor of −3 dB available by switching to the optimal quantum probe without a compromise in precision.

State-of-the-art multiplexed single-photon sources are not yet bright enough to provide the required power to match performance with typical repetition rates of the order $\sim 10^6$ Hz[226]. Such a source would only begin to saturate samples with relaxation rates ~ µs, with typical biophysical relaxation rates ~ ns[227,228]. Although current single-photon sources lack the brightness to outperform classical probes, bright amplitude-squeezed states are readily available and are capable of approaching the limit on quantum performance.

5.2.6 Amplitude-squeezing: a viable route to enhanced performance

The precision gained from such a bright amplitude-squeezed state, $F_s(a)$, is given by:

$$F_s(a) = \left(\frac{L\eta}{1+\eta\kappa}\right)^2 \frac{\langle \hat{n}_{in} \rangle}{\eta^2 10^{-R/10} + \eta(1-\eta)} \tag{5.34}$$

where R is the input state's squeezing factor in dB, valid for bright amplitude-squeezing such that $|\alpha|^2 \gg R^2$[229]. Squeezed state performance is thus found to approach the quantum limit for infinite squeezing values, $F_s(a) \xrightarrow{R\to\infty} \mathcal{Q}(a)$. Fig. 5.4(b) shows squeezed state performance normalised by $\mathcal{Q}(a)$. A state-of-the-art squeezed vacuum source with 15 dB squeezing could be displaced to provide precision within 85% of the quantum limit and is almost unaffected by saturation effects for $\kappa \leq 4$[230]. We note that losses other than those caused by the target sample absorption, such as coupling losses or additional propagation losses, will dilute the squeezed statistics with vacuum noise, negatively affecting the state's performance. However, these results strongly indicate that advances can be made by employing squeezed states in the absence of bright Fock states.

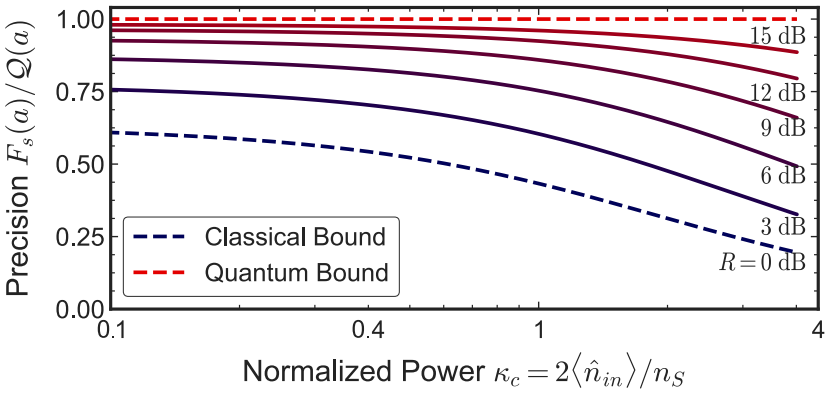

FIGURE 5.5. Squeezed state precision, $F_s(a)$, normalised by the quantum limit $\mathcal{Q}(a)$. The graph displaying the relative performance of several amplitude-squeezed states with squeezing factor R. Results have been plotted on a logarithmic x-axis. (Figure adapted from Ref.[190].)

5.3 A fully-quantum model of saturation

The results presented thus far have assumed a semi-classical model of saturation in which the effect on input state noise is not properly accounted for. We present a fully-quantum model of saturation as a quantum loss channel acting on the probe state. To allow for a fully-quantum simulation, the loss channel is discritise along its length z into slices each consisting of n_a absorbers. The optical probe state is then propagated through each slice, with photon number statistics extracted at each step to show how optical quantum noise is propagated along the sample. Each slice interacts for a time $\tau_{\text{int}} = dz/c$ where c is the speed of propagation through the sample. The model used is closely related to the Dicke model[231] for an open quantum system under Markovian evolution[232].

Though we account for both coherent and decoherent processes within our model, sensors that have not been specifically designed to operate coherently will be dominated by decoherent processes that result from spontaneous emission, variational atomic trajectories and inhomogeneous broadening across the ensemble. Since this is by far the most common type of dynamic seen in direct absorption schemes, we focus our discussion on this. Specifically we account for decoherence due to the spontaneous emission of each independent absorber at a rate $\Gamma_{\text{sp}} := 1/T_1$ to the environment and due to the dephasing at a rate $\Gamma_{\text{dp}} := 1/T_2$. Here, T_1 & T_2 are the characteristic energy and phase relaxation time scales of the specific absorber under consideration.

To solve for the evolution of the combined probe-sample system for a time τ_{int},

we first outline the governing Hamiltonian, $\hat{H}$, that applies to our model. Using open-system quantum modelling, we then numerically propagate this Hamiltonian through time allowing for spontaneous emission into the environment. We do not fully derive the Hamiltonian from first principles, instead we start with the standard Dicke Hamiltonian[231,233] which describes N-atoms resonantly interacting with a privileged optical mode. A full derivation of this Hamiltonian can be found in the following textbook by Walls and Milburn[234,235] which follows canonical quantisation of the classical electromagnetism Lagrangian. It is important to note that the Dicke Hamiltonian given below in Eq. 5.35 is derived under the following assumptions:

- **Density of particles & interaction frequency approximations:** a term quadratic in vector potential is considered negligible given that the absorbers are spaced at a distance greater than their Bohr radius and the the interaction frequency is greater than the Rydberg frequency.
- **Rotating wave approximation:** fast rotating terms within the Hamiltonian can be considered negligible over appreciable time scales.
- **Two-level system approximation:** each absorber can be considered to be a two level system fully described by a 2D Hilbert space.

The governing Hamiltonian is then found to be

$$\hat{H} = \hbar\omega\hat{a}^\dagger\hat{a} + \sum_{k=1}^{n_a}\left\{\hbar\omega\hat{\sigma}_k^\dagger\hat{\sigma}_k + g(\hat{a}\hat{\sigma}_k^\dagger + \hat{a}^\dagger\hat{\sigma}_k)\right\}. \tag{5.35}$$

Here, $\hat{\sigma}_k^\dagger$ is the excitation operator for the k^{th} absorber within the slice which has the form $\hat{\sigma}_k = |g\rangle\langle e|$ (these operators follow standard spin-1/2 algebra). $\hat{a}$ is the quantum oscillator probe field annihilation operator. The first term propagates the radiation field. The second term propagates n_a two-level systems (the absorbers). The third and fourth terms account for absorption and its reverse process, stimulated emission, at a rate determined by the single absorber-field interaction strength g. By assuming a homogeneous sample density and probe intensity, we can approximate each absorber to be equally coupled to the field which is considered to be resonant with the absorber transition frequency ω.

We assume each absorber to be well approximated by a charge pair with separation r. Under the dipole approximation, the electric field applied to each pole of the dipole can be considered to be equal. This assumption holds under resonant

probing with monochromatic light of wavelength λ where $r \ll \lambda$. The interaction strength g is then approximated by[235]:

$$g = \frac{\mu_{12} E}{\hbar}, \tag{5.36}$$

where μ_{12} is the dipole transition moment and E is the energy per photon within the interaction volume. There is some debate over the definition of E in free space, however, it is common practice to use the cavity based interaction definition where the volume V is now given by the interaction volume defined by the probe optical mode cross-section and duration. As such, E is given by[236]:

$$E = \sqrt{\frac{\hbar\omega}{2\epsilon_0 V}}. \tag{5.37}$$

The free space transition cross-section and spontaneous emission rates can be recast in terms of the dipole transition moment[237]:

$$\sigma = \frac{\pi\omega\mu_{12}^2}{3\epsilon_0\hbar c}, \tag{5.38}$$

$$\Gamma_{\text{sp}} = \frac{\omega^3\mu_{12}^2}{3\epsilon_0\pi\hbar c^3}. \tag{5.39}$$

We note that deriving the dephasing rate for a given system is much more complex and so is typically measured experimentally for a given setup and is often found to be orders of magnitude greater than g[238].

Following reference[239], we express the optical mode area $A = \pi r_{\text{focus}}^2$ in multiples of the wavelength $r_{\text{focus}} := \beta\lambda$. We normalise the interaction time τ_{int} by the absorber lifetime Γ_{sp} such that $\tau_{\text{int}} := \alpha/\Gamma_{\text{sp}}$. Using the following anzats for the interaction volume:

$$V = \pi\beta^2\lambda^2 c\tau_{\text{int}} \tag{5.40}$$

we can express the interaction rate as:

$$\frac{g}{\hbar\omega} = \sqrt{\frac{3}{2\alpha}}\frac{3}{\pi^2\beta}. \tag{5.41}$$

Crucially, in the free space model, the coupling strength is dependent on the interaction time through the parameter α. Note that in this model we do not include the saturation intensity n_s as this only arises in the semi-classical model as a direct result of the constraint that only one photon may be absorbed per cross-section per transition lifetime. Here, this is already built into the Hamiltonian. As mentioned above, the strategy will be to use this model to propagate the probe through each i^{th} sample slice of width dz.

The probe-sample Hilbert space is given by the tensor product of the single optical mode with the n_a two-level absorbers. The input density matrix of the 1st slice is given by:

$$\rho_1(0) = |\psi_1(0)\rangle \langle\psi_1(0)| \otimes |0^k\rangle \langle 0^k| \tag{5.42}$$

where the optical input state $|\psi_1(0)\rangle \in \{|\alpha\rangle, |N\rangle\}$ is either a Fock state or a coherent state with mean photon number $\langle \hat{n}_{\text{in}} \rangle$. The absorbers are assumed to initially be in the ground state.

5.3.1 Open-systems modelling

So far we have considered a closed system Hamiltonian that describes the probe-sample system and its coherent dynamics. Now we expand on this model to account for spontaneous emission and dephasing to the environment.

Open-system quantum modelling is a powerful tool to describe the non-unitary evolution of a system's density matrix by considering the system as a sub-space of a larger system-environment Hilbert space which undergoes unitary evolution. Under certain assumptions (listed below) about the nature of the interaction with the environment, the environment can be traced out leaving a equation of motion for the systems density matrix. In general, the governing equation is coined the *master equation*. Here, we employ the Linbladian form of the master equation, derived fully in[240]. The Linbladian master equation is a completely positive trace preserving map which evolves the system density matrix under the following Markovian assumptions:

- **Separability:** at $t = 0$ there exsists no correlations between the probe-sample system and the environment.

- **Born approximation:** (1) the interaction with the probe-sample system does not significanly alter the state of the environment during the interaction; (2) the combined density matrix of the environment and probe-sample system remain separable throughout the interaction.

- **Markov approximation:** the environment can be considered static i.e. the environment time-scale is much shorter than the probe-sample system interaction time.

Under these assumption, the Linbladian master equation is given by:

$$\frac{\partial \rho_i(t)}{\partial t} = -i[\hat{H}, \rho_i(t)] + \sum_i \left(\hat{L}_i \rho_i(t) \hat{L}_i^\dagger - \frac{1}{2}\{\hat{L}_i^\dagger \hat{L}_i, \rho_i(t)\} \right) \tag{5.43}$$

where $\hat{L}_i$ are the so-called collapse operators which describe the non-Hermitian loss of energy to the environment. For an intuitive derivation of this equation, we point the reader towards Ref.[232]. Within our model, we have the following two collapse operators,

$$\begin{aligned} \hat{L}_1 &= \sqrt{\Gamma_{\text{sp}}}\,\hat{\sigma}, \\ \hat{L}_2 &= \sqrt{\Gamma_{\text{dp}}}\,\hat{\sigma}_z, \end{aligned} \tag{5.44}$$

for each absorber. $\hat{L}_1$ accounts for spontaneous emission of each absorber to the environnement. $\hat{L}_2$ is proportional to the Pauli-z dephasing operator and accounts for the dephasing of each absorber. Inserting Eq. 5.35 and Eq. 5.44 into Eq. 5.43 gives:

$$\begin{aligned} \frac{\partial \rho_i(t)}{\partial t} = -i\Big[\hat{a}^\dagger \hat{a} + \sum_{k=1}^{N_a} \left\{ \hat{\sigma}_k^\dagger \hat{\sigma}_k + g(\hat{a}\hat{\sigma}_k^\dagger + \hat{a}^\dagger \hat{\sigma}_k), \rho_i \right\} \Big] \\ + \Gamma_{\text{sp}} \sum_{k=1}^{N_a} \left(\hat{\sigma}_k \rho_i \hat{\sigma}_k^\dagger - \frac{1}{2}\{\hat{\sigma}_k^\dagger \hat{\sigma}_k, \rho_i\} \right) \\ + \Gamma_{\text{dp}} \sum_{k=1}^{N_a} \left(\hat{\sigma_z}_k \rho_i \hat{\sigma_z}_k^\dagger - \frac{1}{2}\{\hat{\sigma_z}_k^\dagger \hat{\sigma_z}_k, \rho_i\} \right). \end{aligned} \tag{5.45}$$

Note we have switched to natural units in which $\hbar \equiv 1$ and $c \equiv 1$, we also set $\omega = 1$ such that $\lambda = 2\pi$. This is for convenience and does not effect the physics. We solve this equation numerically via the open-source software QuTip [169,241]. After propagating the system for a time τ_{int}, we perform a partial trace over the absorbers Hilbert space to extract the optical state's density matrix:

$$|\psi_i(\tau_{\text{int}})\rangle \langle \psi_i(\tau_{\text{int}})| = \text{tr}_{n_a}\{\rho_i(\tau_{\text{int}})\}. \tag{5.46}$$

This state is then coupled forward as the input state of the $i+1^{\text{th}}$ slice and the algorithm is thus repeated for the full length of the sample:

$$\hat{\rho}_{i+1}(0) = |\psi_i(\tau_{\text{int}})\rangle \langle \psi_i(\tau_{\text{int}})| \otimes (|0^k\rangle \langle 0^k|). \tag{5.47}$$

At each step, we use the optical states density matrix to solve for the photon number statistics, comparing it directly with that predicted by a linear loss channel.

For the purpose of this investigation we set $\tau_{\text{int}} = 1$ and assume $\alpha = 0.5$ such that the interaction time is half the transition relaxation time. This allows saturation to take effect during the interaction. When focusing close to the diffraction

limit, the coupling constant can no longer be considered the same for each absorber due to the state's polarisation becoming non uniform[242]. We therefore consider a maximal focusing of $\beta = 10$. This gives an interaction rate $g = 0.1$ in natural units. We set the dephasing rate to be $\Gamma_{\text{dp}} = 2$ such that decoherence dominates the evolution with $\Gamma_{\text{dp}} \gg g, \Gamma_{\text{sp}}$. The model can be used to recreate the famous optical Bloch equations under a classical probe approximation which describe the evolution of an ensemble of absorbers coupled to a classical coherent field[243]. Here, we will use the model to probe the intensity profile along a sample consisting of 20 slices. To enable full simulation of the Hilbert space $n_a = 4$ for each slice and we probe with an optical state consisting of $\langle \hat{n}_{in} \rangle = 12$ input photons. Despite the simplicity of this model, we can use it to lend insight into how probing a loss channel above saturation effects quantum noise in the probe state.

5.3.2 A comparison to the semi-classical model

To compare the two models, we plot the evolution of the probe state's Fano factor – the variance-to-mean ratio of the photon number probability distribution – defined as $\mathbf{F} := \langle \hat{n} \rangle / \text{Var}(\hat{n})$, for classical (Fig. 5.6(a)) and Fock (Fig. 5.6(b)) input states.

As the state propagates along the sample, the photon number distribution evolves according to the effective loss applied to each component number state. In the fully-quantum model, this effective loss is dependent on the number of photons in each basis state and is therefore different for each component of the distribution. By comparison, the semi-classical model assumes the effective loss is the same for all component number states and is dependent only on the mean photon number. The overall effect of accounting for the differential effective loss across the distribution is to increase or decrease the photon number variance in comparison to the semi-classical approximation, as is the case with all nonlinear processes.

We find that the addition of noise to the Fock state is suppressed in comparison to the semi-classical model whilst the probe intensity remains above saturation. During a saturated interaction only n_a photons may be absorbed per interaction time which suppresses the rate at which noise, through loss, is added to the state. $F_f(a)$ is therefore underestimated for output powers $\kappa \geq 1$. For coherent state propagation, saturation increases the optical noise due to a differential effective absorption rate across the state's photon number distribution. This acts to stretch the Poissonian photon number statistics such that the probe be-

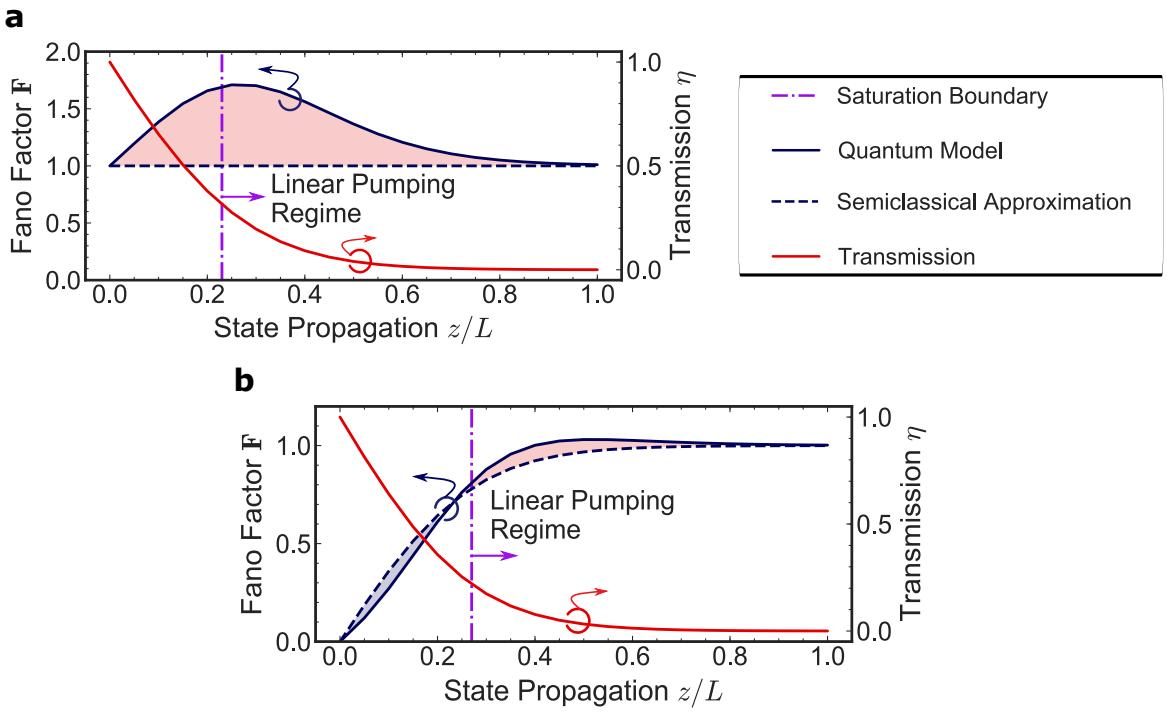

FIGURE 5.6. Coherent (a) and Fock (b) state evolution along a saturable sample. We plot the evolution of the probe state's Fano factor **F** (blue) and transmission η (red) comparing the fully-quantum model (solid blue) to the semi-classical approximation (dashed blue). Shaded red represents additional noise and shaded blue represents suppressed noise. The dot-dashed purple line is the point along the channel at which the number of photons present in the probe state drops below n_a. (Figure adapted from Ref.[190].)

comes super-Poissonian. We therefore conclude that $F_c(a)$ presented under the semi-classical approximation is an upper bound on the true classical state performance. Consequently, the quantum advantage given by Eq. 5.30 is a lower bound on the true quantum advantage under saturated probing.

In alignment with the results presented by Kumar *et al.* in Ref. [244], the semi-classical approximation for classical sensing experiments is sufficient when the mean photon number of the state remains one standard deviation above or below the saturation intensity during the analyte-probe interaction. This ensures that the effective absorption strength across the states poissonian photon number statistics is well approximated by its mean value, minimising the effect of the nonlinearity on the states statistics.

5.4 Conclusion

We have explored the damaging effects of saturation on absorption spectroscopy precision. These results are of most importance to saturation-limited classical measurements demanding greater precision or efficiency such as those often performed in high-precision absorption spectroscopy experiments[214,215]. We have proven Fock states are optimal for mitigating the limiting effects of saturation and, through performance comparison, have shown classical schemes probing weak absorptions stand to gain the most from a quantum upgrade[191–193]. For schemes that do not have access to quantum resources we present a classical sample-probe optimisation strategy to help improve performance with minimal experimental adaptation. Further, we have shown that in the absence of bright Fock states, state-of-the-art squeezed states provide an effective alternative to overcoming saturation with today's technology. Whilst the analysis here finds saturation to be a detrimental effect on standard absorption spectroscopy, there are a number of more advanced techniques, such as stimulated depletion microscopy[202] or saturated structured-illumination microscopy[245], where saturation is used as a tool to enhance the information gained on a sample. Adapting the analysis here to optimise the performance of these strategies and to investigate any potential quantum advantages may lead to further enhancement of these optical sensors.

Chapter 6

Conclusion

The work presented in chapter 3 presents a state-of-the-art 2 µm homodyne detector. The device was purpose built for enabling pulse squeezing measurements and is sufficient for future measurements of squeezing with a reasonable total efficiency of 57%, far above any previous demonstration. Shot-noise limited detection at megahertz speeds will support the future development of both integrated and off-chip squeezed states in the 2 µm-band. The bandwidth of the device presented here, though currently limited by the performance of the op-amp and parasitic capacitance on the input of the op-amp, is also sufficient to enhance the signal-to-noise ratio of classical absorption sensing schemes that modulate information into megahertz sidebands[69] or that employ balanced detection to reject classical laser noise[71,109].

Chapter 4 presents an attempt at integrated classical noise reduction, via a device that was originally intended to provide sub-classical noise suppression of a pulsed 2 µm laser. We note the work in this chapter, along with the characterisation of noise in the pulsed laser presented at the end of chapter 3, was enabled by the detector developd in chapter 3 proving the device's utility. We conclude the scheme does suppress noise but in addition to added noise from unwanted modulation instability present in the waveguide. This effect can be countered by switching to a normal dispersive geometry. We also discuss barriers to sub-classical noise suppression and conclude the main barriers to a squeezing result to be limited integrated beamsplitter extinction and excess classical laser noise. The former could be overcome in future rounds of PIC development via low-loss, broadband, integrated MZI design such as the one utilised in Ref.[246].

In chapter 5 we asses the effect of saturation on the performance of classical and nonclassical states of light used to probe absorption. Under a semi-classical approximation, we derive a bound on precision and prove Fock states optimal. Squeezed states are presented as a viable route towards experimental realisation. A fully quantum model is presented and we find the analytical quantum advantage to be a lower bound on the actual advantage. The analytic formulae derived in this chapter can be directly applied to classical, shot-noise limited, spectroscopy measurements[214] to help optimised measurement precision. Furthermore, the intuition gained about the obtainable quantum advantage for high-power, saturation-limited, spectroscopy measurements, will prove useful for those looking to preform a cost-benefit analysis of switching to a squeezed state probe.

6.1 In pursuit of integrated 2 μm squeezing for absorption sensing

Since the start of this PhD, integrated silicon squeezing, even in the well supported telecoms band, has proven elusive. The field of integrated telecoms squeezing has pivoted away from pulsed Kerr-interferometers in silicon and towards resonator-based four-wave mixing in silicon nitride[160,161]. A key benefit of this switch is the fact that greater amounts for squeezing are obtainable from resonators than from pulsed Kerr-interferometery[160]. Additional benefits include continuous-wave operation, no two-photon absorption, ultra-low loss waveguides, and silicon integration via multi-platform fabrication capabilities that enable silicon to silicon nitride coupling on the same chip.

At 2 μm, silicon resonator squeezing still holds promise with most of these benefits gained not from a change of platform but by a shift in photon energy. The scheme is dependent on the availability of 2 μm continuous-wave lasers and high power EDFAs which have now become commercially available. A downside of switching to a continuous-wave source is the need for faster (~ 100 MHz) detection electronics. As discussed in chapter 3, this presents a significant problem at 2 μm.

A potential solution is to utilise a bichromatic local oscillator (BLO) homodyne detection scheme[247]. In this adapted homodyne detection scheme, the LO consists of two coherent frequencies at symmetric sidebands to the original carrier. It can be proven that using such an LO maps quadrature statistics from the

LO sideband frequency to DC enabling the signal to be probed about the LO sideband frequency. Adopting acusto-optic or phase modulation techniques, it is then possible to create a BLO at a sideband frequency faster than the bandwidth of the detector presented in chapter 3, thereby increasing the overall bandwidth of the measurement.

6.2 An outlook on integrated absorption sensing in the MIR

The dense number of absorption features in the fingerprint region creates difficulties in the distinguishability and selectivity of target analytes from background features. These difficulties can be mitigated to some extent by additonal reference signals[248] or sample pre-processing, however, both of these methods can come with significant cost to measurement speed or deployability. Wavelength resolution is by far the best solution and, in the absence of nonlinear optics techniques, is often provided by one of three main solutions: 1) a tuneable laser source, 2) a broadband laser with either a multichannel or filter-based spectrometer, or 3) a broadband laser & tuneable filter combination.

Option 1, requiring only one detection channel, is by far the simplest to design, however, integrated tuneable lasers are often an order of magnitude more expensive than broadband lasers. Option 2 shifts the complexity onto the design of integrated spectrometers, such as AWGs[249], which are notoriously difficult to design to a high specification and which can have costly footprints. Additionally, the scheme requires multiple detectors or a line-scanning detector with measurement sensitivity likely to be limited by detection electronics as advanced methods such as balanced detection[71] become untenable. Option 3 requires a tuneable filter with a working bandwidth on the order of GHz or less to be able to resolve single transitions. A fourth option is to exploit the superior nonlinear optics capabilities afforded by integrated platforms, such as silicon, to craft functional multi-wavelength probes, such as frequency combs[250]. Edge emitting quantum cascade lasers available in this part of the spectrum can be integrated into a monolithic device to power comb generation[251]. The ability to generate integrated frequency combs provides integrated optical gas sensors a competative edge over other promising scalable and deployable, non-optical, gas sensing technologies such as semiconductor metal oxide sensors[252] or calorimetric sensors[253].

A key issues faced by integrated optical gas sensors is limited probe-analyte

overlap which often bounds the limit of detection for a given probe power. High probe confinement achieved by high index contrast materials, whilst conducive to nonlinear phenomena, hinders analyte-probe overlap with the majority of power concentrated inside the waveguide. Solutions to enhance analyte-probe interactions make use of the additional benefits of integrated optics, namely the ability to engineer sub-wavelength structures and the ability to engineer the oxide of local regions of the chip. These capabilities have been used to slow the probe down, providing a strong enhancement factor[254].

Classical integrated sensing schemes using silicon PICs have begun to bring together key components onto the same chip to exploit multi-wavelength or modulation-enhanced absorption techniques. Wang *et al.* presents a silicon PIC consisting of a tunable laser sources, detectors and waveguide circuits with propagation losses of ~0.5 dB/cm which enable spectrometry via an arrayed waveguide grating centred on 2.3 µm range[44]. As the field of integrated silicon absorption sensing grows at 2 µm, low frequency intensity noise in both high power pulsed lasers and continuous-wave lasers will become more of a pressing issue that limits measurement precision. While active noise suppression technology and shot-noise limited lasing is developd in industry, we look to passive noise suppression methods[50] and modulation-enhanced sensing schemes[255] to circumvent this noise.

In rudimentary demonstrations of integrated gas sensing, sensitivity is limited by the need for stability across two consecutive measurements—a reference measurement and a signal that passes through the gas. In the 2 µm–band, a promising solution is to utilise recently developd fast modulation in silicon to modulate absorption information out to higher frequencies[256]. Modulation speeds are then limited by detection bandwidths which are set to gain from the integration of photodiodes[41,257]. A key barrier to this will be the adoption rate of detector materials, such as GaInAsSb, responsive at 2 µm by fabrication houses.

6.3 Closing remarks

In closing, the field of integrated absorption sensing in the 2 µm-band faces some significant engineering challenges to provide competative sensing devices, however, as we have discussed above, encouraging progress is being made on these challenges that should place integrated silicon devices at the forefront of the gas sensing industry in the years to come.

We have seen in this thesis that integrated silicon devices specifically are not only suitable for 2 µm-band classical sensing but are also well suited to quantum enhancement through squeezed state production. As 2 µm laser technology catches up to telecoms standards, we can utilise the same properties that afford squeezing to suppress classical laser noise and thereby improve the measurement precision of both linear and saturation-limited absorption schemes. Guided by the characterisation of noise enabled by the detector presented here, the field can continue to leverage PIC technology to develop low noise states in the hope of one day applying them in a commercially viable monolithic package that represents the cutting-edge of optical sensing in the 2 µm-band.

Appendix

List of symbols

Constants		
Electron charge	e	$1.60\text{x}10^{-19}$ C
Speed of light	c	$3.00\text{x}10^{8}$ m/s
Reduced Planck's constant	$\hbar$	$1.06\text{x}10^{-34}$ Js
Bolzmann's constant	k	$1.38\text{x}10^{-23}$ $\text{m}^2\text{kgs}^{-2}\text{K}^{-1}$
Vacuum permitivity	ϵ_0	$8.85\text{x}10^{-12}$ F/m
Magnetic constant	μ_0	$1.38\text{x}10^{-6}$ H/m
Functions		
Delta function	$\delta(x)$	
Leguerre polynomial functions	$L_n[x]$	$\sum_{k=0}^{n} \frac{n!}{k!(n-k)!} \frac{(-1)^k}{k!} x^k$
Transverse mode distribution	$F(x,y)$	
Wigner function	$W(x,p)$	
Kronecker delta function	δ_{ij}	
Square indentity matrix	I_M	
Square zero matrix	0_M	
Lambert-W function	$W(x)$	$W(ze^z) \equiv z$
Wright Omega function	$\mathcal{W}(x)$	$W(e^z) \equiv \mathcal{W}(z)$
Electrodynamics		
Electric field	$\mathbf{E}(\mathbf{r},t)$	[V/m]
Magnetic field	$\mathbf{B}(\mathbf{r},t)$	[T]
Vector field	$\mathbf{A}(\mathbf{r},t)$	[Vs/m]
Frequency	f	[Hz]

Wavelength	λ	$[\mathrm{m}]$
Angular frequency	ω	$2\pi f$ $[\mathrm{rad/s}]$
Wave number	k	$2\pi/\lambda$ $[\mathrm{m}^{-1}]$
Refractive index	n	
Polarisation vector	$\mathbf{e}^{\lambda}$	$\{\mathbf{x}, \mathbf{y}\}$
Volume	V	$[\mathrm{m}^3]$
Characteristic dispersion length	L_{D}	$[\mathrm{m}]$
Nonlinear Optics		
Polarisation field	$\mathbf{P}(\mathbf{r}, t)$	$\epsilon_0 \chi \mathbf{E}$
Electric susceptability	χ	$n^2 - 1$
Third order susceptability	$\chi^{(3)}$	
TPA coefficient	β_{TPA}	$[\mathrm{m/W}]$
Nonlinear refractive index	n_2	$3\chi^{(3)}/4n_1^2\epsilon_0 c$ $[\mathrm{m}^2/\mathrm{W}]$
Permitivity	ϵ	$1 + \chi$
Nonlinear parameter	ϕ_{NL}	$\omega n^2/cA_{\mathrm{eff}}$ $[1/\mathrm{Wm}]$
Characteristic nonlinear length	L_{NL}	$[\mathrm{m}]$
Integrated Optics		
Waveguide length	L	$[\mathrm{m}]$
Core refreactive index	n_{core}	
Cladding refreactive index	n_{clad}	
Effective index	n_{eff}	
Effective propagation constant	β	$n_{\mathrm{eff}} 2\pi/\lambda$ $[1/\mathrm{m}]$
Effective mode area	A_{eff}	$[\mathrm{m}^2]$
Group velocity	v_g	$[\mathrm{m/s}]$
Group velocity dispersion	β_2	$[\mathrm{s}^2/\mathrm{m}]$
Dispertion parameter	D	$-s\pi c\beta_2/\lambda^2$ $[\mathrm{ps/nmkm}]$
Propagation loss	α_L	$[\mathrm{dB/cm}]$
Thermo-optic coefficient	$\partial n/\partial T$	$[1/\mathrm{K}]$
Tempurature	T	$[\mathrm{K}]$
Odd supermode index	n_{odd}	
Even supermode index	n_{even}	
Angle of incidence	θ_i	
50:50 coupling length	L_{50}	
Interference visibility	V	
Beamsplitter transmission	η	
Propagation loss correlation function	$R(u)$	

Correlation length	L_c	[m]
Sidewall roughness mean squared deviation	g	[m]
Waveguide width	w	[m]
Waveguide heigth	h	[m]
Single-mode Quantum Optics		
Generic state	$\|\psi\rangle$	
Creation operator	$\hat{a}$	
Annihilation operator	$\hat{a}^\dagger$	
Hamiltonian	$\hat{H}$	
Eigen-enegry	E_n	
Photon number	N	
Number operator	$\hat{n}$	
Amplitude quadrature operator	$\hat{x}$	$(\hat{a}+\hat{a}^\dagger)/2$
Phase quadrature operator	$\hat{p}$	$i(\hat{a}^\dagger-\hat{a})/2$
Quadrature operator	$\hat{q}$	$\hat{a}e^{i\phi}+\hat{a}^\dagger e^{-i\phi}$
Squeezing factor	r	
Squeezing angle	θ	
Squeeze parameter	ξ	$re^{i\theta}$
Squeezing operator	$\hat{S}(\xi)$	
Coherent amplitude	α	
Coherent state phase	ϑ	
Coherent state	$\|\alpha\rangle$	
Fock state	$\|n\rangle$	
Coherent squeezed state	$\|\alpha,\xi\rangle$	
Unitary Kerr operator	$\hat{U}_\mathrm{K}$	
Kerr state	$\|\alpha\rangle_\mathrm{K}$	$\hat{U}_\mathrm{K}\|\alpha\rangle$
Electronics		
Bias voltage	V_b	[V]
Supply voltage	V_s	[V]
Inverting input voltage	V_-	[V]
Non-inverting input voltage	V_+	[V]
Op-amp open gain	A_0	
Op-amp output voltage	V	[V]
Photodiode shunt resistance	R_shunt	[Ω]
Photodiode junction capacitance	C_pd	[F]
Op-amp capacitance	C_oa	[F]

Feedback capacitance	C_f	[F]
Freedback resistance	R_f	[Ω]
Impedance	z	[Ω]
Op-amp gain bandwidth product	$A_0 f_0$	[Hz]
Dark current shot noise	$\langle I_d \rangle$	$[\mathrm{A}/\sqrt{Hz}]$
Voltage supply noise	$\langle V_{\mathrm{reg}} \rangle$	$[\mathrm{A}/\sqrt{Hz}]$
Op-amp voltage noise	$\langle V_{oa} \rangle$	$[\mathrm{V}/\sqrt{Hz}]$
Op-amp current noise	$\langle I_{oa} \rangle$	$[\mathrm{A}/\sqrt{Hz}]$
Total current noise	$\langle I_{oa}^{tot} \rangle$	$[\mathrm{A}/\sqrt{Hz}]$
Saturation power	P_{sat}	[W]
Noise equivalent power	P_{nep}	[W]
Peak-to-peak voltage	V_{pp}	[V]
Detector unit response function	$r(t)$	
Photodiode responsivity	$\mathscr{R}$	[A/W]
Homodyne Detection		
LO field operator	$\hat{A}_{\mathrm{LO}}$	
LO field mean value	A_{LO}	
LO field time-dependent quantum noise operator	$\hat{a}_{\mathrm{LO}}$	
LO amplitude	α_{LO}	
LO phase	ϕ	
Signal amplitude	α_{s}	
Signal field mean value	A_{s}	
Signal field time-dependent quantum noise operator	$\hat{a}_{\mathrm{s}}$	
Signal field operator	$\hat{A}_{\mathrm{s}}$	$A_{\mathrm{s}} + \hat{a}_{\mathrm{s}}$
Time-dependent signal quadrature	$\hat{q}_{s,\phi}(t)$	
Photocurrent operator	$\hat{I}(t)$	
Detector noise operator	$\hat{I}_d(t)$	
Target time-independent quadrature	$\hat{Q}_{\mathrm{targ}}$	
Single pulse quadrature	$\hat{Q}_{\mathrm{p}}$	
Time-independent detected quadrature	$\hat{Q}$	
Quadrature integration weighting function	$\Phi(t)$	
Photodiode coupling efficiency	η_c	
Photodiode quantum efficiency	η_{QE}	
Detector SNR efficiency	η_{SNR}	
Total detector efficiency	η_{tot}	
ESA resolution bandwidth	B	[Hz]

Radio/sideband frequency	Ω	[Hz]
ESA PSD	$\langle \hat{p}_\Omega \rangle$	[W]
Noise suppression modelling		
Pulse envelope temporal discretisation index	j	
Number of discritisation modes	M	
Temporal discretisation spacing	$\Delta\tau$	
Propagation length discritisation spacing	Δz	[m]
j-th mean field value	$A(z)_j$	
j-th slice quantum fluctuation operator	$\hat{a}_j(z,t)$	
Quantum fluctuation decomposition matracies	$\mu(z), \nu(z)$	
Classical stochastic functions	$s_j(z,t)$	
Orthognal classical stochastic basis functions	ζ_j	
Level of classical noise above shot noise	σ	
DC signal component	Φ	
Relative intensity noise	RIN	
Modulation instability gain spectrum	G_{MI}	
Peak laser power	P_p	[W]
Saturation modelling		
Ground state occupation number	n_0	
Excited state occupation number	n_1	
Total number of absorbers	n_t	
Absorption cross section	σ	[1/m]
Excited state lifetime	τ	s
Saturation intensity	n_s	
Linear absorption coefficient	a	[1/m]
Normalised intensity	κ	
Optimal intensity	n_{opt}	
Fisher information	$F(x)$	
Coherent state fisher information	$F_c(x)$	
Squeezed state fisher information	$F_s(x)$	
Quantum advantage	$\Lambda(x)$	
Spontaneous emission rate	Γ_{sp}	[Hz]
Dephasing rate	Γ_{sp}	[Hz]
Single-atom interaction rate	g	[J]
Dipole transition moment	μ_{12}	[]
Collapse operators	$\hat{L}_{1,2}$	

Appendix B

Key specifications & parameters

Here, we list all relevant specifications for the pulsed laser used in Chapters 3 & 4, alongside key parameters of the Cornerstone devices investigated in Chapter 4.

B.1 Pulsed laser specifications

Table B.1. A list of 2 µm pulsed laser specifications.

Property	Value
Central wavelength λ_0	2.07 µm
Bandwidth $\Delta\lambda$	2.6 nm
Max average power	17 dBm
Repetition rate R_{rep}	39.5 MHz
Pulse width $\Delta\tau$	2.8 ps
Pulse shape	$\approx \text{sech}^2$
Coupling type	free space
Gain medium	Thulium/Holmium
Laser type	passive mode-locked
Model number	AdValue Photonics AP-ML-1

B.2 Cornerstone device parameters

TABLE B.2. A list of Cornerstone device specifications.

Property	Value
Platform	silicon-on-silicon dioxide
Fabrication method	optical lithography
Technology	passive with heaters (TiN)
Silicon height	340 nm
TOX/BOX thickness	1 µm/2 µm
Heater sheet resistance	10 Ω/□
Single-moded strip waveguide width @ 2.07 µm	500 n
Strip effective modal area A_{eff} @ 2.07 µm	0.39 μm^2
Strip waveguide effective index @ 2.23 µm	2.12
Group velocity v_g @ 2.07 µm	0.7x10^8 m/s
Group velocity dispersion D @ 2.07 µm	5.28x10^{-4} s/m^2
Thermo-optic coefficient of silicon	1.7x10^{-4} K^{-1}
Nonlinear refractive index @ 2.07 µm n_2	1.5x10^{-18} m^2/W

References

[1] Ferreira, M. F. S. *et al.* Roadmap on optical sensors. *Journal of Optics (2010)* **19**, 083001 (2017). ⟨1⟩.

[2] Dirac, P. A. M. & Bohr, N. H. D. The quantum theory of the emission and absorption of radiation. *Proceedings of the Royal Society of London. Series A, Containing Papers of a Mathematical and Physical Character* **114**, 243–265 (1927). ⟨1⟩.

[3] Cohen-tannoudji, C. & Guery-odelin, D. *Advances In Atomic Physics: An Overview* (World Scientific, 2011). ⟨1⟩.

[4] Pradhan, A. K. & Nahar, S. N. *Atomic Astrophysics and Spectroscopy* (Cambridge University Press, 2011). ⟨1⟩.

[5] Ozaki, Y., Wójcik, M. J. & Popp, J. *Molecular Spectroscopy, 2 Volume Set: A Quantum Chemistry Approach* (John Wiley & Sons, 2019). ⟨1⟩.

[6] Ciurczak, E. W. & Igne, B. *Pharmaceutical and Medical Applications of Near-Infrared Spectroscopy, Second Edition* (CRC Press, 2014). ⟨1⟩.

[7] Clark, R. J. H. & Hester, R. E. *Spectroscopy in Environmental Science* (Wiley, 1995). ⟨1⟩.

[8] Chen, W., Venables, D. S. & Sigrist, M. W. *Advances in Spectroscopic Monitoring of the Atmosphere* (Elsevier, 2021). ⟨1⟩.

[9] All Nobel Prizes in Physics. https://www.nobelprize.org/prizes/lists/all-nobel-prizes-in-physics. ⟨1⟩.

[10] Scotter, C. Use of near infrared spectroscopy in the food industry with particular reference to its applications to on/in-line food processes. *Food Control* **1**, 142–149 (1990). ⟨1⟩.

[11] Sahni, N. S., Isaksson, T. & Næs, T. In-line near infrared spectroscopy for use in product and process monitoring in the food industry. *Journal of Near Infrared Spectroscopy* **12**, 77–83 (2004).

[12] Smidt, E. & Schwanninger, M. Characterization of waste materials using ftir spectroscopy: Process monitoring and quality assessment. *Spectroscopy Letters* **38**, 247–270 (2005).

[13] Lackner, M. Tuneable diode laser absorption spectroscopy in the process industries - a review. *Reviews in Chemical Engineering* **23**, 65–147 (2007).

[14] Farooq, A., Jeffries, J. & Hanson, R. CO2 concentration and temperature sensor for combustion gases using diode-laser absorption near 2.7 um. *Applied Physics B* **90**, 619–628 (2008). ⟨1⟩.

[15] Elrod, M. J. Greenhouse Warming Potentials from the Infrared Spectroscopy of Atmospheric Gases. *Journal of Chemical Education* **76**, 1702 (1999). ⟨1⟩.

[16] Restieri, R., Gagliardi, G., Biasio, G. D., Cotrufo, F. & Gianfrani, L. High-precision measurements of CO2 concentration in air by means of diode-laser absorption spectroscopy near 2 um. In *Water, Ground, and Air Pollution Monitoring and Remediation*, vol. 4199, 124–129 (SPIE, 2001).

[17] Ismail, S. *et al.* Development of a Ground-based 2-Micron Differential Absorption Lidar System to Profile Tropospheric CO2.

[18] Cui, X. *et al.* Photonic sensing of the atmosphere by absorption spectroscopy. *Journal of Quantitative Spectroscopy and Radiative Transfer* **113**, 1300–1316 (2012). ⟨1⟩.

[19] Du, C. & Zhou, J. Evaluation of soil fertil-

ity using infrared spectroscopy – a review. In Lichtfouse, E. (ed.) *Climate Change, Intercropping, Pest Control and Beneficial Microorganisms: Climate Change, Intercropping, Pest Control and Beneficial Microorganisms*, Sustainable Agriculture Reviews, 453–483 (Springer Netherlands, Dordrecht, 2009). ⟨1⟩.

[20] Massie, C., Stewart, G., McGregor, G. & Gilchrist, J. R. Design of a portable optical sensor for methane gas detection. *Sensors and Actuators B: Chemical* **113**, 830–836 (2006).

[21] Chagunda, M. G. G. Opportunities and challenges in the use of the Laser Methane Detector to monitor enteric methane emissions from ruminants. *Animal* **7**, 394–400 (2013). ⟨1⟩.

[22] Henderson, B. *et al.* Laser spectroscopy for breath analysis: Towards clinical implementation. *Applied Physics B: Lasers and Optics* **124**, 1–21 (2018). ⟨1⟩.

[23] Selvaraj, R., Vasa, N. J., Nagendra, S. M. S. & Mizaikoff, B. Advances in mid-infrared spectroscopy-based sensing techniques for exhaled breath diagnostics. *Molecules* **25**, 2227 (2020). ⟨1⟩.

[24] Hänsel, A. & Heck, M. J. Opportunities for photonic integrated circuits in optical gas sensors. *JPhys Photonics* **2**, 012002–012002 (2020). ⟨2⟩.

[25] Liu, X. *et al.* A survey on gas sensing technology. *Sensors* **12**, 9635–9665 (2012). ⟨2⟩.

[26] Gordon, I. *et al.* The HITRAN2020 molecular spectroscopic database. *Journal of Quantitative Spectroscopy and Radiative Transfer* **277**, 107949 (2022). ⟨2⟩.

[27] Supplee, J. M., Whittaker, E. A. & Lenth, W. Theoretical description of frequency modulation and wavelength modulation spectroscopy. *Applied Optics* **33**, 6294–6302 (1994). ⟨2, 64⟩.

[28] Silver, J. A. Frequency-modulation spectroscopy for trace species detection: Theory and comparison among experimental methods. *Applied Optics* **31**, 707–717 (1992). ⟨64⟩.

[29] Lins, B., Zinn, P., Engelbrecht, R. & Schmauss, B. Simulation-based comparison of noise effects in wavelength modulation spectroscopy and direct absorption TDLAS. *Applied Physics B: Lasers and Optics* **100**, 367–376 (2010). ⟨2⟩.

[30] Paul, J. B. *et al.* Infrared cavity ringdown and integrated cavity output spectroscopy for trace species monitoring. In *Vibrational Spectroscopy-based Sensor Systems*, vol. 4577, 1–11 (SPIE, 2002). ⟨2⟩.

[31] Baer, D., Paul, J., Gupta, M. & O'Keefe, A. Sensitive absorption measurements in the near-infrared region using off-axis integrated-cavity-output spectroscopy. *Applied Physics B* **75**, 261–265 (2002). ⟨2⟩.

[32] Hu, T. *et al.* Silicon photonic platforms for mid-infrared applications [Invited]. *Photonics Research* **5**, 417–417 (2017). ⟨2⟩.

[33] Shimura, F. *Semiconductor Silicon Crystal Technology* (Elsevier, 2012). ⟨2⟩.

[34] Wang, J., Sciarrino, F., Laing, A. & Thompson, M. G. Integrated photonic quantum technologies. *Nature Photonics* **14**, 273–284 (2020). ⟨3⟩.

[35] Miller, S. A. *et al.* Low-loss silicon platform for broadband mid-infrared photonics. *Optica* **4**, 707–707 (2017). ⟨3⟩.

[36] Rosenfeld, L. M. *Mid-Infrared Quantum Optics in Silicon: Light Work Wiith Long Waves*. Ph.D. thesis, University of Bristol (2019). ⟨3, 4, 5, 24, 26, 27, 78, 80, 84, 85⟩.

[37] Weng, B. *et al.* Room temperature mid-infrared surface-emitting photonic crystal laser on silicon. *Applied Physics Letters* **99**, 221110 (2011). ⟨3⟩.

[38] Rahim, M. *et al.* Mid-infrared PbTe vertical external cavity surface emitting laser on Si-substrate with above 1 W output power. *Applied Physics Letters* **95**, 1–4 (2009).

[39] Fill, M., Khiar, A., Rahim, M., Felder, F. & Zogg, H. PbSe quantum well mid-infrared vertical external cavity surface emitting laser on Si-substrates. *Journal of Applied Physics* **109**, 093101 (2011). ⟨3⟩.

[40] Ryckeboer, E. *et al.* Silicon-on-insulator spectrometers with integrated GaInAsSb photodiodes for wide-band spectroscopy from 1510 to 2300 nm. *Optics Express* **21**, 6101–6108 (2013). ⟨3⟩.

[41] Wang, R. *et al.* 2 um wavelength range InP-based type-II quantum well photodiodes heterogeneously integrated on silicon photonic integrated circuits. *Optics Express* **23**, 26834–26841 (2015). ⟨122⟩.

[42] Muneeb, M. *et al.* III-V-on-silicon integrated micro - spectrometer for the 3 um wavelength range. *Optics Express* **24**, 9465–9472 (2016). ⟨3⟩.

[43] Yu, M. *et al.* Silicon-chip-based mid-infrared dual-comb spectroscopy. *Nature Communications* **9**, 1869 (2018). ⟨3⟩.

[44] Wang, R. *et al.* III-V/silicon photonic integrated circuits for spectroscopic sensing in the 2um wavelength range. In Lee, E.-H. & He, S. (eds.) *Smart Photonic and Optoelectronic Integrated Circuits XX*, 2 (SPIE, San Francisco, United States, 2018). ⟨3, 122⟩.

[45] Giovannetti, V., Lloyd, S. & Maccone, L. Quantum-enhanced measurements: Beating the standard quantum limit. *Science* **306**, 1330–1336 (2004). ⟨3, 5, 96⟩.

[46] Whittaker, R. *et al.* Absorption spectroscopy at the ultimate quantum limit from single-photon states. *New Journal of Physics* **19** (2017). ⟨3, 5⟩.

[47] Jones, J. A. *et al.* Magnetic field sensing beyond the standard quantum limit using 10-spin noon states. *Science* **324**, 1166–1168 (2009). ⟨3⟩.

[48] Lawrie, B. J., Lett, P. D., Marino, A. M. & Pooser, R. C. Quantum sensing with squeezed light. *ACS Photonics* **6**, 1307–1318 (2019). ⟨3⟩.

[49] Aasi, J., Abbott, B. P. & Al, E. Advanced LIGO. *Classical and Quantum Gravity* **32** (2015).

[50] Atkinson, G., Allen, E., Ferranti, G., McMillan, A. & Matthews, J. Quantum enhanced precision estimation of transmission with bright squeezed light. *Physical Review Applied* **16**, 044031–044031 (2021). ⟨3, 31, 36, 58, 64, 72, 80, 122⟩.

[51] Lvovsky, A. I. & Raymer, M. G. Continuous-variable optical quantum-state tomography. *Reviews of Modern Physics* **81**, 299–332 (2009). ⟨4, 30⟩.

[52] Bristow, A. D., Rotenberg, N. & Van Driel, H. M. Two-photon absorption and Kerr coefficients of silicon for 850-2200 nm. *Applied Physics Letters* **90**, 191104–191104 (2007). ⟨4⟩.

[53] Wang, T. *et al.* Multi-photon absorption and third-order nonlinearity in silicon at mid-infrared wavelengths. *Optics Express* **21**, 32192–32198 (2013). ⟨4⟩.

[54] Garcia, H. & Kalyanaraman, R. Phonon-assisted two-photon absorption in the presence of a dc-field: The nonlinear Franz–Keldysh effect in indirect gap semiconductors. *Journal of Physics B: Atomic, Molecular and Optical Physics* **39**, 2737–2746 (2006). ⟨4⟩.

[55] Rumi, M. & Perry, J. W. Two-photon absorption: An overview of measurements and principles. *Advances in Optics and Photonics* **2**, 451–518 (2010). ⟨4⟩.

[56] Walls, D. F. & Milburn, G. J. *Quantum Optics* (Springer, 2007), second edn. ⟨4, 10, 12, 15⟩.

[57] Sang, X., Tien, E. & Boyraz, O. Applications of two-photon absorption in silicon. *Journal of Optoelectronics and Advanced Materials* **11(1)** (2008). ⟨4⟩.

[58] Ispasoiu, R. G., Jin, Y., Lee, J., Papadimitrakopoulos, F. & Goodson, T. Two-photon absorption and photon-number squeezing with cdse nanocrystals. *Nano Letters* **2**, 127–130 (2002). ⟨4⟩.

[59] Husko, C. A. *et al.* Multi-photon absorption limits to heralded single photon sources. *Scientific Reports* **3** (2013). ⟨5⟩.

[60] Ramelow, S. *et al.* Silicon-nitride platform for narrowband entangled photon generation. *arXiv* (2015). 1508.04358. ⟨5⟩.

[61] Ji, X. *et al.* Ultra-low-loss on-chip resonators with sub-milliwatt parametric oscillation threshold. *Optica* **4**, 619–624 (2017). ⟨5⟩.

[62] Gardeniers, J. G. E., Tilmans, H. a. C. & Visser, C. C. G. LPCVD silicon-rich silicon nitride films for applications in micromechanics, studied with statistical experimental design*. *Journal of Vacuum Science & Technology A* **14**, 2879–2892 (1996). ⟨5⟩.

[63] Grillot, F., Vivien, L., Laval, S., Pascal, D. & Cassan, E. Size influence on the propagation loss induced by sidewall roughness in ultrasmall SOI waveguides. *IEEE Photonics Technology Letters* **16**, 1661–1663 (2004). ⟨5, 82⟩.

[64] Cheben, P., Halir, R., Schmid, J. H., Atwater, H. A. & Smith, D. R. Subwavelength integrated photonics. *Nature* **560**, 565–572 (2018). ⟨5⟩.

[65] Rosenfeld, L. M. *et al.* Mid-infrared quantum optics in silicon. *Optics Express* **28**, 37092–37092 (2020). ⟨5, 30, 31, 77, 81, 83⟩.

[66] Mouret, G. *et al.* THz media characterization by means of coherent homodyne detection, results and potential applications. *Applied Physics B* **89**, 395–399 (2007). ⟨5⟩.

[67] Mahler, D. H. *et al.* An on-chip homodyne detector for measuring quantum states. In *Optics InfoBase Conference Papers*, vol. Part F43-C, JTh3E.6–JTh3E.6 (OSA, Washington, D.C., 2017). ⟨5⟩.

[68] Tasker, J. F. *et al.* Silicon photonics interfaced with integrated electronics for 9 GHz measurement of squeezed light. *Nature Photonics* **15**, 11–15 (2021). ⟨5, 58, 59⟩.

[69] Carlisle, C. B. & Cooper, D. E. Tunable-diode-laser frequency-modulation spectroscopy using balanced homodyne detection. *Optics Letters* **14**, 1306–1306 (1989). ⟨5, 31, 119⟩.

[70] Chen, W., Mouret, G. & Boucher, D. Difference-frequency laser spectroscopy detection of acetylene trace constituent. *Applied Physics B: Lasers and Optics* **67**, 375–378 (1998). ⟨31⟩.

[71] Sonnenfroh, D. M. *et al.* Application of balanced detection to absorption measurements of trace gases with room-temperature, quasi-cw quantum-cascade lasers. *Applied Optics* **40**, 812–812 (2001). ⟨5, 31, 64, 119, 121⟩.

[72] Kenfack, A. & yczkowski, K. Negativity of the Wigner function as an indicator of non-classicality. *Journal of Optics B: Quantum and Semiclassical Optics* **6**, 396–404 (2004). ⟨6, 14, 60⟩.

[73] Neuman, K. C., Chadd, E. H., Liou, G. F., Bergman, K. & Block, S. M. Characterization of photodamage to Escherichia coli in optical traps. *Biophysical Journal* **77**, 2856–2863 (1999). ⟨6, 95⟩.

[74] Peterman, E. J., Gittes, F. & Schmidt, C. F. Laser-induced heating in optical traps. *Biophysical Journal* **84**, 1308–1316 (2003). ⟨6, 95⟩.

[75] Griffith, D. J. *Introduction to Electrodynamics* (Cambridge University Press, 2017). ⟨9, 11⟩.

[76] Davis, L. W. & Patsakos, G. TM and TE electromagnetic beams in free space. *Optics Letters* **6**, 22–23 (1981). ⟨10⟩.

[77] Gerry, C. & Knight, P. *Introductory Quantum Optics* (Cambridge University Press, Cambridge, 2004). ⟨11, 12, 13, 15⟩.

[78] Loudon, R. *The Quantum Theory of Light* (OUP Oxford, 2000). ⟨11, 12, 13, 15, 17, 18⟩.

[79] Protsenko, I. *et al.* Quantum theory of a thresholdless laser. *Physical Review A* **59**, 1667–1682 (1999). ⟨14⟩.

[80] Bachor, H.-A. H.-A., Ralph, T. C. & Wiley InterScience (Online service). *A Guide to Experiments in Quantum Optics*. A Guide to Experiments in Quantum Optics (Weinheim, Germany, 2004). ⟨14, 19, 32, 71, 104⟩.

[81] Leonhardt, U. Essential quantum optics: From quantum measurements to black holes. In *Essential Quantum Optics: From Quantum Measurements to Black Holes*, vol. 9780521869, 1–277 (Cambridge University Press, Cambridge, 2010). ⟨14, 33⟩.

[82] Walls, D. F. Squeezed states of light. *Nature* **306**, 141–146 (1983). ⟨16⟩.

[83] Hanamura, E., Kawabe, Y. & Yamanaka, A. *Quantum Nonlinear Optics* (Springer Science & Business Media, 2007). ⟨16⟩.

[84] Lvovsky, A. I. Squeezed Light. In *Photonics:*

Scientific Foundations, Technology and Applications, vol. 1, 121–163 (John Wiley & Sons, Inc., Hoboken, NJ, USA, 2015). ⟨17⟩.

[85] Zeilinger, A. General properties of lossless beam splitters in interferometry. *American Journal of Physics* **49**, 882–883 (1981). ⟨21⟩.

[86] Agrawal, G. P. Nonlinear Fiber Optics. *Nonlinear Science at the Dawn of the 21st Century* 195–211 (2007). ⟨22, 23, 24, 66, 67, 69, 83⟩.

[87] Jackson. *Classical Electrodynamics* (Wiley, 1998), 3rd edn. ⟨22, 67⟩.

[88] Payne, F. P. & Lacey, J. P. A theoretical analysis of scattering loss from planar optical waveguides. *Optical and Quantum Electronics* **26**, 977–986 (1994). ⟨24, 81, 82⟩.

[89] Reed, G. T. & Knights, A. P. *Silicon Photonics: An Introduction* (Wiley, 2004). ⟨24, 25⟩.

[90] Rukhlenko, I. D., Premaratne, M. & Agrawal, G. P. Effective mode area and its optimization in silicon-nanocrystal waveguides. *Optics Letters* **37**, 2295–2295 (2012). ⟨24⟩.

[91] Frey, B. J., Leviton, D. B. & Madison, T. J. Temperature-dependent refractive index of silicon and germanium. In *Optomechanical Technologies for Astronomy*, vol. 6273, 790–799 (SPIE, 2006). ⟨27⟩.

[92] Biele, J. *et al.* Shot-noise limited homodyne detection for MHz quantum light characterisation in the 2 um band. *Optics Express* **30**, 7716–7724 (2022). ⟨29, 49, 51, 54, 56, 57⟩.

[93] Yuen, H. P. & Chan, V. W. Noise in homodyne and heterodyne detection. *Optics Letters, Vol. 8, Issue 3, pp. 177-179* **8**, 218–220 (1983). ⟨29⟩.

[94] Dixon, P. K. & Wu, L. Broadband digital lock-in amplifier techniques. *Review of Scientific Instruments* **60**, 3329–3336 (1989). ⟨30⟩.

[95] Noll, D. C., Nishimura, D. G. & Macovski, A. Homodyne Detection in Magnetic Resonance Imaging. *IEEE Transactions on Medical Imaging* **10**, 154–163 (1991). ⟨30⟩.

[96] Fuwa, M., Takeda, S., Zwierz, M., Wiseman, H. M. & Furusawa, A. Experimental proof of nonlocal wavefunction collapse for a single particle using homodyne measurements. *Nature Communications* **6**, 1–6 (2015). ⟨30⟩.

[97] Gross, C. *et al.* Atomic homodyne detection of continuous-variable entangled twin-atom states. *Nature* **480**, 219–223 (2011). ⟨30⟩.

[98] Jouguet, P., Kunz-Jacques, S., Leverrier, A., Grangier, P. & Diamanti, E. Experimental demonstration of long-distance continuous-variable quantum key distribution. *Nature Photonics* **7**, 378–381 (2013). ⟨30⟩.

[99] Breitenbach, G., Schiller, S. & Mlynek, J. Measurement of the quantum states of squeezed light. *Nature* **387**, 471–475 (1997). ⟨30⟩.

[100] Ourjoumtsev, A., Jeong, H., Tualle-Brouri, R. & Grangier, P. Generation of optical 'Schrödinger cats' from photon number states. *Nature* **448**, 784–786 (2007). ⟨30⟩.

[101] Gabriel, C. *et al.* A generator for unique quantum random numbers based on vacuum states. *Nature Photonics* **4**, 711–715 (2010). ⟨30⟩.

[102] Millot, G. *et al.* Frequency-agile dual-comb spectroscopy. *Nature Photonics* **10**, 27–30 (2016). ⟨30⟩.

[103] Furusawa, A. *et al.* Unconditional quantum teleportation. *Science* **282**, 706–709 (1998). ⟨30⟩.

[104] Mansell, G. L. *et al.* Observation of Squeezed Light in the 2 μ m Region. *Physical Review Letters* **120** (2018). ⟨30, 31⟩.

[105] Yap, M. J. *et al.* Squeezed vacuum phase control at 2 Mm. *Optics Letters* **44**, 5386–5386 (2019). ⟨30, 31⟩.

[106] Temporao, G. *et al.* Feasibility study of free-space quantum key distribution in the mid-infrared. *Quantum Information and Computation* **8**, 0001–0011 (2008). ⟨30, 58⟩.

[107] Bartalini, S., Borri, S. & De Natale, P. Doppler-free polarization spectroscopy with a quantum cascade laser at 43 Mm. *Optics Express* **17**, 7440–7440 (2009). ⟨31⟩.

[108] Lendl, B., Moser, H. & Waclawek, J. P. Balanced-

detection interferometric cavity-assisted photothermal spectroscopy employing an all-fiber-coupled probe laser configuration. *Optics Express, Vol. 29, Issue 5, pp. 7794-7808* **29**, 7794–7808 (2021). ⟨31, 58⟩.

[109] Leleux, D. P. *et al.* Ammonia detection by use of near-infrared diode-laser-based overtone spectroscopy. *Applied Optics, Vol. 40, Issue 24, pp. 4387-4394* **40**, 4387–4394 (2001). ⟨31, 58, 119⟩.

[110] Cole, D. C., Papp, S. B. & Diddams, S. A. Downsampling of optical frequency combs. *Journal of the Optical Society of America B* **35**, 1666–1666 (2018). ⟨31, 58⟩.

[111] Gabbrielli, T. *et al.* Mid-infrared homodyne balanced detector for quantum light characterization. *Optics Express* **29**, 14536–14536 (2021). ⟨31⟩.

[112] Grangier, P., Slusher, R. E., Yurke, B. & LaPorta, A. Squeezed-light enhanced polarization interferometer. *Physical Review Letters* **59**, 2153–2156 (1987). ⟨31, 64⟩.

[113] Biagi, N., Bohmann, M., Agudelo, E., Bellini, M. & Zavatta, A. Experimental certification of nonclassicality via phase-space inequalities. *Physical Review Letters* **126**, 023605–023605 (2021). ⟨31⟩.

[114] Kumar, R. *et al.* Versatile wideband balanced detector for quantum optical homodyne tomography. *Optics Communications* **285**, 5259–5267 (2012). ⟨34, 35, 59⟩.

[115] Almeida, M., Pereira, D., Facão, M., Pinto, A. N. & Silva, N. A. Impact of imperfect homodyne detection on measurements of vacuum states shot noise. *Optical and Quantum Electronics* **52**, 503–503 (2020). ⟨34⟩.

[116] Graeme, J. *Photodiode Amplifiers Op-Amp Solutions* (McGraw-Hill, 1995). ⟨36, 38⟩.

[117] Sackinger, E. *Analysis and Design of Transimpedance* (Wiley, 2017). ⟨36, 42, 44⟩.

[118] Atkinson, G. *Quantum Metrology with Bright Squeezed Light*. Ph.D. thesis, Bristol University (2021). ⟨36, 37⟩.

[119] Helfrick, A. D. *Electrical Spectrum and Network Analyzers: A Practical Approach* (Academic Press, 1991), 1st edn. ⟨36⟩.

[120] Technologies, A. Spectrum and Signal Analyszer Measurements and Noise (2011). ⟨36, 37⟩.

[121] Yun, I. (ed.) *Photodiodes : From Fundamentals to Applications* (IntechOpen, 2012). ⟨39, 40⟩.

[122] Zhou, L. *et al.* Dark current characteristics of GaAs-based 2.6 μ m InGaAs photodetectors on different types of InAlAs buffer layers. *Journal of Physics D: Applied Physics* **47**, 085107 (2014). ⟨39, 41⟩.

[123] Nunna, K. C. *et al.* Short-Wave Infrared GaInAsSb Photodiodes Grown on GaAs Substrate by Interfacial Misfit Array Technique. *IEEE Photonics Technology Letters* **24**, 218–220 (2012). ⟨41⟩.

[124] Joshi, A. & Datta, S. High-speed, large-area, p-i-n InGaAs photodiode linear array at 2-micron wavelength. In *Infrared Technology and Applications XXXVIII*, vol. 8353, 1158–1166 (SPIE, 2012). ⟨41⟩.

[125] Goushcha, A. O. & Tabbert, B. On response time of semiconductor photodiodes. *Optical Engineering* **56**, 1–1 (2017). ⟨42, 44⟩.

[126] Miyazaki, D. Fresnel Equations. In Ikeuchi, K. (ed.) *Computer Vision: A Reference Guide*, 305–307 (Springer US, Boston, MA, 2014). ⟨42⟩.

[127] Graeme, J. Photodiode amplifiers 108–111 (1996). ⟨42⟩.

[128] Roberge, J. *Operational Amplifiers: Theory and Practice*. ⟨42⟩.

[129] Masalov, A. V., Kuzhamuratov, A. & Lvovsky, A. I. Noise spectra in balanced optical detectors based on transimpedance amplifiers. *Review of Scientific Instruments* **88** (2017). ⟨45, 47⟩.

[130] Hui, R. Chapter 4 - Photodetectors. In Hui, R. (ed.) *Introduction to Fiber-Optic Communications*, 125–154 (Academic Press, 2020). ⟨46⟩.

[131] Boggs, C., Doak, A. & Walls, F. Measurement of voltage noise in chemical batteries. In *Proceedings of the 1995 IEEE International Frequency Con-*

trol Symposium (49th Annual Symposium), 367–373 (1995). ⟨47⟩.

[132] Chi, Y.-M. *et al.* A balanced homodyne detector for high-rate Gaussian-modulated coherent-state quantum key distribution. *New Journal of Physics* **13**, 013003–013003 (2011). ⟨48, 56⟩.

[133] Jin, X. *et al.* Balanced homodyne detection with high common mode rejection ratio based on parameter compensation of two arbitrary photodiodes. *Optics Express* **23**, 23859–23859 (2015). ⟨48, 59⟩.

[134] Thorlabs. Balanced Detector Manual (PDB48xC-AC) (2020). ⟨48⟩.

[135] Devices, A. LTSpice (2020). ⟨49⟩.

[136] Hoff, U. B., Nielsen, B. M. & Andersen, U. L. Integrated source of broadband quadrature squeezed light. *Optics Express* **23**, 12013–12013 (2015). ⟨58, 65⟩.

[137] Yu, J., Petros, M., Singh, U., Kavaya, M. & Koch, G. Development of 2-micron lasers and lidars for 3D wind and carbon dioxide measurement. *Optical Instrumentation for Energy and Environmental Applications, E2 2014* EF4A.1–EF4A.1 (2014). ⟨58⟩.

[138] Refaat, T. F. *et al.* Airborne, direct-detection, 2-um triple-pulse IPDA lidar for simultaneous and independent atmospheric water vapor and carbon dioxide active remote sensing. In Sugimoto, N. & Singh, U. N. (eds.) *Lidar Remote Sensing for Environmental Monitoring XVI*, vol. 10779, 1–1 (SPIE, 2018). ⟨58⟩.

[139] Takeda, S. & Furusawa, A. Toward large-scale fault-tolerant universal photonic quantum computing. *APL Photonics* **4** (2019). ⟨58⟩.

[140] Larsen, M. V., Guo, X., Breum, C. R., Neergaard-Nielsen, J. S. & Andersen, U. L. Deterministic generation of a two-dimensional cluster state. *Science* (2019). ⟨58⟩.

[141] Asavanant, W. *et al.* Generation of time-domain-multiplexed two-dimensional cluster state. Tech. Rep. 6463 (2019). ⟨58⟩.

[142] Xu, S. *et al.* Integrating GeSn photodiode on a 200 mm Ge-on-insulator photonics platform with Ge CMOS devices for advanced OEIC operating at 2 Mm band. *Optics Express* **27**, 26924–26939 (2019). ⟨59⟩.

[143] Gumenyuk, R., Vartiainen, I., Tuovinen, H. & Okhotnikov, O. G. Dissipative dispersion-managed soliton 2 Mm thulium/holmium fiber laser. *Optics Letters* **36**, 609–611 (2011). ⟨60⟩.

[144] Euan Allen. *Suppression of Noise in Classical and Quantum Optics*. Ph.D. thesis, University of Bristol (2019). ⟨63, 64⟩.

[145] Caves, C. M. Quantum limits on noise in linear amplifiers. *Physical Review D* **26**, 1817–1839 (1982). ⟨64⟩.

[146] Henry, C. H. & Kazarinov, R. F. Quantum noise in photonics. *Reviews of Modern Physics* **68**, 801–853 (1996). ⟨64⟩.

[147] Hodgkinson, J. & Tatam, R. P. Optical gas sensing: A review. *Measurement Science and Technology* **24**, 012004 (2012). ⟨64⟩.

[148] Hobbs, P. C. D. Ultrasensitive laser measurements without tears. *Applied Optics* **36**, 903–920 (1997). ⟨64⟩.

[149] Robertson, N. A., Hoggan, S., Mangan, J. B. & Hough, J. Intensity stabilisation of an argon laser using an electro-optic modulator —Performance and limitations. *Applied Physics B* **39**, 149–153 (1986). ⟨64⟩.

[150] Alnis, J., Matveev, A., Kolachevsky, N., Udem, T. & Hänsch, T. W. Subhertz linewidth diode lasers by stabilization to vibrationally and thermally compensated ultralow-expansion glass Fabry-P\'erot cavities. *Physical Review A* **77**, 053809 (2008). ⟨64⟩.

[151] Danion, G., Bondu, F., Loas, G. & Alouini, M. GHz bandwidth noise eater hybrid optical amplifier: Design guidelines. *Optics Letters* **39**, 4239–4242 (2014). ⟨64⟩.

[152] Doerr, C. R., Shirasaki, M. & Khatri, F. I. Simulation of pulsed squeezing in optical fiber with chromatic dispersion. *Journal of the Optical Soci-*

ety of America B **11**, 143–143 (1994). ⟨64, 72, 73, 77⟩.

[153] Fiorentino, M., Sharping, J., Kumar, P. & Porzio, A. Amplitude squeezing in a Mach-Zehnder fiber interferometer: Numerical analysis of experiments with microstructure fiber. *Optics Express* **10**, 128–128 (2002). ⟨64, 73, 76⟩.

[154] Sawai, S., Kawauchi, H., Hirosawa, K. & Kannari, F. Photon-number squeezing with a noisy femtosecond fiber laser amplifier source using a collinear balanced detection technique. *Optics Express* **21**, 25099–25106 (2013). ⟨64⟩.

[155] Spälter, S. *et al.* Photon number squeezing of spectrally filtered sub-picosecond optical solitons. *Europhysics Letters* **38**, 335 (1997). ⟨64, 86⟩.

[156] Kanter, G. S. *et al.* Squeezing in a $LiNbO_3$ integrated optical waveguide circuit. *Optics Express* **10**, 177–182 (2002). ⟨64⟩.

[157] Dutt, A. *et al.* On-chip optical squeezing. *Physical Review Applied* **3**, 044005–044005 (2015). ⟨65⟩.

[158] Dutt, A. *et al.* Tunable squeezing using coupled ring resonators on a silicon nitride chip. *Optics Letters* **41**, 223–226 (2016). ⟨65⟩.

[159] Cernansky, R. & Politi, A. Nanophotonic source of quadrature squeezing via self-phase modulation. *APL Photonics* **5**, 101303 (2020). ⟨65, 94⟩.

[160] Vaidya, V. D. *et al.* Broadband quadrature-squeezed vacuum and nonclassical photon number correlations from a nanophotonic device. *Science Advances* **6**, eaba9186 (2020). ⟨65, 120⟩.

[161] Zhang, Y. *et al.* Squeezed light from a nanophotonic molecule. *Nature Communications* **12**, 2233 (2021). ⟨65, 120⟩.

[162] Payne, D. *Integrating the Generation and Detection of Continuous-Variable Quantum States Using Silicon and Its Compounds*. Ph.D. thesis, Univeristy of Bristol (2022). ⟨65⟩.

[163] Pavesi, L. & Vivien, L. *Handbook of Silicon Photonics* (*Optics and Optoelectronics*) (CRC Press), 1st edn. ⟨66⟩.

[164] Weinberger, P. John Kerr and his effects found in 1877 and 1878. *Philosophical Magazine Letters* **88**, 897–907 (2008). ⟨66⟩.

[165] Shirasaki, M. & Haus, H. A. Squeezing of pulses in a nonlinear interferometer. *Journal of the Optical Society of America B* **7**, 30–30 (1990). ⟨70, 72⟩.

[166] Culshaw, B. The optical fibre Sagnac interferometer: An overview of its principles and applications. *Measurement Science and Technology* **17**, R1–R16 (2006). ⟨70⟩.

[167] Schmitt, S. *et al.* Photon-number squeezed solitons from an asymmetric fiber-optic sagnac interferometer. *Physical Review Letters* **81**, 2446–2449 (1998). ⟨72, 77⟩.

[168] Tana´stana´s, R. Theory of Nonclassical States of Light. Tech. Rep. (2003). ⟨72, 73⟩.

[169] Johansson, J. R., Nation, P. D. & Nori, F. QuTiP 2: A Python framework for the dynamics of open quantum systems. *Computer Physics Communications* **184**, 1234–1240 (2013). ⟨73, 115⟩.

[170] Thomas, N. L., Dhakal, A., Raza, A., Peyskens, F. & Baets, R. Impact of fundamental thermodynamic fluctuations on light propagating in photonic waveguides made of amorphous materials. *Optica* **5**, 328–336 (2018). ⟨77, 93⟩.

[171] Fiorentino, M., Sharping, J. E., Kumar, P., Porzio, A. & Windeler, R. S. Soliton squeezing in microstructure fiber. Tech. Rep. 8 (2002). ⟨80⟩.

[172] Fiorentino, M., Sharping, J. E., Kumar, P., Levandovsky, D. & Vasilyev, M. Soliton squeezing in a Mach-Zehnder fiber interferometer. *Physical Review A - Atomic, Molecular, and Optical Physics* **64**, 4–4 (2001). ⟨80⟩.

[173] Friberg, S. R., Machida, S., Werner, M. J., Levanon, A. & Mukai, T. Observation of optical soliton photon-number squeezing. Tech. Rep. 18 (1996). ⟨80, 92⟩.

[174] Hagan, D. E. & Knights, A. P. Mechanisms for optical loss in SOI waveguides for mid-infrared wavelengths around 2 *M*m. *Journal of Optics* (*United Kingdom*) **19** (2017). ⟨81⟩.

[175] Silfvast, W. T. *Laser Fundamentals* (Cambridge University Press, 2008), second edn. ⟨87⟩.

[176] Alem, M., Soto, M. A. & Thévenaz, L. Analytical model and experimental verification of the critical power for modulation instability in optical fibers. *Optics Express* **23**, 29514–29532 (2015). ⟨89, 91⟩.

[177] Anderson, D. & Lisak, M. Modulational instability of coherent optical-fiber transmission signals. *Optics Letters* **9**, 468–470 (1984). ⟨89⟩.

[178] Mazhar, S. F. B. & Alfano, R. R. Modulation instability induced by cross-phase modulation of transient stimulated Raman scattering and self-phase modulation in calcite. *Optics Letters* **45**, 3167–3170 (2020). ⟨91⟩.

[179] Drummond, P. D., Kennedy, T. A. B., Dudley, J. M., Leonhardt, R. & Harvey, J. D. Cross-phase modulational instability in high-birefringence fibers. *Optics Communications* **78**, 137–142 (1990). ⟨91⟩.

[180] Tombez, L., Zhang, E. J., Orcutt, J. S., Kamlapurkar, S. & Green, W. M. J. Methane absorption spectroscopy on a silicon photonic chip. *Optica* **4**, 1322–1322 (2017). ⟨91⟩.

[181] Takiguchi, K., Itoh, M. & Shibata, T. Optical-signal-processing device based on waveguide-type variable delay lines and optical gates. *Journal of Lightwave Technology* **24**, 2593–2601 (2006). ⟨92⟩.

[182] Willner, A. E., Zhang, B., Zhang, L., Yan, L. & Fazal, I. Optical Signal Processing Using Tunable Delay Elements Based on Slow Light. *IEEE Journal of Selected Topics in Quantum Electronics* **14**, 691–705 (2008). ⟨92⟩.

[183] Fercher, A. F. & Hitzenberger, C. K. Chapter 4 - Optical coherence tomography. In Wolf, E. (ed.) *Progress in Optics*, vol. 44, 215–302 (Elsevier, 2002). ⟨92⟩.

[184] Song, Q. Q., Hu, Z. F. & Chen, K. X. Scalable and reconfigurable true time delay line based on an ultra-low-loss silica waveguide. *Applied Optics* **57**, 4434–4439 (2018). ⟨92⟩.

[185] Saunders, R., Patel, B., Garthe, D. & Lee, W. Impact of modulation instability on high bit rate optically-amplified transmission systems. In *IEE Colloquium on High Speed and Long Distance Optical Transmission*, 16/1–16/5 (1996). ⟨92⟩.

[186] Han, J. *et al.* Optimizing noise characteristics of mode-locked Yb-doped fiber laser using gain-induced RIN-transfer dynamics. *High Power Laser Science and Engineering* **9** (2021/ed). ⟨93⟩.

[187] Allen, E. J. *et al.* Passive, broadband, and low-frequency suppression of laser amplitude noise to the shot-noise limit using a hollow-core fiber. *Physical Review Applied* **12**, 044073 (2019). ⟨93⟩.

[188] Haus, H. A. From classical to quantum noise. *JOSA B* **12**, 2019–2036 (1995). ⟨93⟩.

[189] Elshaari, A. W., Zadeh, I. E., Jöns, K. D. & Zwiller, V. Thermo-Optic Characterization of Silicon Nitride Resonators for Cryogenic Photonic Circuits. *IEEE Photonics Journal* **8**, 1–9 (2016). ⟨94⟩.

[190] Biele, J., Wollmann, S., Silverstone, J. W., Matthews, J. C. F. & Allen, E. J. Maximizing precision in saturation-limited absorption measurements. *Physical Review A* **104**, 053717 (2021). ⟨95, 98, 100, 105, 109, 111, 117⟩.

[191] Carpentier, R., Leblanc, R. M. & Mimeault, M. Photoinhibition and chlorophyll photobleaching in immobilized thylakoid membranes. *Enzyme and Microbial Technology* **9**, 489–493 (1987). ⟨95, 118⟩.

[192] Bopp, M. A., Jia, Y., Li, L., Cogdell, R. J. & Hochstrasser, R. M. Fluorescence and photobleaching dynamics of single light-harvesting complexes. *Proceedings of the National Academy of Sciences of the United States of America* **94**, 10630–10635 (1997).

[193] Henderson, J. N., Ai, H. W., Campbell, R. E. & Remington, S. J. Structural basis for reversible photobleaching of a green fluorescent protein homologue. *Proceedings of the National Academy of Sciences of the United States of America* **104**, 6672–6677 (2007). ⟨95, 118⟩.

[194] Toffolo, M. B. & Berna, F. Infrared Absorption Spectroscopy (IR, FTIR, DRIFT, ATR). In *The Encyclopedia of Archaeological Sciences*, 1–4 (John

Wiley & Sons, Inc., 2018). ⟨95⟩.

[195] Corrêa, D. S. *et al.* Reverse saturable absorption in chlorophyll A solutions. *Applied Physics B: Lasers and Optics* **74**, 559–561 (2002). ⟨106⟩.

[196] Taylor, M. A. & Bowen, W. P. Quantum metrology and its application in biology. *Physics Reports* **615**, 1–59 (2016). ⟨95, 96⟩.

[197] Escher, B. M., De Matos Filho, R. L. & Davidovich, L. General framework for estimating the ultimate precision limit in noisy quantum-enhanced metrology. *Nature Physics* **7**, 406–411 (2011). ⟨96, 102⟩.

[198] Monras, A. & Paris, M. G. Optimal quantum estimation of loss in bosonic channels. *Physical Review Letters* **98**, 160401–160401 (2007). ⟨96⟩.

[199] Losero, E., Ruo-Berchera, I., Meda, A., Avella, A. & Genovese, M. Unbiased estimation of an optical loss at the ultimate quantum limit with twin-beams. *Scientific Reports* **8**, 1–11 (2018).

[200] Allen, E. J. *et al.* Approaching the quantum limit of precision in absorbance estimation using classical resources. *Physical Review Research* **2**, 033243–033243 (2020). ⟨96, 102, 104, 107, 108⟩.

[201] Mitchell, M. W. Number-unconstrained quantum sensing. *Quantum Science and Technology* **2**, 44005–44005 (2017). ⟨96⟩.

[202] Chong, S., Min, W. & Xie, X. S. Ground-state depletion microscopy: Detection sensitivity of single-molecule optical absorption at room temperature. *Journal of Physical Chemistry Letters* **1**, 3316–3322 (2010). ⟨96, 108, 118⟩.

[203] Wang, P. *et al.* Far-field imaging of non-fluorescent species with subdiffraction resolution. *Nature Photonics* **7**, 449–453 (2013). ⟨96⟩.

[204] Kobyakov, A., Hagan, D. J. & Van Stryland, E. W. Analytical approach to dynamics of reverse saturable absorbers. *Journal of the Optical Society of America B* **17**, 1884–1884 (2000). ⟨97⟩.

[205] Abitan, H., Bohr, H. & Buchhave, P. Correction to the Beer-Lambert-Bouguer law for optical absorption. *Applied Optics* **47**, 5354–5357 (2008). ⟨97⟩.

[206] Islam, N., Mondal, T., Chakraborty, S. & Biswas, S. Re-examining Einstein's B coefficient and rate equations with the Rabi model. *Journal of Statistical Mechanics: Theory and Experiment* **2019**, 113104–113104 (2019). ⟨98, 99⟩.

[207] Ball, D. W. *Field Guide to Spectroscopy* (SPIE, 2006). ⟨98⟩.

[208] Corless, R. M. & Jeffrey, D. J. The Wright ω Function. 76–89 (Springer, Berlin, Heidelberg, 2002). ⟨100, 103⟩.

[209] Birchall, P. M. *et al.* Quantum optical metrology of correlated phase and loss. *Physical Review Letters* **124**, 140501–140501 (2020). ⟨102⟩.

[210] van der Vaart, A. W. *Asymptotic Statistics*. Asymptotic Statistics (Cambridge University Press, 1998). ⟨102⟩.

[211] Braunstein, S. L. & Caves, C. M. Statistical distance and the geometry of quantum states. *Physical Review Letters* **72**, 3439–3443 (1994). ⟨102⟩.

[212] Ziegel, E. R. & Lehmann, E. L. *Theory of Point Estimation*. Theory of Point Estimation (Springer-Verlag, New York, 1998). ⟨103⟩.

[213] Sargent, M., Scully, M. O. & Lamb, W. E. *Laser Physics*, vol. 1 of *Laser Physics* (Addison-Wesley Publishing Company, 2018), first edn. ⟨104⟩.

[214] Truong, G. W., Anstie, J. D., May, E. F., Stace, T. M. & Luiten, A. N. Accurate lineshape spectroscopy and the Boltzmann constant. *Nature Communications* **6**, 1–6 (2015). ⟨106, 118, 120⟩.

[215] Bain, J. R. *et al.* Recovery of absolute gas absorption line shapes using tunable diode laser spectroscopy with wavelength modulation-part 2: Experimental investigation. *Journal of Lightwave Technology* **29**, 987–996 (2011). ⟨106, 118⟩.

[216] Lichtenthaler, H. K. & Buschmann, C. Chlorophylls and Carotenoids: Measurement and Characterization by UV-VIS Spectroscopy. *Current Protocols in Food Analytical Chemistry* **1**, F4.3.1–F4.3.8 (2001). ⟨106⟩.

[217] Aminot, A. & Rey, F. ICES Techniques in Marine Environmental Sciences Chlorophyll a: Determi-

nation by spectroscopic methods International Council for the Exploration of the Sea Conseil International pour l'Exploration de la Mer. *ICES Techniques in Marine Environmental Sciences* (200). ⟨106⟩.

[218] Schalles, J. F. Optical remote sensing techniques to estimate phytoplankton chlorophyll a concentrations in coastal waters with varying suspended matter and cdom concentrations. In *Remote Sensing and Digital Image Processing*, vol. 9, 27–79 (Springer, Dordrecht, 2006). ⟨106⟩.

[219] Corrêa, D. S., De Boni, L., Pavinatto, F. J., Dos Santos, D. S. & Mendonça, C. R. Excited state absorption cross-section spectrum of Chlorophyll A. In *Conference on Quantum Electronics and Laser Science (QELS) - Technical Digest Series*, 1–2 (IEEE, 2007). ⟨106⟩.

[220] Birchall, P. M., O'Brien, J. L., Matthews, J. C. & Cable, H. Quantum-classical boundary for precision optical phase estimation. *Physical Review A* **96**, 062109–062109 (2017). ⟨107⟩.

[221] Bollinger, J. J. ., Itano, W. M., Wineland, D. J. & Heinzen, D. J. Optimal frequency measurements with maximally correlated states. *Physical Review A* **54**, R4649–R4652 (1996). ⟨107⟩.

[222] Holland, M. J. & Burnett, K. Interferometric detection of optical phase shifts at the Heisenberg limit. *Physical Review Letters* **71**, 1355–1358 (1993). ⟨107⟩.

[223] Wolf, F. *et al.* Motional Fock states for quantum-enhanced amplitude and phase measurements with trapped ions. *Nature Communications* **10**, 1–8 (2019). ⟨107⟩.

[224] Harrison, W. W., Yurachek, J. P. & Benson, C. A. The determination of trace elements in human hair by atomic absorption spectroscopy. *Clinica Chimica Acta* **23**, 83–91 (1969). ⟨108⟩.

[225] Christian, G. D. Medicine, trace elements, and atomic absorption spectroscopy. *Analytical Chemistry* **41**, 24–40 (1969). ⟨108⟩.

[226] Meyer-Scott, E., Silberhorn, C. & Migdall, A. Single-photon sources: Approaching the ideal through multiplexing. *Review of Scientific Instruments* **91**, 041101–041101 (2020). ⟨110⟩.

[227] Berezin, M. Y. & Achilefu, S. Fluorescence lifetime measurements and biological imaging. *Chemical Reviews* **110**, 2641–2684 (2010). ⟨110⟩.

[228] Eisaman, M. D., Fan, J., Migdall, A. & Polyakov, S. V. Invited Review Article: Single-photon sources and detectors. *Review of Scientific Instruments* **82**, 071101–071101 (2011). ⟨110⟩.

[229] Teich, M. C. & Saleh, B. E. Squeezed state of light. *Quantum Optics: Journal of the European Optical Society Part B* **1**, 153–191 (1989). ⟨110⟩.

[230] Vahlbruch, H., Mehmet, M., Danzmann, K. & Schnabel, R. Detection of 15 db squeezed states of light and their application for the absolute calibration of photoelectric quantum efficiency. *Physical Review Letters* **117**, 110801–110801 (2016). ⟨110⟩.

[231] Garraway, B. M. The Dicke model in quantum optics: Dicke model revisited. *Philosophical Transactions of the Royal Society A: Mathematical, Physical and Engineering Sciences* **369**, 1137–1155 (2011). ⟨111, 112⟩.

[232] Manzano, D. A short introduction to the Lindblad master equation. *AIP Advances* **10**, 025106–025106 (2020). ⟨111, 115⟩.

[233] Kirton, P., Roses, M. M., Keeling, J. & Dalla Torre, E. G. Introduction to the dicke model: From equilibrium to nonequilibrium, and vice versa. Tech. Rep. 1-2 (2019). ⟨112⟩.

[234] Walls, D. & Milburn, G. J. Interaction of radiation with atoms. In Walls, D. & Milburn, G. J. (eds.) *Quantum Optics*, 197–211 (Springer, Berlin, Heidelberg, 2008). ⟨112⟩.

[235] Walls, D. & Milburn, G. J. Quantisation of the electromagnetic field. In Walls, D. & Milburn, G. J. (eds.) *Quantum Optics*, 7–27 (Springer, Berlin, Heidelberg, 2008). ⟨112, 113⟩.

[236] Rempe, G. Atoms in an optical cavity: Quantum electrodynamics in confined space. *Contemporary Physics* **34**, 119–129 (1993). ⟨113⟩.

[237] Hilborn, R. C. Einstein coefficients, cross sec-

tions, f values, dipole moments, and all that. *American Journal of Physics* **50**, 982–986 (1982). ⟨113⟩.

[238] Anastopoulos, C. & Hu, B. L. Two-level atom-field interaction: Exact master equations for non-Markovian dynamics, decoherence, and relaxation. *Physical Review A - Atomic, Molecular, and Optical Physics* **62**, 13–13 (2000). ⟨113⟩.

[239] Leuchs, G. & Sondermann, M. Light-matter interaction in free space. *Journal of Modern Optics* **60**, 36–42 (2013). ⟨113⟩.

[240] Breuer, H.-P. & Petruccione, F. *The Theory of Open Quantum Systems* (Oxford University Press, Oxford, 2007). ⟨114⟩.

[241] Johansson, J. R., Nation, P. D. & Nori, F. QuTiP: An open-source Python framework for the dynamics of open quantum systems. *Computer Physics Communications* **183**, 1760–1772 (2012). ⟨115⟩.

[242] van Enk, S. J. & Kimble, H. J. Single atom in free space as a quantum aperture. Tech. Rep. 5 (2000). ⟨116⟩.

[243] Liu, R. *et al.* Strong Light-Matter Interactions in Single Open Plasmonic Nanocavities at the Quantum Optics Limit. *Physical Review Letters* **118**, 237401–237401 (2017). ⟨116⟩.

[244] Kumar, S. Theory of coherent, degenerate two-photon absorption and emission. Tech. Rep. 3 (1985). ⟨117⟩.

[245] Ingerman, E. A., London, R. A., Heintzmann, R. & Gustafsson, M. G. Signal, noise and resolution in linear and nonlinear structured-illumination microscopy. *Journal of Microscopy* **273**, 3–25 (2019). ⟨118⟩.

[246] Little, B. & Murphy, T. Design rules for maximally flat wavelength-insensitive optical power dividers using Mach-Zehnder structures. *IEEE Photonics Technology Letters* **9**, 1607–1609 (1997). ⟨119⟩.

[247] Marino, A. M., C. R. Stroud, J., Wong, V., Bennink, R. S. & Boyd, R. W. Bichromatic local oscillator for detection of two-mode squeezed states of light. *JOSA B* **24**, 335–339 (2007). ⟨120⟩.

[248] Barwicz, T., Green, W. M., Martin, Y. C., Orcutt, J. S. & Tombez, L. Gas sensor with integrated optics and reference cell (2017). ⟨121⟩.

[249] Leijtens, X. J., Kuhlow, B. & Smit, M. K. Arrayed waveguide gratings. In *Springer Series in Optical Sciences*, vol. 123, 125–187 (Springer Berlin Heidelberg, 2006). ⟨121⟩.

[250] Picqué, N. & Hänsch, T. W. Frequency comb spectroscopy. *Nature Photonics* **13**, 146–157 (2019). ⟨121⟩.

[251] Gaeta, A. L., Lipson, M. & Kippenberg, T. J. Photonic-chip-based frequency combs. *Nature Photonics* **13**, 158–169 (2019). ⟨121⟩.

[252] Seiyama, T., Kato, A., Fujiishi, K. & Nagatani, M. A New Detector for Gaseous Components Using Semiconductive Thin Films. *Analytical Chemistry* **34**, 1502–1503 (1962). ⟨121⟩.

[253] Aldhafeeri, T., Tran, M. K., Vrolyk, R., Pope, M. & Fowler, M. A review of methane gas detection sensors: Recent developments and future perspectives. *Inventions* **5**, 1–18 (2020). ⟨121⟩.

[254] Gervais, A., Jean, P., Shi, W. & LaRochelle, S. Design of slow-light subwavelength grating waveguides for enhanced on-chip methane sensing by absorption spectroscopy. *IEEE Journal of Selected Topics in Quantum Electronics* **25** (2019). ⟨122⟩.

[255] Stewart, G. Absorption Spectroscopy of Gases. *Laser and Fiber Optic Gas Absorption Spectroscopy* 1–20 (2021). ⟨122⟩.

[256] Sayers, B., Rosenfeld, L. & Silverstone, J. Electro-optic Kerr Modulation in Wide Silicon Waveguides in the Mid-IR. In *2021 Conference on Lasers and Electro-Optics Europe European Quantum Electronics Conference (CLEO/Europe-EQEC)*, 1–1 (2021). ⟨122⟩.

[257] Ryckeboer, E., Bockstaele, R., Vanslembrouck, M. & Baets, R. Glucose sensing by waveguide-based absorption spectroscopy on a silicon chip. *Biomedical Optics Express* **5**, 1636–1636 (2014). ⟨122⟩.